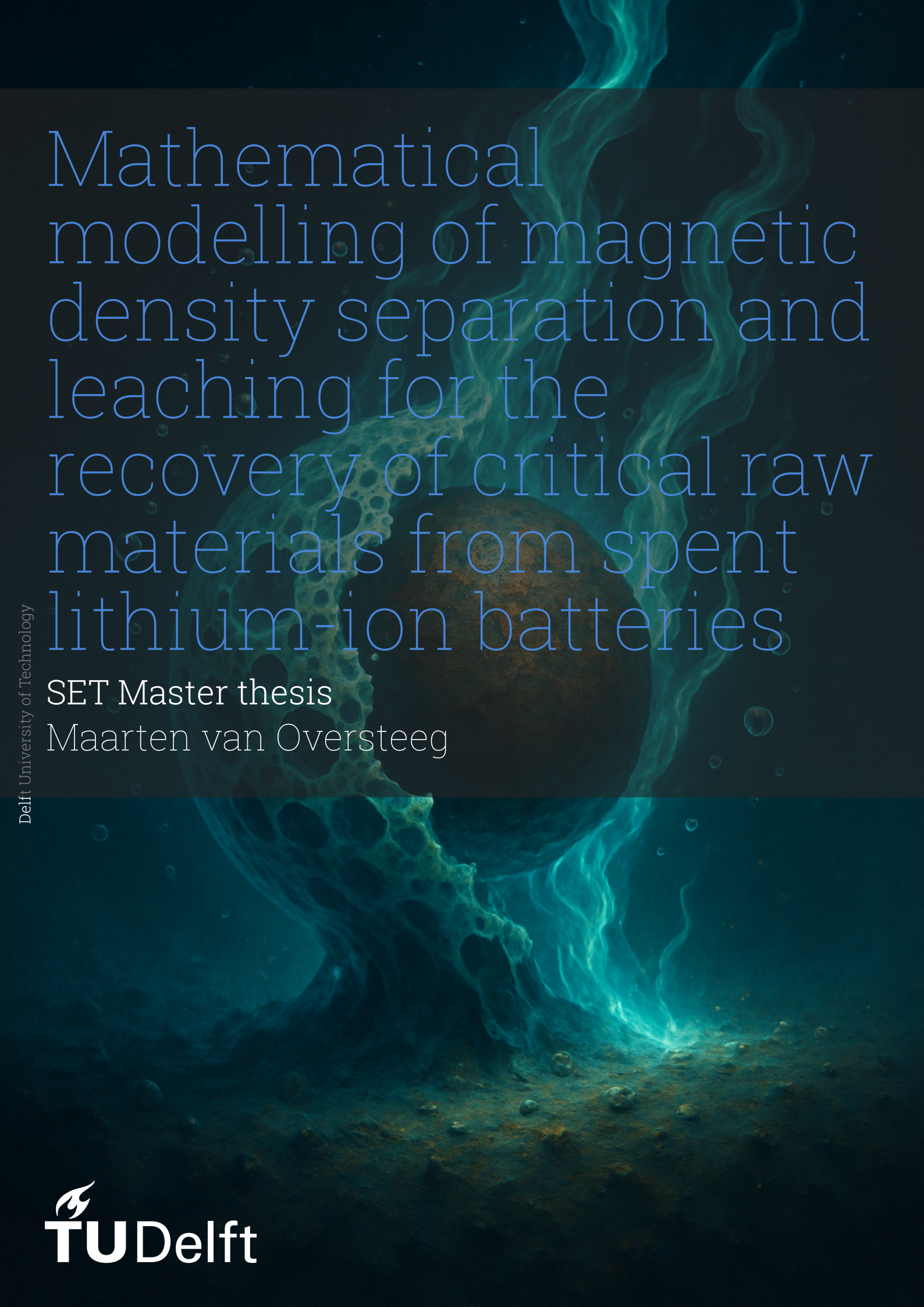

Mathematical modelling of magnetic density separation and leaching for the recovery of critical raw materials from spent lithium-ion batteries

SET Master thesis

Maarten van Oversteeg

Delft University of Technology

TU Delft

Mathematical modelling of magnetic density separation and leaching for the recovery of critical raw materials from spent lithium-ion batteries

by

Maarten van Oversteeg

to obtain the degree of Master of Science
at the Delft University of Technology,
to be defended publicly on Monday May 26, 2025 at 13:00 PM.

Student number:	4725808
Project Duration:	May 2024 - May 2025
Faculty:	Electrical Engineering Mathematics and Computer Sciences, TU Delft
Thesis Committee:	dr. L. Botto, TU Delft, Supervisor
	dr. M. Ramdin, TU Delft, Committee member
	dr. S. Abrahami, TU Delft, Committee member

TU Delft

Preface

This thesis was written by Maarten van Oversteeg as part of the Master's program in Sustainable Energy Technology at the Faculty of Electrical Engineering, Mathematics & Computer Science at Delft University of Technology.

My academic journey at TU Delft started in 2017 with the Bachelor's program in Applied Physics. Over the years, I developed a growing interest in the energy transition and the complex challenges it brings. Seeking a more tangible and applied direction, I decided to pursue the Master's in Sustainable Energy Technology, where I could combine my technical background with practical energy applications. Within this program, I focused on the largest renewable energy technologies: solar and wind energy. These technologies offer great potential but also pose many challenges due to their intermittent nature. This creates the need for sufficient energy storage technologies, which became the focus of this master thesis.

One of the key issues in energy storage systems like lithium-ion batteries is the increasing demand for critical raw materials such as lithium, cobalt, and graphite. In particular, Europe's heavy dependence on graphite imports from China poses a strategic vulnerability. This thesis addresses the recovery of such critical materials through computational modelling of magnetic density separation and hydrometallurgical leaching processes.

First, I would like to express my gratitude to my supervisor Lorenzo Botto for his invaluable guidance throughout this project. Your support and feedback taught me to conduct research independently and to critically review my own work, which was crucial to achieving the results of this thesis. Additionally, I want to thank Heng, Shoshan, Joep and Niels for their helpful insights and assistance during challenging moments. Finally, I would like to thank my parents, who supported me unconditionally throughout my studies. Your encouragement has always motivated me to get the best out of myself.

This master thesis represents a piece of work I am truly proud of. I hope it contributes to ongoing research within the Process and Energy department and to Europe's resilience in securing the critical raw materials essential for the production of sustainable energy storage systems.

Maarten van Oversteeg
Delft, May 2025

Abstract

With the increasing demand for lithium-ion batteries, the supply of critical raw materials such as graphite, lithium and cobalt has become increasingly important. In response to environmental impact and geopolitical reliance on Chinese exports, this study explores the recovery of these materials from spent lithium-ion batteries using computational modelling. Two methods are investigated: Magnetic Density Separation (MDS) and hydrometallurgical leaching using the Shrinking Core model (SCM).

The first part focuses on MDS, in which a two-dimensional particle tracking model was developed to simulate the separation of graphite particles suspended in a paramagnetic $\mathrm{MnCl_2}$ solution subjected to a non-uniform magnetic field. The model incorporated experimentally determined magnetic susceptibility values, a magnetic field profile generated from COMSOL and a particle size distribution. The simulation reproduced key phenomena which were experimentally observed such as levitation height around 5-6 mm, settling dynamics and lateral particle accumulation.

In the second part a dimensionless SCM was developed to describe the leaching behaviour of $\mathrm{LiCoO_2}$ particles in sulfuric acid. The model includes mass transfer, diffusion and surface reaction mechanisms to describe the dissolution of the $\mathrm{LiCoO_2}$ particles. While the SCM captured general leaching trends, it overestimated leaching efficiencies due to assumptions of uniform lithium dissolution and neglecting increasing diffusion resistance during the leaching process and it the effect of $\mathrm{H_2O_2}$ was not taken into account. Therefore a more advanced SCM with varying crust was developed, which included the formation of a $\mathrm{Co_3O_4}$ crust on the $\mathrm{LiCoO_2}$ core. For this model, the alignment with experimental leaching data was improved across varying conditions of acid concentrations, $\mathrm{H_2O_2}$ concentrations, pulp density, temperature and particle size.

These results demonstrate that both MDS and leaching models can be effectively described through computational modelling. Both methods offer a valuable insight into LIB recycling process and can support the design of more sustainable and efficient recovery systems.

Contents

List of Figures

List of Tables

Nomenclature

Abbreviations

Abbreviation	Definition
Cl	Chloride
Co	Cobalt
Co_3O_4	Cobalt(II,III) oxide
$CoSO_4$	Cobalt(II) sulfate
Da number	Damköhler number
H^+	Proton
HCl	Hydrochloric acid
H_2O	Water
H_2O_2	Hydrogen peroxide
H_2SO_4	Sulfuric acid
LIB	Lithium-ion battery
Li	Lithium
$LiCoO_2$	Lithium cobalt oxide
Li_2SO_4	Lithium sulfate
LP	Liquid product
LR	Liquid reactant
MDS	Magnetic density separation
$MnCl_2$	Manganese (II) chloride
O_2	Oxygen
OH^-	Hydroxide ion
ODE	Ordinary differential equation
SCM	Shrinking Core Model
Re number	Reynolds number
Sc number	Schmidt number
Sh number	Sherwood number
SP	Solid product
SR	Solid reactant
w/w	Weight per weight percentage
XPS	X-ray photoelectron spectroscopy

List of Symbols

Symbol	Definition	Units
a_i	Activity of species i	[-]
b	Stoichiometric coefficient	[-]
B	Magnetic field strength	[T]
B_r	Magnetic remanence	[T]
C^*_LRc	Dimensionless concentration of the liquid reactant at the core surface	[-]
C^*_LRb	Dimensionless concentration of the liquid reactant in the bulk	[-]
C_0, C_1	Empirical fitting parameters (diffusion)	[-]
C_i	Concentration of species i	[mol/m^3]
$C_{\mathrm{MnCl_2}}$	Concentration of manganese(II) chloride	[mol/m^3]
$C_{\mathrm{H_2SO_4}}$	Concentration of sulfuric acid	[mol/m^3]
$C_{\mathrm{H_2O_2}}$	Concentration of hydrogen peroxide	[mol/m^3]
$C_{\mathrm{Li^+}}$	Concentration of lithium ions	[mol/m^3]
$C_{\mathrm{Co^{2+}}}$	Concentration of cobalt ions	[mol/m^3]
$C_{\mathrm{H^+,bulk}}$	Proton concentration in the bulk	[mol/m^3]
$C_{\mathrm{H^+,core}}$	Proton concentration at the core	[mol/m^3]
$C_{\mathrm{LiCoO_2}}$	Concentration of $LiCoO_2$	[mol/m^3]
$C_{\mathrm{Co_3O_4}}$	Concentration of Co_3O_4	[mol/m^3]
$C_{\mathrm{Co_3O_4},0}$	Initial concentration of Co_3O_4	[mol/m^3]
C_{SR0}	Initial concentration of solid reactant	[mol/m^3]
c	Acid concentration (used in empirical correlations)	[mol/L]
D	Thickness of cylindrical magnet	[mm]
d	Particle diameter	[μm]
$D_{\mathrm{H^+}}$	Diffusion coefficient of protons	[m^2/s]
$D_{\mathrm{H_2SO_4}}$	Diffusion coefficient of sulfuric acid	[m^2/s]
D_m	Molecular diffusion coefficient	[m^2/s]
D_eff	Effective diffusion coefficient	[m^2/s]
D_0	Reference diffusion coefficient	[m^2/s]
E_a	Activation energy	[J/mol]
E^0	Standard electrode potential	[V]
F_buoy	Buoyancy force	[N]
F_drag	Drag force	[N]
F_m	Magnetic force	[N]
F_z	Gravitational force	[N]
g	Gravitational acceleration	[m/s^2]
ΔG	Gibbs free energy change	[J/mol]
H	Magnetic field strength	[A/m]
k	General reaction rate constant	[varies]
k_1	Rate constant for reaction 1 (acid)	[m/s]
k_2	Rate constant for reaction 2 (acid + solid)	[m^{2}mol$^{-2/3}$s^{-1}]
k_3	Rate constant for reaction 3 (acid + H_2O_2)	[m^{5}mol$^{-4/3}$s^{-1}]
k_4	Rate constant for reaction 4 (acid + solid + H_2O_2)	[m^{8}mol$^{-8/3}$s^{-1}]
k_D	Diffusional tortuosity factor	[m^{-1}]
k_m	Mass transfer coefficient	[m/s]
M	Magnetization	[A/m]
$M_{\mathrm{LiCoO_2}}$	Molar mass of $LiCoO_2$	[kg/mol]
$M_{\mathrm{Co_3O_4}}$	Molar mass of Co_3O_4	[kg/mol]
$m_{\mathrm{LiCoO_2}}$	Mass of $LiCoO_2$	[kg]
m_p	Mass of a particle	[kg]

Symbol	Definition	Units
m_{sol}	Mass of solution	[g]
$m_{\mathrm{H_2O_2}}$	Mass of hydrogen peroxide	[g]
n	Reaction order	[-]
N_{p}	Number of particles	[-]
$N_{\mathrm{LR}}, N_{\mathrm{SR}}$	Moles of liquid and solid reactant	[mol]
r_1, r_2, r_3, r_4	Reaction rates for reactions 1–4	[mol/(m^{3}s)]
R	Universal gas constant	[J/mol·K]
R_{p}	Reaction rate per particle	[mol/s]
R	Radius of cylindrical magnet	[mm]
r_{c}^*	Dimensionless core radius	[-]
r_{c}	Shrinking core radius	[m]
r_{s}	Initial particle radius	[m]
r_{np}	Nanoparticle radius	[m]
r_{c}^*	Dimensionless core radius	[-]
t	Time	[s]
T	Temperature	[K]
U_{f}	Fluid velocity	[m/s]
U_{p}	Particle velocity	[m/s]
v	General velocity	[m/s]
v_{pz}	Vertical particle velocity component	[m/s]
v_{py}	Horizontal particle velocity component	[m/s]
V	Volume	[m^3]
V_{r}	Reactor volume	[m^3]
V_{solid}	Volume of solid material (e.g., Co_3O_4)	[m^3]
V_{void}	Void volume in porous shell	[m^3]
V_{shell}	Volume of the shell (porous layer)	[m^3]
V_{particle}	Volume of a single particle	[m^3]
V_{total}	Total particle volume	[m^3]
$V_{\mathrm{H_2O_2,sol}}$	Volume of H_2O_2 in solution	[mL]
X	Leaching efficiency (extraction yield)	[%]
z	Distance from magnet surface	[mm]
γ_i	Activity coefficient of species i	[-]
μ	Dynamic viscosity of fluid	[Pa·s]
$\bar{\mu}$	Mean particle size	[μm]
μ_0	Magnetic permeability of vacuum	[N/A^2]
ϵ	Porosity of the crust layer	[-]
τ	Dimensionless time	[-]
σ	Standard deviation of particle size	[μm]
χ_{p}	Magnetic susceptibility of particle	[-]
χ_{m}	Magnetic susceptibility of medium	[-]
χ^{V}	Volume magnetic susceptibility	[-]
Da	Damköhler number	[-]
Sh	Sherwood number	[-]

1

Introduction

1.1. Motivation

As the world transitions from fossil fuels towards renewable energy sources, the demand for energy-storage technologies is growing rapidly. Among these technologies, lithium-ion batteries (LIBs) have become the dominant rechargeable battery due to their high energy density, long lifespan, high efficiency and low self-discharge rate [7]. LIBs are used in mobile phones, grid-scale storage systems and electric vehicles (EVs). To illustrate the rapid expansion of the sector, the global LIB market was worth 64.84 billion dollars in 2023 and is expected to grow to 446.85 billion dollars in 2032 [8].

However, the rapid expansion of LIB usage brings a mounting pressure on the supply of critical raw materials. The cathode typically contains metals such as lithium, cobalt, manganese and nickel. These are all classified as critical raw materials by the European commission due to their economic value and the risk of supply shortages [9]. Recycling these metals from LIBs is therefore crucial to reduce dependency on mining and extend the availability of these metals [10].

While cathode recycling has drawn significant attention, graphite, the dominant anode material, is equally important, as it stores lithium ions during charging and is essential to battery performance. LIBs can contain 11 times more graphite than lithium by weight [11]. China currently dominates the graphite supply chain, producing more than 75 % of global graphite and nearly 90% of the flake graphite used in LIBs [12] [13]. This dominant position in the graphite market places Europe and the United States in a vulnerable position, since they heavily rely on imports of graphite. For instance, between 2019 and 2022, 42% of U.S. graphite imports originated from China [13]. This dependency has become more pronounced since December 2023, when China imposed export permits on high-purity graphite, posing risks to supply stability and underscore the need to diversify supply chains [14]. As a result, graphite is now also considered as a critical raw material, not due to scarcity, but because of geopolitical and supply chain risks [15]. The efficient separation and recovery of materials from spent LIBs remains technically challenging due to high costs and chemical inefficiencies. Predictive models are therefore essential to understand and optimize these recovery methods, with fewer experimental trials.

Beyond material availability, environmental impact and new regulations further highlight the urgency of improving battery recycling. LIBs have a limited lifespan and by 2040 the accumulated capacity of spent LIBs is expected to reach 1300 GWh [16]. These batteries contain heavy metals and organic chemicals, that pose risks to human and environmental health if not properly managed [17]. To address this growing volume of battery waste, the European Union has introduced a new, strict regulation for batteries, covering the entire lifecycle with a strong emphasis on metal recovery [18].

In this context, developing effective methods to recover lithium, cobalt and graphite from spent LIBs are not only environmentally necessary but also of strategic importance. This thesis contributes to that by modelling magnetic density separation and hydrometallurgical leaching, to identify which process parameters affect material separation and dissolution, supporting more efficiency recovery of these critical materials.

1.2. Literature review

This chapter provides the theoretical background information for the models developed in this study. First, an overview of the Magnetic Density Separation technique is presented, detailing its working principle and relevance for element recovery. This is followed by a description of the fundamental principles of the Shrinking Core Model, a method commonly used to describe the leaching behaviour of solid particles during chemical reactions.

1.2.1. Magnetic density separation

Magnetic Density Separation (MDS) is a technique to separate particles based on differences in both density and magnetic susceptibility. Magnetic phenomena in materials result from the motion of electric charges, in particular the spin and orbital motion of electrons around the nucleus. The sum of the microscopic magnetic moments produces a macroscopic property known as magnetization, denoted by M [19]. In magnetostatics, the total magnetic field B within a material is related to the applied magnetic field H and magnetization by:

$$B = \mu_0(H + M) \tag{1.1}$$

in which μ_0 is the permeability of free space. In non-magnetic materials, where $M = 0$, this simplifies to $B = \mu_0 H$. An important quantity in the context of MDS is the magnetic susceptibility (χ). This dimensionless quantity indicates how easily a material becomes magnetized when subjected to an external magnetic field:

$$M = \chi H \tag{1.2}$$

Materials with $\chi > 0$ become magnetized in the same direction as the applied field, while those with $\chi < 0$ are magnetized in the opposite direction [19] [20]. Magnets can be classified into diamagnetic, paramagnetic and ferromagnetic materials. Each type exhibits distinct magnetic behaviour in an external magnetic field.

Diamagnetic materials contain only paired electrons with opposite spins, causing their magnetic moments to cancel out. The materials have a weak negative susceptibility and are repelled by the magnetic fields. Their magnetic properties disappear when the magnetic fields are removed.

Paramagnetic materials have unpaired electrons that generate a net magnetic moment. However, there is no overall net magnetic moment because thermal vibrations cause the magnetic moments to point in random directions. Paramagnetic materials have a small positive magnetic susceptibility. When exposed to a magnetic field, the magnetic moments partially align with the field, causing the materials to be weakly attracted to the magnets. However, for paramagnets these magnetic properties are temporary and disappear when the magnetic field is removed [21]. An example of a paramagnetic material is aluminium.

Ferromagnets also contain unpaired electrons, but their magnetic moments are grouped into regions called magnetic domains. In a demagnetized state, the domains are randomly oriented resulting in no net magnetic field. When a magnetic field is applied, all domains align in the direction of the field, leading to a strong magnetization and a large positive magnetic susceptibility. When the magnetic field is removed, some magnetic domains remain aligned, which explains why ferromagnetic materials can retain their magnetic properties [22].

The magnetic susceptibility influences the particle behaviour in MDS, which separates particles based on differences in both density and magnetic properties. In this method, particles are suspended in a paramagnetic liquid that responds to an external magnetic field. A permanent magnet placed at the bottom of the setup generates a vertically varying magnetic field, resulting in a magnetic field gradient. This gradient acts on both the fluid and the suspended particles. As a result, particles with varying density and magnetic susceptibility experience different forces and move to different equilibrium positions. The net force acting on a particle, $\vec{F}_{\mathrm{net}}$, is the sum of the gravitational force, magnetic force, buoyancy force and drag force and is expressed as:

$$\vec{F}_{\mathrm{net}} = \vec{F}_{\mathsf{z}} + \vec{F}_{\mathsf{buoy}} + \vec{F}_{\mathsf{m}} + \vec{F}_{\mathsf{drag}} \tag{1.3}$$

To fully capture the dynamics of particle motion, it is essential to also consider the forces acting on the surrounding medium. The forces acting on the particle and surrounding medium are illustrated in Figure 1.1.

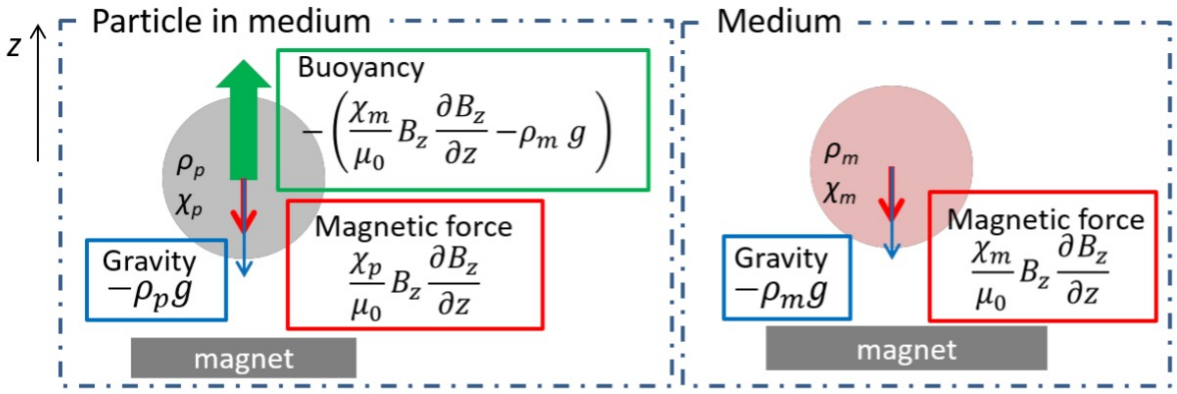

Figure 1.1: Magneto-Archimedes effect [1]

The gravitational force ($\vec{F}_\mathrm{z}$) acting on the particle is downward and given by:

$$\vec{F}_\mathrm{g} = -\rho_\mathrm{p} g V \tag{1.4}$$

Where ρ_p is the density of the particle, V is the volume of the particle, and g is the gravitational acceleration. The gravitational force acting on the medium is similar in form and described as:

$$\vec{F}_\mathrm{g} = -\rho_\mathrm{m} g V \tag{1.5}$$

in which ρ_m is the density of the medium. The magnetic force experienced by the particle arises from the magnetic susceptibility of the particle interacting with the magnetic field gradient and is expressed as:

$$\vec{F}_\mathrm{m} = \frac{\chi_\mathrm{p}}{\mu_0} B_\mathrm{z} \frac{\partial B_\mathrm{z}}{\partial z} V \tag{1.6}$$

Here, χ_p is the magnetic susceptibility of the particle, μ_0 is the magnetic permeability of free space and $B_\mathrm{z}\frac{\partial B_\mathrm{z}}{\partial z}$ represents the vertical magnetic field gradient. In this setup, the magnetic field decreases with height, meaning $\frac{\partial B_\mathrm{z}}{\partial z} < 0$. Consequently:

- For paramagnetic particles ($\chi_\mathrm{p} > 0$), the magnetic force is directed downward (attractive force).
- For diamagnetic particles ($\chi_\mathrm{p} < 0$), the magnetic force is directed upward (repulsive force)

In a magnetic density separation experiment a paramagnetic medium is typically used. Characterized by $\chi_\mathrm{m} > 0$ and $B_\mathrm{z}\frac{\partial B_\mathrm{z}}{\partial z} < 0$, the resulting magnetic force acting on the medium is negative which corresponds to an attractive force. According to Archimedes' principle, buoyancy force equals the weight of the fluid displaced by the particle. When both gravitational and magnetic contributions are considered, this results in:

$$\begin{aligned} \vec{F}_\text{weight, medium} &= \left(\frac{\chi_m}{\mu_0} B_z \frac{\partial B_z}{\partial z} - \rho_m g\right) V \\ \vec{F}_\text{weight, medium} &= -\vec{F}_\text{buoy} \\ \vec{F}_\text{buoy} &= -\left(\frac{\chi_m}{\mu_0} B_z \frac{\partial B_z}{\partial z} - \rho_m g\right) V \end{aligned} \tag{1.7}$$

The drag force arises from the relative motion between a particle and the surrounding fluid. In particle-fluid flows, the particle velocity U_p is normally different than the fluid velocity U_f. The velocity difference leads to an unbalanced pressure distribution and viscous stress on the particle surface, resulting in a force that opposes the motion of the particle and is known as the drag force [23]:

$$\vec{F}_\mathrm{drag} = \frac{1}{2} \mathrm{C_D} A \rho_\mathrm{f} \left|U_\mathrm{f} - U_\mathrm{p}\right| \left(U_\mathrm{f} - U_\mathrm{p}\right) \tag{1.8}$$

in which C_{D} is the drag coefficient, A is the cross-sectional area of the particle perpendicular to the incoming flow (for a sphere, $\mathrm{A} = \pi \mathrm{d}^2/4$), ρ_{f} is the fluid density and $U = U_{\mathrm{f}} - U_{\mathrm{p}}$ is the relative velocity. The drag coefficient depends on the Reynolds number, which is a dimensionless number that represents the ratio of inertial to viscous forces:

$$Re = \frac{\rho_{\mathrm{f}} U d}{\mu} \tag{1.9}$$

Here, d is the particle diameter μ is the dynamic viscosity of the fluid. Based on the Re number, three regimes for C_{D} can be identified [2]:

1. **Stokes flow regime ($Re < 1$):** Laminar flow, viscous forces dominate.

   $C_D = \dfrac{24}{Re}$ for $Re < 1$

2. **Transitional regime ($1 < Re < 2000$):** This regime bridges the gap between purely viscous Stokes flow and turbulent flows.

   $C_D = \dfrac{24}{Re}\left(1 + 1.935 Re^{0.63}\right)$ for $1 < Re < 285$

   $C_D = \dfrac{24}{Re}\left(1 + 0.15 Re^{0.687} + 0.42 Re^{0.427}\right)$ for $285 < Re < 2000$

3. **Newton's regime ($Re > 2000$):** Turbulent flow, inertial forces dominate.

   $C_D = 0.4$–0.5 for $2000 < Re < 3.5 \times 10^5$

In Figure 1.2 the drag coefficient for the different regimes is shown.

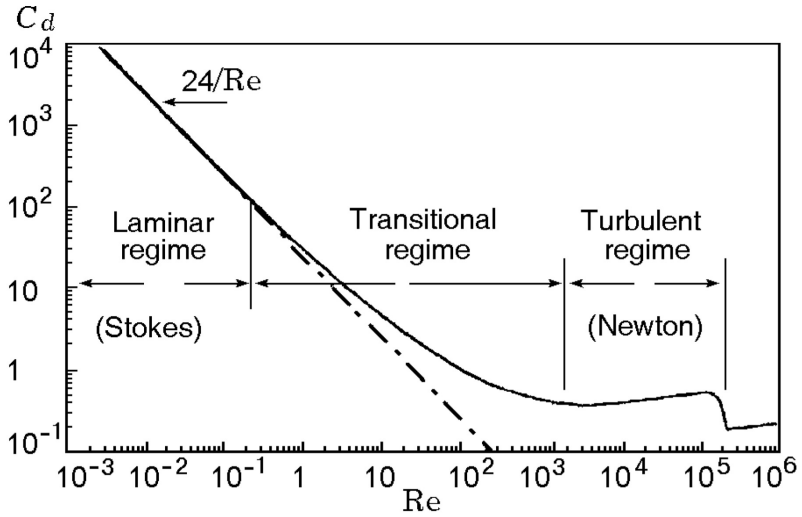

Figure 1.2: Drag coefficient as function of Reynolds number [2]

For a spherical particle, the drag force can be simplified as [24] [25]:

$$F_{\mathrm{drag}} = \frac{1}{8} C_D \pi d^2 U^2 \rho_f \tag{1.10}$$

In the Stokes flow regime, by substituting $C_D = \frac{Re}{24} = \frac{24\mu}{\rho_f U d}$, the drag force reduces to:

$$F_{\mathrm{drag}} = \frac{24 \mu \rho_f U^2 \pi d^2}{8 \rho_f U d} = 3 \mu U \pi d \tag{1.11}$$

In addition to gravitational, magnetic, buoyant and drag forces, particles may also experience added mass, history, lift and interaction forces (i.e. particle-particle or particle-wall interactions). To simplify

the analysis, one-way coupling is assumed. This means that the fluid influences the motion of the particles, but the particles do not influence the motion of the fluid [26]. This assumption is valid for dilute suspensions with a local volume fraction below 10^{-5} and in laminar conditions [27]. At higher concentrations, particle-interactions and fluid disturbance become significant, requiring a more complex force balance. For a dilute particle suspension, substituting the expressions for all relevant forces into the net force balance (Equation 1.3) yields:

$$\vec{F}_{\mathrm{net}} = \left[-\rho_{\mathrm{p}} g + \frac{\chi_{\mathrm{p}}}{\mu_0} B_{\mathrm{z}} \frac{\partial B_{\mathrm{z}}}{\partial z} - \left(\frac{\chi_{\mathrm{m}}}{\mu_0} B_{\mathrm{z}} \frac{\partial B_{\mathrm{z}}}{\partial z} - \rho_{\mathrm{m}} g\right)\right] V + 3\pi\mu d U \tag{1.12}$$

If the particle reaches a steady-state position and stops moving ($U = 0$), the drag force disappears and the force balance simplifies to:

$$\vec{F}_{\mathrm{net}} = \left[-\rho_{\mathrm{p}} g + \frac{\chi_{\mathrm{p}}}{\mu_0} B_{\mathrm{z}} \frac{\partial B_{\mathrm{z}}}{\partial z} - \left(\frac{\chi_{\mathrm{m}}}{\mu_0} B_{\mathrm{z}} \frac{\partial B_{\mathrm{z}}}{\partial z} - \rho_{\mathrm{m}} g\right)\right] V \tag{1.13}$$

Magnetic and gravitational forces acting on the medium are negative, resulting in a positive buoyancy force on the particle. The magnetic susceptibility of the paramagnetic medium increases the downward force acting on it, enhancing the buoyancy force on the particle, making it stronger than it would be under gravity alone.

A particle levitates when the buoyancy force exceeds the sum of the magnetic and gravitational forces ($\vec{F}_{\mathrm{net}} \geq 0$). When the three forces balance, the particle will levitate at a stable height when the net force acting on it is zero ($\vec{F}_{\mathrm{net}} = 0$). Applying the levitation condition ($\vec{F}_{\mathrm{net}} \geq 0$) to the force balance results in:

$$(\chi_{\mathrm{p}} - \chi_{\mathrm{m}}) B_{\mathrm{z}} \frac{\partial B_{\mathrm{z}}}{\partial z} \geq (\rho_{\mathrm{p}} - \rho_{\mathrm{m}}) g \mu_0 \tag{1.14}$$

For diamagnetic materials, χ_p is negative and significantly smaller in magnitude than χ_m, making the term $(\chi_p - \chi_m)$ a negative value. Rearranging the inequality gives

$$B_z \frac{\partial B_z}{\partial z} \leq \frac{(\rho_p - \rho_m) g \mu_0}{\chi_p - \chi_m} \tag{1.15}$$

This inequality describes the relationship between the magnetic field strength and its vertical gradient, required for particle levitation. This means that a lighter (lower ρ_{p}) or more diamagnetic particle (more negative χ_{p}) is easier to levitate. Varying the concentration of the medium also alters its magnetic susceptibility χ_m. This directly affects the levitation condition in Equation 1.15 and the density-based separation of particles [1].

1.2.2. Shrinking core model

The Shrinking Core Model (SCM) is a widely used framework to describe the consumption of solid particles over time due to dissolution or reaction. The model can be applied in different areas such as pill dissolution in the stomach, catalyst regeneration (restoring catalyst activity by removing deactivating impurities), the development of an ash layer around a burned coal particle or leaching of metals such as lithium (Li) and cobalt (Co) from lithium metal oxide in spent lithium-ion batteries (LIBs) [28]. In this Master's thesis, the primary focus will be on applying the SCM to the leaching of lithium and cobalt from lithium cobalt oxide ($\mathrm{LiCoO_2}$) using sulfuric acid ($\mathrm{H_2SO_4}$) as a leaching agent. Other leaching agents are also analysed. This section provides a generalized overview and context of the SCM, introducing its main parameters and the underlying concepts. Then, it is explained how the concentration of the liquid reactant in the bulk changes over time and finally a non-dimensional analysis is performed in which non-dimensional parameters are introduced to facilitate a broader understanding of the model's applicability.

The SCM was introduced by Yagi and Kuni in 1955 to describe the conversion of solid particles reacting with a gas [29]. The model assumes that the gaseous reactant reacts with the solid from the outside inward, forming a shrinking unreacted core surrounded by a growing product layer. This model is particularly relevant when the solid product does not dissolve in the liquid phase. As a result the external particle size remains constant over time while the core shrinks and an ash layer forms around

the shrinking core [30].

In fluid-solid reactions, the SCM provides a widely used framework that describes the dissolution of solid particles as they react with a fluid. The general reaction can be written in the following form:

$$\mathrm{LR(l)} + \mathrm{bSR(s)} \rightarrow \mathrm{LP(l)} + \mathrm{SP(s)} \tag{1.16}$$

Where b is stoichiometric coefficient. The SCM assumes that the liquid reactant (LR) reacts with the solid reactant (SR), forming a liquid product (LP) and a solid product (SP) around the unreacted shrinking core. [3]. The SCM identifies three processes that control the overall reaction rate:

1. External mass transfer of the LR from the bulk fluid to the particle surface
2. Diffusion of the LR through the porous product layer.
3. Chemical reaction at the shrinking core [31].

Initially, the spherical particle is considered to have a radius r_{s}, suspended in a liquid with bulk concentration C_{LRb}. Over time, the reaction causes the unreacted core radius r_{c} to shrink, reducing its radius to r_{c}. Between r_{c} and r_{s} a porous product layer is formed, and the LR diffuses through this porous layer to the interface at which the chemical reaction takes place. As a result, the concentration of the LR decreases from the bulk fluid (C_{LRb}) to the particle surface (C_{LRs}) and further through the porous product layer to the core interface (C_{LRc}) which is illustrated in Figure 1.3

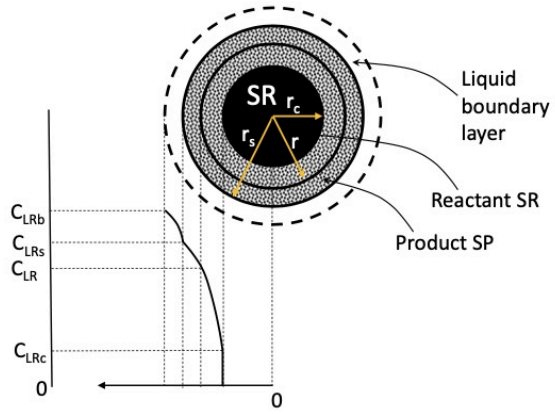

Figure 1.3: Concentration profile of the LR across the radial distribution of the shrinking particle [3]

The SCM is based on the following assumptions to simplify the system. It is assumed that the particle maintains its spherical shape throughout the process and that the densities of the solid reactant and the product are equal, keeping r_{s} constant. Additionally, it is assumed that there exists no liquid region between the unreacted core and the product layer. Furthermore, the velocity of the reaction interface at $r = r_{\mathrm{c}}$ is slow enough relative to the diffusion rate such that the pseudo-steady-state approximation is valid, meaning that the transport rates and reaction rates are assumed to be balanced at every moment. The final assumption is that the reaction rate is proportional to the surface area of the unreacted core. The overall rate of the process is determined by the slowest of the three sequential steps: mass transfer, diffusion or surface reaction. This will be investigated in the following sections.

The mass-transfer of LR through the liquid boundary layer occurs due to the difference in concentration between the LR in the bulk and at the surface. Figure 1.4a illustrates a spherical particle surrounded by a fluid boundary layer. The LR moves from the bulk concentration C_{LRb} towards the surface concentrations C_{LRs}. The corresponding concentration gradient is shown in Figure 1.4b

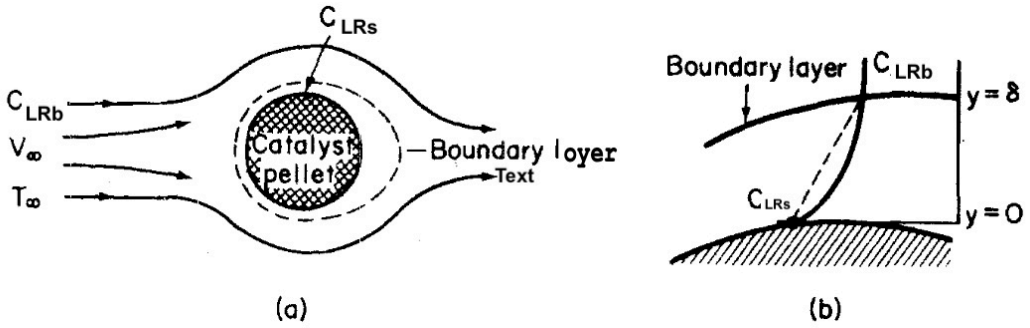

Figure 1.4: Boundary layer around a spherical particle [4].

To simplify the mass transfer process through this boundary layer, the stagnant film model is applied as illustrated in Figure 1.5. This model assumes a uniform film thickness of $\tilde{\delta}$ around the particle and a linear concentration gradient between C_{LRb} and C_{LRs}. The solid line in Figure 1.4 corresponds to the actual concentration gradient and the dashed line to the linear approximation used in the stagnant film model. Fick's law of diffusion describes the molar flux of the LR through the film:

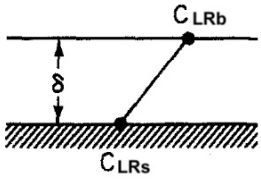

Figure 1.5: Stagnant film model with a linear concentration gradient.
[4]

$$W_{\mathrm{LR}} = -D_m \frac{\partial C}{\partial y} \tag{1.17}$$

For a constant gradient this simplifies to:

$$W_{\mathrm{LR}} = \frac{D_m}{\tilde{\delta}} (C_{\mathrm{LRb}} - C_{\mathrm{LRs}}) \tag{1.18}$$

Here, D_m is the diffusion coefficient of the LR (m^2/s) and $\tilde{\delta}$ is the film thickness. The local mass transfer coefficient is defined by $\tilde{k}_m = \frac{D_m}{\tilde{\delta}}$. To account for spatial variations over the sphere, the average mass transfer coefficient across the particle surface is given by:

$$k_m = \frac{\int_A \tilde{k}_m dA}{A} \tag{1.19}$$

Using this, the average molar flux from the bulk to the surface becomes:

$$W_{\mathrm{LR}} = k_m (C_{\mathrm{LRb}} - C_{\mathrm{LRs}}) \tag{1.20}$$

The total rate of disappearance of the LR per particle is related to this flux by:

$$-r' = -\frac{1}{S} \frac{dN_{\mathrm{LR}}}{dt} = W_{\mathrm{LR}} \tag{1.21}$$

Where $\mathrm{S} = 4\pi r_{\mathrm{s}}^2$ is the total surface area of the particle [32]. This substitution results in:

$$\frac{dN_{\mathrm{LR}}}{dt} = -4\pi r_{\mathrm{s}}^2 k_m (C_{\mathrm{LRb}} - C_{\mathrm{LRs}}) \tag{1.22}$$

These expressions describe the overall mass transfer rate through the boundary layer. Since the LR is consumed in the reaction, the rate is negative.

Once the LR reaches the porous product layer, it continues to diffuse through this layer. This diffusion can be described by Fick's first law of diffusion. In which the effective diffusion coefficient D_e is used, accounting for the increased path length. This law states that the direction of the molar flux is always opposite to the concentration gradient of the particles. The molar flow rate of the LR through the porous product layer is described by:

$$W = -D_e \frac{dC}{dr}\bigg|_{r=r_c} \tag{1.23}$$

Since C_{LR} increases with radial distance, the gradient is positive and D_e is also positive. This results in a net flux which is directed inwards. The rate of disappearance of LR at the core interface is given by:

$$\frac{dN_{\mathrm{LR}}}{dt} = -4\pi r_c^2 D_e \frac{dC_{\mathrm{LR}}}{dr}\bigg|_{r=r_c} \tag{1.24}$$

At the surface of the shrinking core, the LR is consumed in a chemical reaction. The change in the number of moles of LR at the surface is described by the reaction rate. For a general reaction of $aA + bB \rightarrow$ products, the rate is given by:

$$\text{rate} = k[A]^n[B]^m \tag{1.25}$$

where k is the rate constant, n and m the reaction orders and [A] and [B] are the concentrations of the species [33]. When the LR has reached the surface of the shrinking core, the change in the number of moles of LR occurring at the surface is described by the reaction rate. The reaction rate depends on the concentration of the species and the rate constant. The reaction rate also depends on the surface area available for the reaction. A larger surface area exposed to the LR results in a faster reaction. For a first order reaction (n=1), the reaction rate at the surface of a spherical particle can be described as: [32]

$$-r_{\mathrm{LR}} = -\frac{1}{4\pi r_c^2}\frac{dN_{\mathrm{LR}}}{dt} = kC_{\mathrm{LRc}}^{n=1} \tag{1.26}$$

Rearranging results in the following final expression for the consumption of the LR at the surface of the unreacted shrinking core:

$$\frac{dN_{\mathrm{LR}}}{dt} = -4\pi r_c^2 k C_{\mathrm{LRc}} \tag{1.27}$$

The equations for the processes governing the SCM are summarized in Table 1.1. According to the pseudo-steady-state assumption, the rates of the external mass transfer, diffusion through the product layer and the surface chemical reaction are equal. At any given time, the amount of LR that reaches the particle surface, diffuses through the product layer, and reacts at the surface of the shrinking core is the same. The slowest step determines the overall reaction rate.

Table 1.1: Governing equations of the SCM

Process	**Governing Equation**
External mass transfer	$\frac{dN_{\mathrm{LR}}}{dt} = -4\pi r_s^2 k_m (C_{\mathrm{LRb}} - C_{\mathrm{LRs}})$
Diffusion through product layer	$\frac{dN_{\mathrm{LR}}}{dt} = -4\pi r_c^2 D_e \left.\frac{dC_{\mathrm{LR}}}{dr}\right\vert_{r=r_c}$
Chemical reaction at the interface	$\frac{dN_{\mathrm{LR}}}{dt} = -4\pi r_c^2 k C_{\mathrm{LRc}}$

The concentration of the LR at the surface of the unreacted core, denoted by C_{LRc}, is lower than the bulk concentration C_{LRb}. This difference is due to resistances in mass transfer and diffusion. For a

first-order reaction, The concentration C_{LRc} as a function of C_{LRb} is given by:

$$C_{\mathrm{LRc}} = \frac{C_{\mathrm{LRb}}}{1 + \left(\frac{r_{\mathrm{c}}}{r_{\mathrm{s}}}\right)^2 \left(\frac{k}{k_{\mathrm{m}}}\right) + \left(\frac{k r_{\mathrm{c}}}{D_{\mathrm{e}}}\right)\left(1 - \frac{r_{\mathrm{c}}}{r_{\mathrm{s}}}\right)} \tag{1.28}$$

Here, k is the rate constant, k_{m} is the mass transfer coefficient and D_{e} is the effective diffusion coefficient within the porous product layer. This expression is derived under the assumption of a pseudo-steady-state system in which mass transfer, diffusion and surface reaction occur at equal rates. The detailed derivation is given in appendix A.1.

The rate at which the unreacted core r_{c} shrinks over time is governed by the bulk concentration of the LR and influenced by resistances in mass transfer, diffusion and surface reaction. This rate can be described as follows:

$$\frac{dr_{\mathrm{c}}}{dt} = -\frac{bM_{\mathrm{SR}}}{\rho_{\mathrm{s}}} \frac{C_{\mathrm{LRb}}}{\frac{1}{k} + \left(\frac{r_{\mathrm{c}}}{r_{\mathrm{s}}}\right)^2 \left(\frac{1}{k_{\mathrm{m}}}\right) + \left(\frac{r_{\mathrm{c}}}{D_{\mathrm{e}}}\right)\left(1 - \frac{r_{\mathrm{c}}}{r_{\mathrm{s}}}\right)} \tag{1.29}$$

In which ρ_{s} is the density of the SR ($\mathrm{kg/m^3}$) and M_{SR} is the molecular weight of the SR (kg/mol). The full derivation is provided in appendix A.2.

As the reaction progresses, the LR is consumed at the surface of each particle, reducing C_{LRb} over time. To determine the depletion of LR in the bulk, a mole balance is performed over the entire suspension and can be expressed as:

$$\frac{dC_{\mathrm{LRb}}}{dt} = -\frac{3M_{\mathrm{SR}}k}{\rho_{\mathrm{s}} r_{\mathrm{s}}} \left(\frac{r_{\mathrm{c}}}{r_{\mathrm{s}}}\right)^2 C_{\mathrm{SR0}} C_{\mathrm{LRc}}^n \tag{1.30}$$

Here, ρ_{SR} is the number of solid particles per unit volume of suspension and C_{SR0} is the initial molar concentration of the solid particles. The derivation of Equation 1.30 is provided in appendix A.3.

From Equation 1.29 it follows that the shrinkage of the core radius depends on the mass-transfer coefficient k_m through the liquid boundary layer, the effective diffusion coefficient D_e through the porous layer and the rate constant k.

The mass transfer coefficient k_m describes the diffusion of the LR through the boundary layer surrounding the particle and is defined by:

$$k_{\mathrm{m}} = \frac{\mathrm{Sh}\, D_{\mathrm{m}}}{r_{\mathrm{s}}} \tag{1.31}$$

in which Sh is the Sherwood number which will is discussed further in subsection 1.2.3, D_{m} is the molecular diffusion coefficient of the LR and r_{s} the radius of the particle.

The diffusion through the porous product layer is driven by a concentration gradient and is more complex due to additional resistances. The path length is extended (tortuosity) and the available cross-section area for diffusion is reduced since only the pores contribute to transport. These effects are captured by the effective diffusion coefficient defined by: [4]:

$$D_{\mathrm{e}} = \frac{D_{\mathrm{m}}\, \varepsilon\, \sigma}{\tau} \tag{1.32}$$

where ε is the porosity (fraction of void volume), τ is the tortuosity (ratio of actual to shortest path) and σ is the constriction factor (ratio of molecule to pore diameter). In general, direct measurement of these parameters is difficult. Therefore, the Bruggeman model is commonly used as an empirical estimate for D_e. This model assumes a medium composed of two homogeneous, isotropic phases that are randomly distributed, with spherical inclusions in the porous structure and a low solid fraction [34]. The effective diffusion coefficient simplifies under these assumptions to:

$$D_{\mathrm{e}} = D_{\mathrm{m}}\, \varepsilon^{3/2} \tag{1.33}$$

The reaction rate quantifies how quickly a chemical reaction proceeds and depends on the concentration of the reactants and the rate constant k [32]. For a general reaction:

$$a\,\mathrm{A} + b\,\mathrm{B} \rightarrow c\,\mathrm{AB} \tag{1.34}$$

the rate law expresses the relationship between the reaction rate and the reactant concentrations:

$$\mathrm{Rate} = k[\mathrm{A}]^s[\mathrm{B}]^t \tag{1.35}$$

Here, [A] and [B] are the concentrations of the reactants, s and t are the reaction orders. The overall reaction order is $s + t$. When $s + t = 0$, the rate is independent of the species' concentration. The rate constant k is temperature-dependent and is given by the Arrhenius equation:

$$k = k_0 \exp\left(-\frac{E_\mathrm{a}}{RT}\right) \tag{1.36}$$

Here, k_0 is the frequency factor (related to the frequency of collisions), E_a is the activation energy (minimum energy required for a reaction to occur), R is the universal gas constant and T is the absolute temperature. The collision theory describes that a reaction only occurs if particles collide with sufficient energy and proper orientation to overcome the activation barrier [32].

1.2.3. Dimensionless shrinking core model

To generalize the SCM for varying particle sizes and operating conditions, a dimensional analysis is introduced. This simplifies the analysis of the model and highlights the dominant mechanisms, such as mass transfer, diffusion or surface reaction, that govern the overall reaction rate. A first-order reaction ($n = 1$) is assumed and the following dimensionless numbers are defined:

$$C^*_{\mathrm{LRc}} = \frac{C_{\mathrm{LRc}}}{C_{\mathrm{LRb},0}}, \qquad C^*_{\mathrm{LRb}} = \frac{C_{\mathrm{LRb}}}{C_{\mathrm{LRb},0}}, \qquad r^*_\mathrm{c} = \frac{r_\mathrm{c}}{r_\mathrm{s}}, \qquad \tau = \frac{D_\mathrm{m} t}{r_\mathrm{s}^2}, \tag{1.37}$$

$$\mathrm{Da} = \frac{k r_\mathrm{s}}{D_\mathrm{m}}, \qquad \mathrm{Sh} = \frac{k_\mathrm{m} r_\mathrm{s}}{D_\mathrm{m}} \tag{1.38}$$

In which C^*_{LRc} and C^*_{LRb} are the dimensionless LR concentrations at the core and in the bulk, r^*_c is the dimensionless core radius, and τ is the dimensionless time. Da and Sh are the dimensionless Damköhler and Sherwood numbers, respectively. The Sh number is represented by the ratio of the total mass transfer rate, which includes both convection and diffusion, to the diffusive mass transfer rate [35]:

$$\mathrm{Sh} = \frac{k_\mathrm{m}\, r_\mathrm{s}}{D_\mathrm{m}} \tag{1.39}$$

The total mass transfer consists of diffusion, driven by concentration gradients and convection, enhanced by fluid motion. The Sh number can be expressed using the Reynolds and Schmidt numbers:

$$\mathrm{Re} = \frac{\rho\, u\, L}{\mu} \tag{1.40}$$

The dimensionless Reynolds number is the ratio of inertial to viscous forces, where ρ is the fluid density, u is the velocity of the fluid, L is the characteristic length (i.e., the particle's diameter) and μ is the dynamic viscosity of the fluid.

$$\mathrm{Sc} = \frac{\mu}{\rho\, D_\mathrm{m}} \tag{1.41}$$

The dimensionless Schmidt number can be calculated from the ratio of the momentum diffusivity (also known as viscosity) to the mass diffusivity and describes how easily a substance can diffuse through the fluid compared to how the fluid flows. It is an intrinsic fluid property and therefore independent of the system geometry or the fluid dynamics [35]. To describe the mass transfer around a solid spherical particle, the empirical Frössling correlation is commonly used [36]:

$$0 < \mathrm{Re} < 200 \quad \text{and} \quad 0 < \mathrm{Sc} < 250, \quad \mathrm{Sh} = 2 + 0.6\,\mathrm{Re}^{1/2}\,\mathrm{Sc}^{1/3} \tag{1.42}$$

In the context of the SCM, the Sh number quantifies the relative contribution of convection to the mass transfer compared to diffusion in the fluid around the shrinking particle. When convection is negligible (e.g. $u = 0$), the Reynolds number is zero and Sh approaches a value of 2, indicating purely diffusive mass transport. Higher Sh numbers imply an enhancement of convective mass transfer outside of the particle surface. According to the Frössling correlation, for the upper bounds $\mathrm{Re} = 200$ and $\mathrm{Sc} = 250$

the Sh number would become $\mathrm{Sh} \approx 55.56$

The dimensionless Da number describes the ratio of the surface reaction rate to the diffusion rate through the porous product layer. For a first order reaction ($n = 1$) it is given by [3].

$$\mathrm{Da} = \frac{k\, r_\mathrm{s}}{D_\mathrm{m}} \tag{1.43}$$

A small Da number ($\ll 1$), indicates that the process is reaction-limited, while a high Da number ($\gg 1$) means that the reactants are consumed faster than they can diffuse to the surface, indicating a diffusion-limited process.

With the dimensionless numbers defined, the analysis can now proceed. The dimensionless form of the LR concentration at the unreacted core surface is derived in appendix A.5 and be written as:

$$C^*_{\mathrm{LRc}} = \frac{C^*_{\mathrm{LRb}}}{1 + (r^*_\mathrm{c})^2 \left(\frac{\mathrm{Da}}{\mathrm{Sh}}\right) + \frac{\mathrm{Da}}{\varepsilon^{3/2}}\, r^*_\mathrm{c}\,(1 - r^*_\mathrm{c})} \tag{1.44}$$

The dimensionless rate of change of the shrinking radius, derived in appendix A.5, is expressed as:

$$\frac{dr^*_\mathrm{c}}{d\tau} = -\left(\frac{bM_{\mathrm{SR}}\mathrm{Da}\, C_{\mathrm{LRb},0}}{\rho_{\mathrm{SR}}}\right)(C^*_{\mathrm{LRc}})^{n=1} \tag{1.45}$$

Substituting Equation 1.44 into Equation 1.45 gives

$$\frac{dr^*_\mathrm{c}}{d\tau} = -\left(\frac{bM_{\mathrm{SR}}\mathrm{Da}\, C_{\mathrm{LRb},0}}{\rho_{\mathrm{SR}}}\right)\frac{C^*_{\mathrm{LRb}}}{1 + (r^*_\mathrm{c})^2 \left(\frac{\mathrm{Da}}{\mathrm{Sh}}\right) + \frac{\mathrm{Da}}{\varepsilon^{3/2}}\, r^*_\mathrm{c}\,(1 - r^*_\mathrm{c})} \tag{1.46}$$

The dimensionless form of the LR bulk concentration, derived in appendix A.6 becomes:

$$\frac{dC^*_{\mathrm{LRb}}}{d\tau} = -\left(\frac{3M_{\mathrm{SR}}C_{\mathrm{SR0}}\mathrm{Da}}{\rho_\mathrm{s}}\right)C^{*n}_{\mathrm{LRc}}r^{*2}_\mathrm{c} \tag{1.47}$$

The bulk concentration of the LR can be expressed as a function of the dimensionless core radius by eliminating time using the chain rule:

$$\frac{dC^*_{\mathrm{LRb}}}{d\tau} = \frac{dC^*_{\mathrm{LRb}}}{dr^*_\mathrm{c}} \cdot \frac{dr^*_\mathrm{c}}{d\tau} \quad \Rightarrow \quad \frac{dC^*_{\mathrm{LRb}}}{dr^*_\mathrm{c}} = \frac{\frac{dC^*_{\mathrm{LRb}}}{d\tau}}{\frac{dr^*_\mathrm{c}}{d\tau}} \tag{1.48}$$

Substituting the expressions for $dC^*_{\mathrm{LRb}}/d\tau$ and $dr^*_\mathrm{c}/d\tau$ yields:

$$\frac{dC^*_{\mathrm{LRb}}}{dr^*_\mathrm{c}} = \frac{3C_{\mathrm{SR0}}}{bC_{\mathrm{LRb},0}}r^{*2}_\mathrm{c} \tag{1.49}$$

Integrating this with the initial boundary condition at $C^*_{\mathrm{LRb}} = 1$ at $r^*_\mathrm{c} = 1$ gives:

$$C^*_{\mathrm{LRb}} = 1 - \frac{C_{\mathrm{SR0}}}{bC_{\mathrm{LRb},0}}(1 - r^{*3}_\mathrm{c}) \tag{1.50}$$

From Equation 1.30 it is evident the rate of change of the LR concentration in the bulk depends on the shrinking radius of the unreacted core r_c. However, tracking the evolution of r_c over time is difficult, since it depends on the concentration of the LR in the bulk. So this creates a coupling between C_{LRb} and r_c because:

- The rate of change of C_{LRb} depends on r_c
- The rate of change of r_c depends on C_{LRb}

The dimensionless method can handle this interdependence more effectively. It allows simultaneous tracking of how the dimensionless radius r^*_c and dimensionless LR concentration in the bulk C^*_{LRb} evolve with respect to dimensionless time τ. This formulation decouples the variables, enabling simultaneous tracking of both parameters over time. This is obtained by substituting Equation 1.50 into Equation 1.46, which yields:

$$\frac{dr^*_\mathrm{c}}{d\tau} = -\left(\frac{bM_{\mathrm{SR}}\mathrm{Da}}{\rho_{\mathrm{SR}}}\right)\frac{C_{\mathrm{LRb},0} - \frac{C_{\mathrm{SR0}}}{b}(1 - r^{*3}_\mathrm{c})}{1 + (r^*_\mathrm{c})^2 \left(\frac{\mathrm{Da}}{\mathrm{Sh}}\right) + \frac{\mathrm{Da}}{\varepsilon^{3/2}}\, r^*_\mathrm{c}(1 - r^*_\mathrm{c})} \tag{1.51}$$

1.3. Problem statement and objective

The rising demand for LIBs, which are essential for energy storage in applications such as electric mobility and renewable energy integration, has led to concerns about the long-term availability of essential materials such as lithium, cobalt and graphite. Today, the EU is still heavily reliant on non-EU countries for the import of these critical materials. This research aims to explore sustainable and scalable recycling methods to recover active materials from spent LIBs, reducing dependence on raw material extraction and mitigating environmental impact. The specific objective is outlined as follows:

Research objective

Investigate the recovery of valuable materials from spent lithium-ion batteries through developing computational models for two processes:
1. Magnetic density separation is used to simulate the levitation and separation behaviour of graphite particles suspended in a paramagnetic liquid.
2. A shrinking core model is applied to investigate the leaching behaviour of $\mathrm{LiCoO_2}$ particles using sulfuric acid, particularly focussing on lithium and cobalt recovery.

The research takes a twofold approach to recovering valuable materials from spent LIB. First, it focuses on direct recycling by investigating magnetic density separation, which is a method used to separate graphite from cathode materials based on a difference in density. It offers a more sustainable alternative to classical dense media separation which relies on expensive and viscous liquids.

Research question 1

Can computational modelling predict the levitation behaviour of graphite in a Magnetic Density Separation system, and how well does it align with experimental observations?

To answer this research question, the following sub questions are addressed.

- SQ1) How does the magnetic susceptibility of $\mathrm{MnCl_2}$ affect the levitation height of graphite particles in a paramagnetic medium?
- SQ2) How does the particle size affect the levitation height and settling time of graphite particles in a paramagnetic medium?
- SQ3) To what extent does the simulation reproduce experimental trends in vertical graphite clustering and lateral distribution?

Secondly, this study investigates the recovery of lithium and cobalt through hydrometallurgical leaching. A shrinking core model is used to describe the leaching of $\mathrm{LiCoO_2}$ particles in sulfuric acid. The model captures the physical and chemical processes which govern the leaching efficiency such as mass transfer, diffusion and kinetics.

Research question 2

Can a Shrinking Core Model predict lithium and cobalt recovery from $\mathrm{LiCoO_2}$ during sulfuric acid leaching and how well does it replicate experimental results across varying conditions?

To answer this research question, the following sub questions are addressed.

- SQ4) Which parameters affect the leaching time and efficiency of $\mathrm{LiCoO_2}$ particles most according to the dimensionless shrinking core model?
- SQ5) How does the shrinking core model with varying crust improve the representation of diffusion and reaction processes compared to the dimensionless model?
- SQ6) To what extent does the shrinking core model with a varying crust replicate experimental leaching trends for $\mathrm{LiCoO_2}$ in sulfuric acid, such as lithium and cobalt recovery under varying operational conditions?

2

Modelling Magnetic Density Separation

This chapter presents the model developed to simulate the Magnetic Density Separation (MDS) process to recover graphite particles suspended in a paramagnetic manganese (II) chloride ($MnCl_2$) solution. The first section investigates the magnetic susceptibility of aqueous $MnCl_2$ solutions at varying concentrations. Values reported in the literature are compared to experimental results from a previous study to validate their use in MDS simulations. Then, a particle tracking model is developed to simulate the motion of graphite particles under the influence of a magnetic field. The model uses a magnetic field obtained from COMSOL and validated against the analytical solution. Subsequently, a detailed explanation of the simulation framework is provided, outlining the modelling assumptions, velocity calculations and particle tracking. Finally, the results are presented, highlighting the equilibrium position of particles, the average time it takes to reach equilibrium and how this depends on particle size. The following sub questions will be addressed in this chapter:

SQ1) How does the magnetic susceptibility of $MnCl_2$ affect the levitation height of graphite particles in a paramagnetic medium?

SQ2) How does the particle size affect the levitation height and settling time of graphite particles in a paramagnetic medium?

SQ3) To what extent does the simulation reproduce experimental trends in vertical graphite clustering and lateral distribution?

2.1. Magnetic susceptibility calculations

Manganese(II) chloride ($MnCl_2$) was selected as the paramagnetic medium, which is commonly used in magnetic density separation experiments. This choice is motivated by its low cost, strong magnetic susceptibility and optical transparency, essential for observing particle levitation height. For the density of aqueous $MnCl_2$ solutions at 1.013 bar and T=25 °C similar results are reported in the literature [37] [38]. Figure 2.1 shows the solution density as a function of concentration.

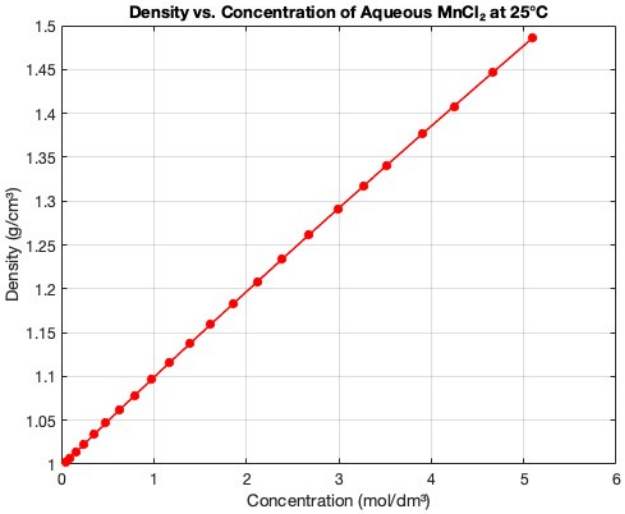

Figure 2.1: Density of $\mathrm{MnCl_2}$ as a function of concentration

The maximum solubility of $\mathrm{MnCl_2}$ in water at room temperature (T=25°C) is reported to be 723 g/L [39]. Given that the molar mass of $\mathrm{MnCl_2}$ is 125.844 g/mol, the corresponding saturation concentration is:

$$C_{\mathrm{MnCl_2},max} = \frac{723}{125.844} \approx 5.75\,\mathrm{mol/L} \tag{2.1}$$

which represents the maximum achievable concentration of $\mathrm{MnCl_2}$ in water. This concentration limits the maximum magnetic susceptibility in the $\mathrm{MnCl_2}$ solution. The magnetic susceptibility of the paramagnetic medium was calculated using Equation 2.2; [40]:

$$\chi^{\mathrm{V}}_{\mathrm{MnCl_2,aq}} = \chi^{\mathrm{M}}_{\mathrm{MnCl_2,aq}} \cdot [\mathrm{MnCl_2}] + \chi^{\mathrm{V}}_{\mathrm{H_2O}} \tag{2.2}$$

In which

- $\chi^{\mathrm{V}}_{\mathrm{MnCl_2,aq}}$ is the dimensionless volume magnetic susceptibility of the solution
- $\chi^{\mathrm{M}}_{\mathrm{MnCl_2,aq}}$ is the molar susceptibility of the aqueous $\mathrm{MnCl_2}$
- $[\mathrm{MnCl_2}]$ is the molar concentration of the $\mathrm{MnCl_2}$ solution = 0 - 5.75 M.
- $\chi^{\mathrm{V}}_{\mathrm{H_2O}}$ is the dimensionless susceptibility of diamagnetic water = -9.05×10^{-6}

In the literature different values for the molar magnetic susceptibility of $\mathrm{MnCl_2}$ are reported. An overview is given in Table 2.1.

Table 2.1: Molar magnetic susceptibilities of $MnCl_2$ from different sources

Source	$\chi^{\mathrm{M}}_{\mathrm{MnCl_2}}$ [L/mol]
Mirica [41]	1.435×10^{-5}
Egami [40]	1.8×10^{-4}
Miura [42]	1.241×10^{-4}

Using the reported values for the molar magnetic susceptibility ($\chi^{\mathrm{M}}_{\mathrm{MnCl_2,aq}}$), the dimensionless volume magnetic susceptibility of the solution ($\chi^{\mathrm{V}}_{\mathrm{MnCl_2,aq}}$) was calculated over a concentration range from 0 to 5.75 mol/L. The results are presented in Figure 2.2 and a significant variation exists in the predicted magnetic susceptibility values.

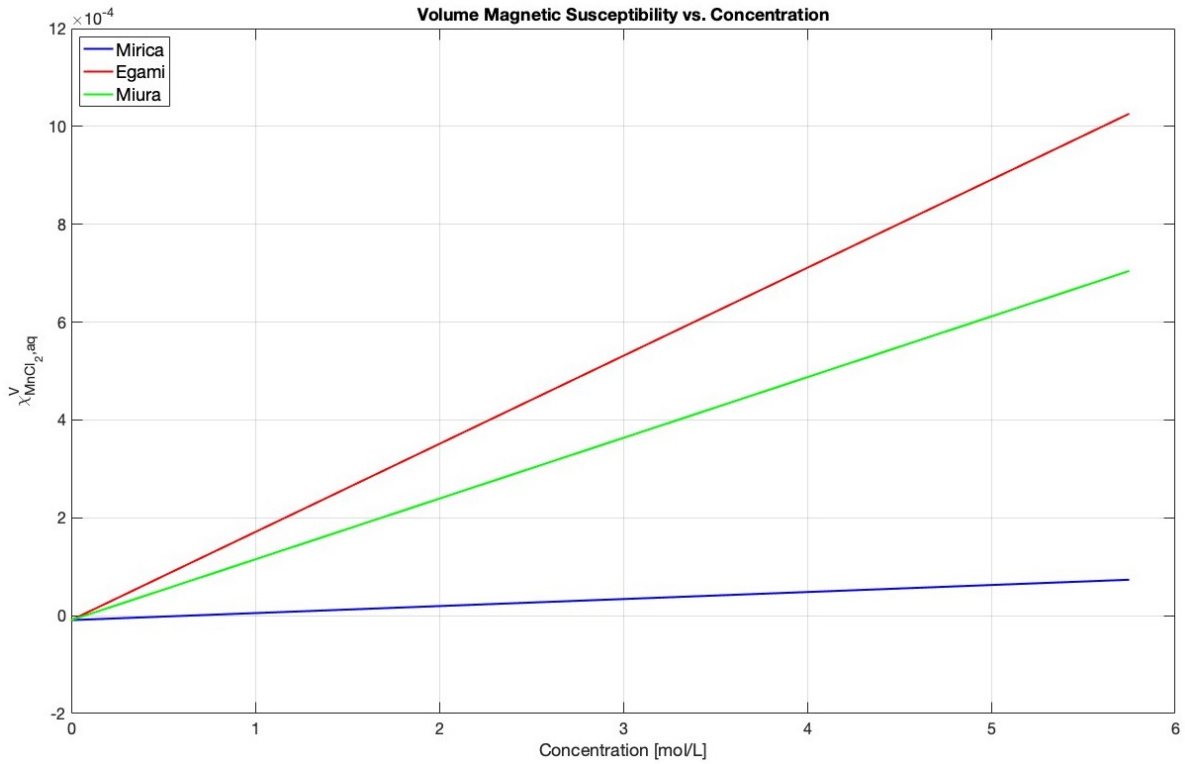

Figure 2.2: Magnetic susceptibility of aqueous $\mathrm{MnCl_2}$ solutions as a function of concentration for different sources.

The experimental magnetic setup consisted of ten N52 neodymium disk magnets stacked vertically along the z-axis. This arrangement produced a strong magnetic field and was previously shown to be the optimal magnetic configuration [5]. The magnetic field along the vertical axis of a cylindrical magnet can be described according to the following equation [43]:

$$B = \frac{B_r}{2}\left(\frac{D+z}{\sqrt{R^2+(D+z)^2}} - \frac{z}{\sqrt{R^2+z^2}}\right) \tag{2.3}$$

in which B_r [T] is the magnetic remanence, which is a material property, D [m] is the thickness of the cylinder, R [m] is the radius and z [m] is the the distance from a pole face on the symmetrical axis. The vertical gradient (in the z-direction) of the magnetic field is described by:

$$\frac{dB_z}{dz} = \frac{B_r}{2}\left(\frac{R^2}{(R^2+(D+z)^2)^{3/2}} - \frac{R^2}{(R^2+z^2)^{3/2}}\right) \tag{2.4}$$

The N52 neodymium disk magnets had a remanent field of $B_r = 1.47$ T, a thickness of $D = 20$ mm (10 stacked 2 mm disks) and a radius of $R = 10$ mm. The magnetic field B_z, its vertical gradient $\frac{\partial B_z}{\partial z}$ and their product over a height range of 0-30 mm above the magnet are shown in Figure 2.3a and Figure 2.3b.

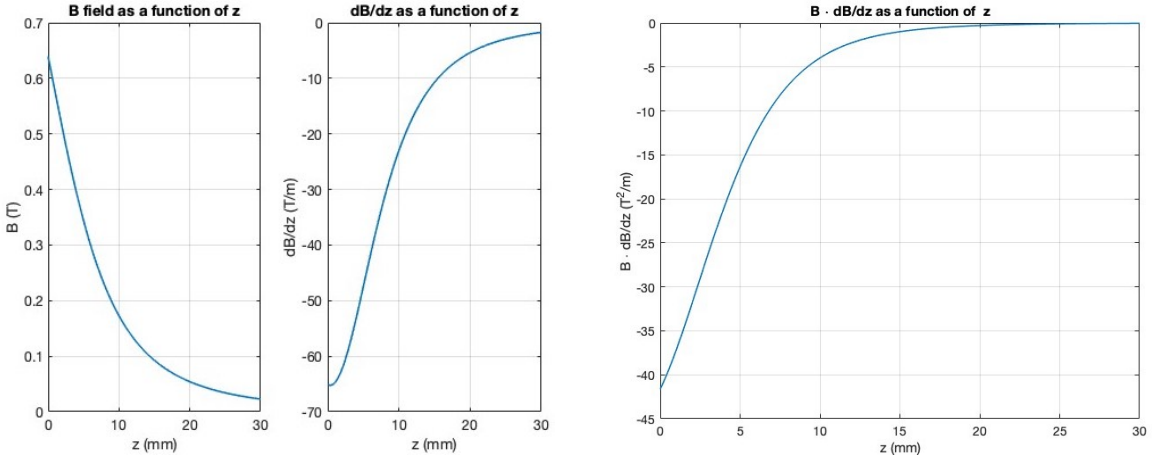

(a) The B-field and dB/dz field from z=0 to z=30mm.

(b) $B_z \cdot \frac{dB_z}{dz}$ from z=0 to z=30mm.

Figure 2.3: Overview of magnetic field parameters used in the analysis

To determine the levitation height of graphite particles, the condition for force balance, introduced in Equation 1.15 must be satisfied:

$$B_z \frac{\partial B_z}{\partial z} \leq \frac{(\rho_s - \rho_m) \cdot g \cdot \mu_0}{\chi_p - \chi_m} \tag{2.5}$$

The left-hand side of the levitation condition was evaluated at each height in Figure 2.3b. The right-hand side depends on physical parameters. The density of graphite is $\rho_p = 2250\,\mathrm{kg/m^3}$. The density of the paramagnetic medium ρ_m varies with the concentration of $\mathrm{MnCl_2}$, ranging from 1.051 to 1.544 g/cm^3. The gravitational acceleration g is 9.81 m/s^2 and the magnetic permeability of free space μ_0 is $4\pi \times 10^{-7}$ N/A^2. The magnetic susceptibility of graphite χ_p is assumed to be zero, while the magnetic susceptibility of the medium χ_m depends on the concentration and are shown in Figure 2.2.

By substituting these values into the right-hand side of Equation 2.5, the minimum magnetic force term ($B_z \frac{\partial B_z}{\partial z}$) required for levitation is computed. Since this term was known at each height, the levitation height corresponding to each concentration can then be determined. Results shown in table B.1 and table B.2 reveal that particle levitation is theoretically possible for concentrations above 2.67 mol/L for Miura and from 1.86 mol/L for Egami. No levitation is possible using Mirica's lower susceptibility values as shown in table B.3 This underlines the importance of determining accurate values for the magnetic susceptibility.

In a previous master thesis, the magnetic susceptibility values for different concentrations of aqueous $\mathrm{MnCl_2}$ were experimentally determined using two methods. The first was the magnetic pendant drop magnet, where the deformation of a droplet of $\mathrm{MnCl_2}$ suspended on a needle was analysed with and without a magnetic field. The difference in the drop deformation was used to calculate the additional magnetic force. Combined with the known magnetic field gradient the magnetic susceptibility of the solution for different concentrations could be calculated. The second method was based on the levitation height of the graphite particles. The levitation height of graphite particles, suspended in $\mathrm{MnCl_2}$ solutions with known concentrations, was measured. By rearranging the levitation condition, the magnetic susceptibility of the medium was calculated for various concentrations. A more detailed description can be found in the thesis by Hooijkaas [5].

The results of both methods are shown in Figure 2.4, plotted alongside the values reported by Egami, Miura, and Mirica, respectively.

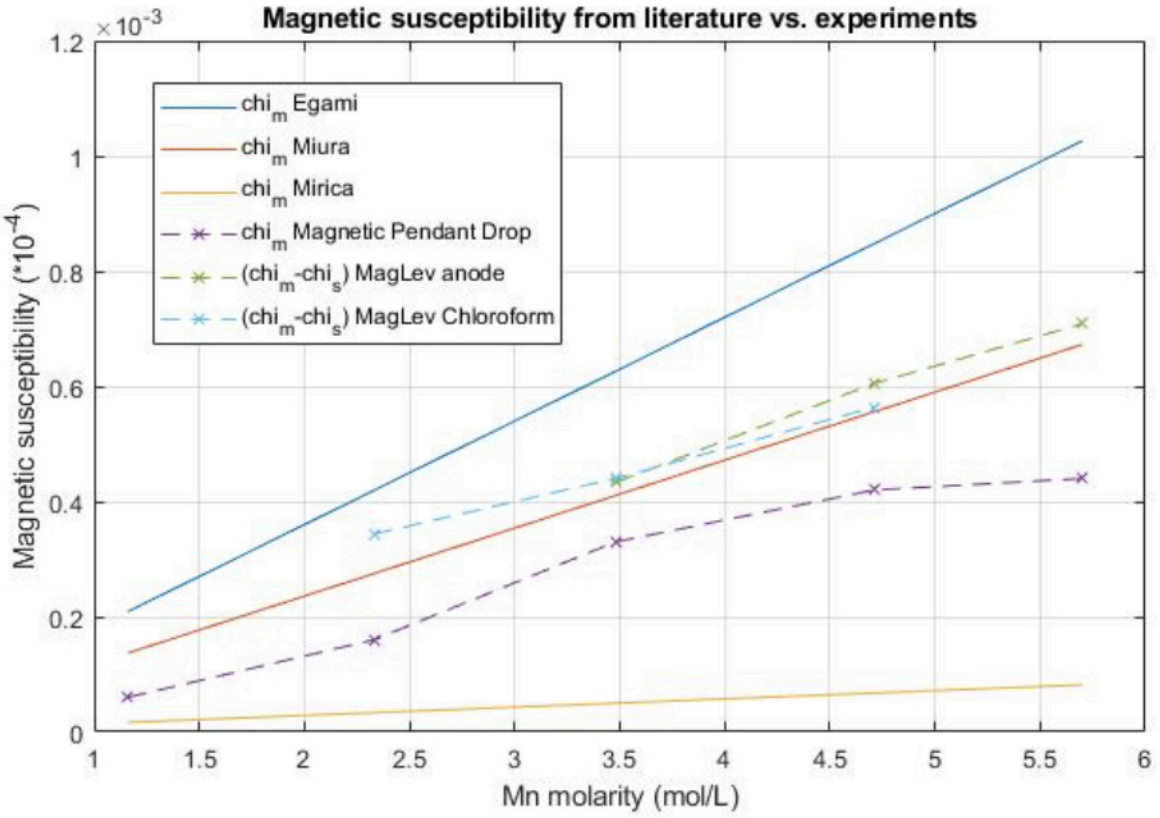

Figure 2.4: Magnetic susceptibility literature vs experiments [5]

The susceptibility values obtained from the pendant drop method were marginally lower than the values reported by Miura, while the susceptibilities determined by the levitation-based method were slightly higher. This discrepancy may be due to the small negative magnetic susceptibility of graphite, which was neglected in the magnetic pendant drop calculations. Table 2.2 presents the levitation height and corresponding susceptibility values for different $\mathrm{MnCl_2}$ concentrations. The value obtained for a saturated $\mathrm{MnCl_2}$ solution is used as an input for the particle tracking model.

Table 2.2: Estimated levitation heights and magnetic susceptibility values using graphite particles in a MDS setup.

% of saturation concentration	$\rho_p - \rho_m$ [kg/m^3]	h [mm]	$B_z \frac{dB_z}{dz}$ [T^2/m]	$\chi_p - \chi_s$ [-]
60	910	3	25.883	4.334×10^{-4}
80	791	5	16.117	6.050×10^{-4}
100	709	6	12.336	7.085×10^{-4}

The following sub question raised at the beginning of this chapter can now be addressed.

SQ1) How does the magnetic susceptibility of $\mathrm{MnCl_2}$ affect the levitation height of graphite particles in a paramagnetic medium?

The magnetic susceptibility of $\mathrm{MnCl_2}$ directly influences the levitation of graphite particles in MDS. A higher magnetic susceptibility of the medium increases the upward magnetic force acting on the particles, thereby enhancing their levitation potential. Levitation occurs only when the condition described in Equation 2.5 is satisfied. Calculations based on values reported by Miura and Egami show that levitation is theoretically possible for $\mathrm{MnCl_2}$ concentrations above 2.67 $\mathrm{mol/L}$ and 1.87 $\mathrm{mol/L}$, respectively. In contrast, Mirica's lower susceptibility values do not support levitation. Experimental measurements

from a previous study confirmed that the susceptibility values closely matched those reported by Miura. In summary, accurate determination of the magnetic susceptibility is crucial, as higher values significantly increase the feasibility of particle levitation.

2.2. A particle tracking model

Before introducing the particle tracking model, several simplifications are outlined. The $MnCl_2$ solution is assumed to be quiescent and homogenous, in the absence of background flow or turbulence. Particle interactions are neglected due to a low particle concentration, allowing the use of a one-way fluid particle coupling approach. Furthermore, particle motion is simulated in two-dimensions, and 1000 graphite particles, with representative density and average size, are used to model the suspension.

To simulate the magnetic field generated by the magnetic configuration, COMSOL Multiphysics 6.2 was used. This finite element simulation software divides the geometry into smaller finite elements (typically triangles or tetrahedra) and solves the governing equations over these elements, enabling accurate modelling of complex fields and boundary conditions. This magnetic field was generated by ten stacked neodymium magnets and is shown in Figure 2.5.

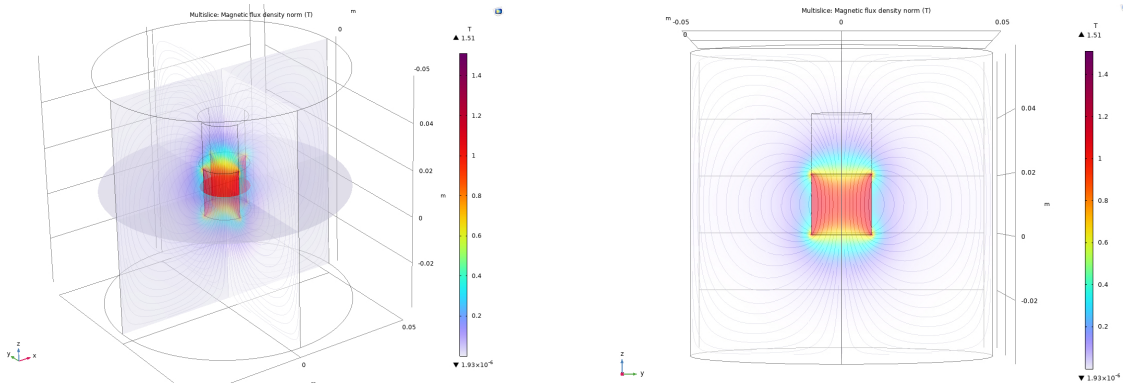

(a) 3D magnetic flux density distribution from stacked magnets

(b) Magnetic flux density in the YZ-plane

Figure 2.5: Magnetic field distribution generated in COMSOL.

In both sub figures, two cylinders are shown. The lower cylinder represents the disk magnet, with the equivalent height of ten stacked neodymium magnets, modelled using the BMN-52 material (representing the N52 properties). The upper cylinder corresponds to the vial region, containing the $MnCl_2$ solution and the dispersed graphite particles, where magnetic effects will be investigated.

To accurately model the magnetic field variations within the volume of interest, a very fine mesh size (in COMSOL) was used to enhance the resolution of the magnetic field gradients. To simplify the model, only forces and motion in the vertical (z) and horizontal (y) directions were considered. As shown in Figure 2.5b, the magnetic field in the YZ-plane is strongest just above the magnet and decreases with height. The magnetic field data forms the basis for calculating the magnetic forces and will be utilized to determine both the levitation height and lateral movement of the graphite particles. To assess the accuracy of the COMSOL-generated field B_z, its vertical gradient $\frac{\partial B_z}{\partial z}$ and their product $B_z \frac{\partial B_z}{\partial z}$ were plotted along the central axis of the disk magnet from z=0 to 30 mm. In Figure 2.6 these results are compared with analytical expressions, showing strong agreement in field strength, gradient and the magnetic force term.

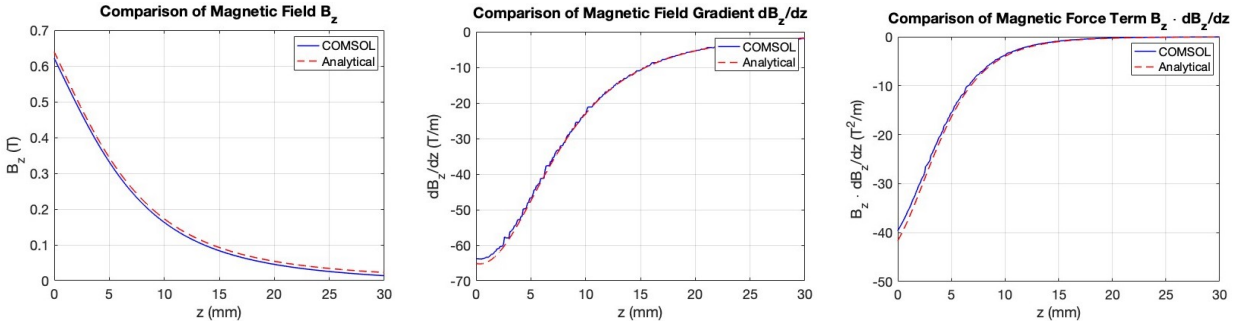

(a) Magnetic Field B_z **(b)** Magnetic Field Gradient $\frac{dB_z}{dz}$ **(c)** Magnetic Force Term $B_z \cdot \frac{dB_z}{dz}$

Figure 2.6: Comparison between COMSOL and analytical results for the magnetic field, its gradient, and their product.

The magnetic field used in the simulation was extracted from the two-dimensional YZ-plane in COMSOL. The extracted magnetic field data were defined on a regular grid with a spatial resolution of $\Delta y = \Delta z = 0.1\text{mm}$. Based on the experimental setup shown in Figure 2.7, the simulation domain was limited to:

$$z \in [0, 10]\text{mm}, \quad y \in [-7.5, 7.5]\text{mm} \tag{2.6}$$

Figure 2.7: Experimental setup [5]

The vertical range corresponds to the height over which levitation was observed (slightly higher) and the horizontal range matches the diameter of the vial (15mm), which is smaller than the stacked magnets. The resolution of 0.1 mm, approximately 18 times larger than the average graphite diameter (18 µm), was selected as a practical balance between computational efficiency and accuracy. Using a finer grid (0.01 mm) resulted in a significant increase in the computational time without a noticeable improvement in key outcomes, such as the levitation height.

To ensure accurate particle tracking, Δt was chosen such that the displacement of the particle $v \cdot \Delta t \approx d_p$. Given an average velocity of 2×10^{-6} m/s and a particle diameter of 18 µm, the estimated time step is approximately 9 s. However, a smaller time step of $\Delta t = 1$ s was used to ensure displacement remained well below the particle diameter.

To initialize the simulation, diameters for 1000 graphite particles were sampled from a normal distribution, based on particle size data [44]. According to this study, graphite particles in black mass material have an average size of μ =18 µm , ranging from 8 µm to 30 µm. Assuming a normal distribution, 99.7% of the values lie within $\pm 3\sigma$ of the mean. The standard deviation was estimated to be $\sigma \approx 3.67$ µm . Using this distribution μ =18 µm and $\sigma = 3.67$ µm), particles were grouped into three size categories:

- Small: $d < \mu - \sigma$

- Medium: $\mu - \sigma \leq d \leq \mu + \sigma$
- Large: $d > \mu + \sigma$

where d represents the particle diameter. This classification reflects a more realistic distribution in the black mass material while simplifying the model. A histogram of the particle size distribution, generated from the normal distribution, is shown in Figure 2.8.

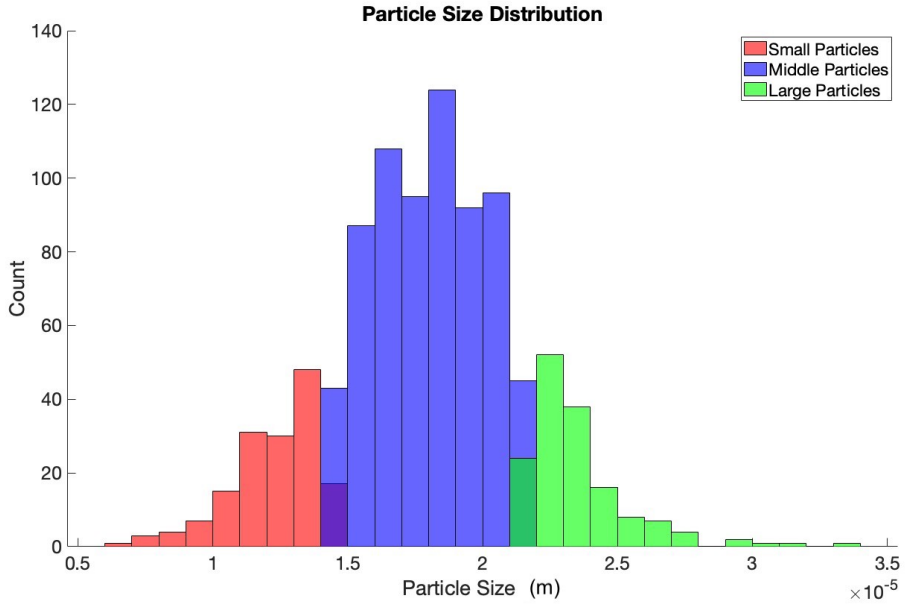

Figure 2.8: Histogram of particle diameters sampled from a normal distribution ($\mu = 18$ µm, $\sigma = 3.67$ µm).

This resulted in:

- 148 small particles (mean diameter: 1.25×10^{-5} m)
- 696 medium particles (mean diameter: 1.79×10^{-5} m)
- 156 large particles (mean diameter: 2.35×10^{-5} m).

To reduce computational complexity and improve the clarity of the results, all particles within a group were assigned the mean diameter of the group. This reduced the 1000 sampled particles to three distinct particle sizes, which could be distinguished by colour: red (small), blue (medium) and green (large). This simplification enabled more efficient simulation and comparison of the results without influencing the accuracy of the model significantly. The total particle volume was approximately $3.30 \times 10^{-12}\,\mathrm{m}^3$, while the volume of the vial was $1.767 \times 10^{-6}\,\mathrm{m}^3$. This corresponds to a particle volume fraction of approximately 1.87×10^{-6}, which is well below the 10^{-5} threshold.

All 1000 particles were assigned random initial positions within the defined 2D simulation domain, as shown in Figure 2.9. This random distribution ensures that particle motion and separation results from magnetic forces rather than initial placement, which allows comparison of the effect of particle size.

Following the initialization, the motion of each particle is governed by a balance of gravitational, buoyancy, magnetic and drag forces, as described in subsection 1.2.1. The net force balance on a spherical particle is:

$$m_\mathrm{p}\frac{dv_\mathrm{p}}{dt} = -3\pi\mu v_\mathrm{p} d + \frac{\chi_\mathrm{p} - \chi_\mathrm{m}}{\mu_0}(\vec{B}\cdot\nabla)\vec{B}\,V + (\rho_\mathrm{m} - \rho_\mathrm{p})Vg \tag{2.7}$$

Due to the small mass of graphite particles (4.8 ng [44]), inertial effects are negligible and particles are

assumed to reach their terminal velocity instantaneously. The operator $(\vec{B} \cdot \nabla)\vec{B}$ can be expanded as:

$$(\vec{B} \cdot \nabla)\vec{B} = \begin{pmatrix} B_x \frac{\partial B_x}{\partial x} + B_y \frac{\partial B_x}{\partial y} + B_z \frac{\partial B_x}{\partial z} \\ B_x \frac{\partial B_y}{\partial x} + B_y \frac{\partial B_y}{\partial y} + B_z \frac{\partial B_y}{\partial z} \\ B_x \frac{\partial B_z}{\partial x} + B_y \frac{\partial B_z}{\partial y} + B_z \frac{\partial B_z}{\partial z} \end{pmatrix} \tag{2.8}$$

When considering only the magnetic field components in the y- and z-direction, this results in the following steady-state force balances in y- and z-directions:

$$0 = -3\pi\mu v_{\mathrm{py}} d + \frac{\chi_{\mathrm{p}} - \chi_{\mathrm{m}}}{\mu_0} \left(B_y \frac{\partial B_y}{\partial y} + B_z \frac{\partial B_y}{\partial z} \right) \cdot \frac{1}{6}\pi d^3 \tag{2.9}$$

$$0 = -3\pi\mu v_{\mathrm{pz}} d + \frac{\chi_{\mathrm{p}} - \chi_{\mathrm{m}}}{\mu_0} \left(B_z \frac{\partial B_z}{\partial z} + B_y \frac{\partial B_z}{\partial y} \right) \cdot \frac{1}{6}\pi d^3 + (\rho_{\mathrm{m}} - \rho_{\mathrm{p}}) \cdot \frac{1}{6}\pi d^3 g \tag{2.10}$$

Solving for velocity components in y- and z-directions gives:

$$v_{\mathrm{py}} = \frac{\chi_{\mathrm{p}} - \chi_{\mathrm{m}}}{\mu_0} \cdot \frac{\left(B_y \frac{\partial B_y}{\partial y} + B_z \frac{\partial B_y}{\partial z} \right) \cdot \frac{1}{6}\pi d^2}{3\pi\mu} \tag{2.11}$$

$$v_{\mathrm{pz}} = \frac{\left[\frac{\chi_{\mathrm{p}} - \chi_{\mathrm{m}}}{\mu_0} \left(B_z \frac{\partial B_z}{\partial z} + B_y \frac{\partial B_z}{\partial y} \right) + (\rho_{\mathrm{m}} - \rho_{\mathrm{p}}) g \right] \cdot \frac{1}{6}\pi d^2}{3\pi\mu} \tag{2.12}$$

The velocities depend on particle size, magnetic susceptibility and spatial gradients in the magnetic field. Particle positions are updated over time using the explicit Euler method:

$$y_{\mathrm{p}}(t) = y_{\mathrm{p}}(t - \Delta t) + v_{\mathrm{py}} \cdot \Delta t \tag{2.13}$$

$$z_{\mathrm{p}}(t) = z_{\mathrm{p}}(t - \Delta t) + v_{\mathrm{pz}} \cdot \Delta t \tag{2.14}$$

Since the velocities v_{py} and v_{pz} are functions of the magnetic field and the particle's position typically does not coincide with the grid points, bilinear interpolation is required to estimate magnetic field values and their spatial derivatives at off-grid particle positions. This step is crucial as the magnetic force (and thus velocity) is fully determined by the local magnetic field. The updated velocities are then used to compute new positions and this process is repeated for every particle at every time step. This results in a time-resolved model which describes how the particles move, levitate and separate under the influence of the magnetic field.

The initial configuration of the simulation is shown in Figure 2.9, in which 1000 particles, composed of small, medium and large sizes, are randomly distributed across 2D y-z domain. Each particle moves from its initial position according to the size-dependent velocity component, which is governed by the local magnetic field gradient. To visualize particle dynamics, a MATLAB script was developed to record particle positions every 30 seconds using an interactive time slider. This allows for real-time observation of the trajectory of the particles. While the interactive slider cannot be embedded in this report, key results are presented and discussed below to illustrate the evolution of the particle trajectories.

- As the time progresses, particles which start above their equilibrium height will move downward towards the equilibrium position, while particles below their equilibrium height will move upward.
- After some time (about 300 seconds), the particles begin to concentrate around a levitation height between 5-7 mm, shown in Figure 2.10.
- After 1200 seconds particles have further aligned with most particles positioned between 5-6 mm. Notably, small particles tend to lag slightly behind the medium and large particles as is shown in Figure 2.11.
- After 3000 seconds the system reaches a near steady state. An interesting pattern emerges where particles accumulate near the edges, shown in Figure 2.12, a phenomenon that will be discussed in more detail later in this chapter.

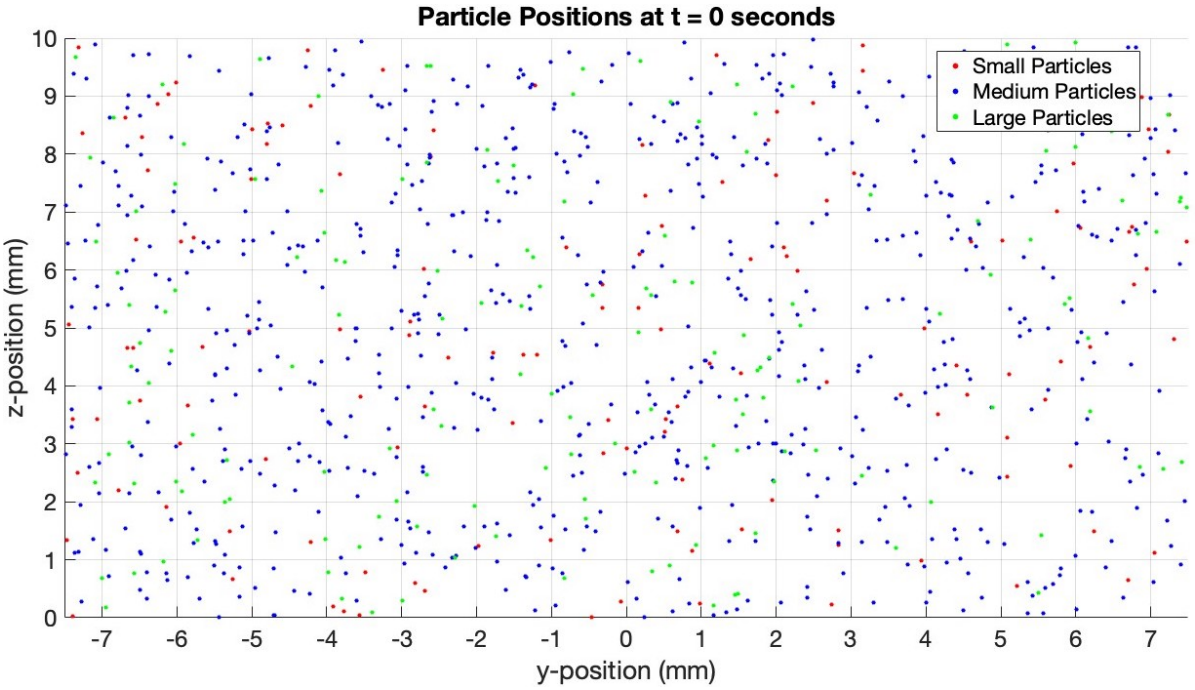

Figure 2.9: The evolution of the position of the particles at t=0 s

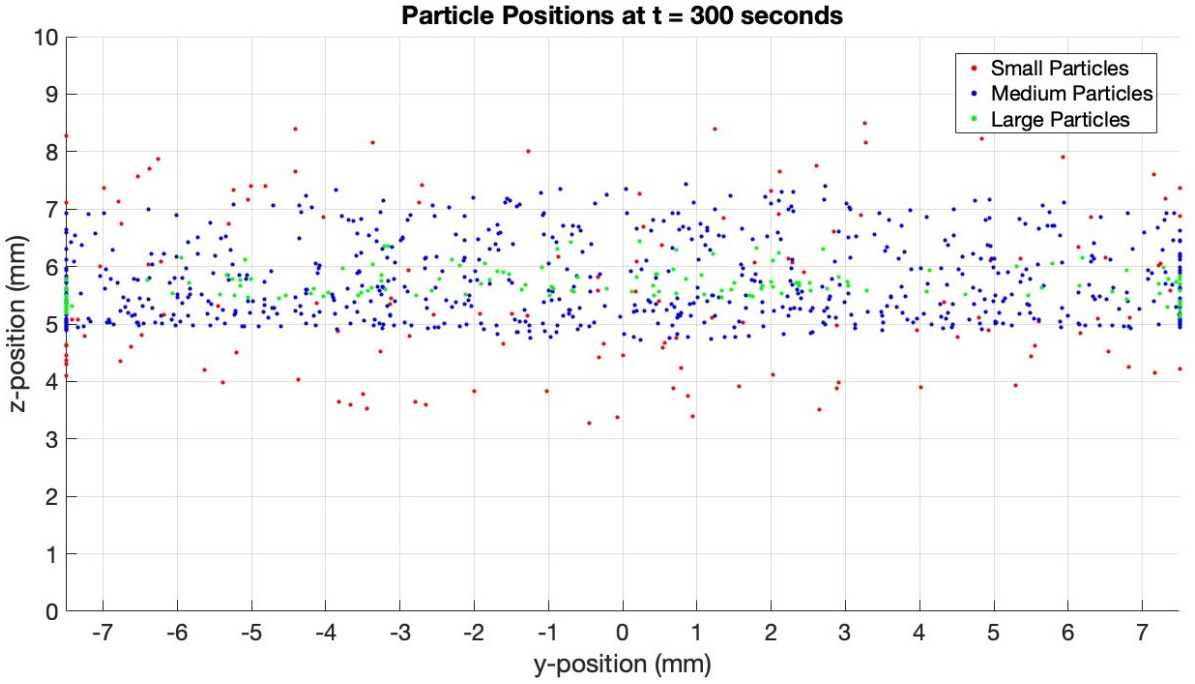

Figure 2.10: The evolution of the position of the particles at t=300 s

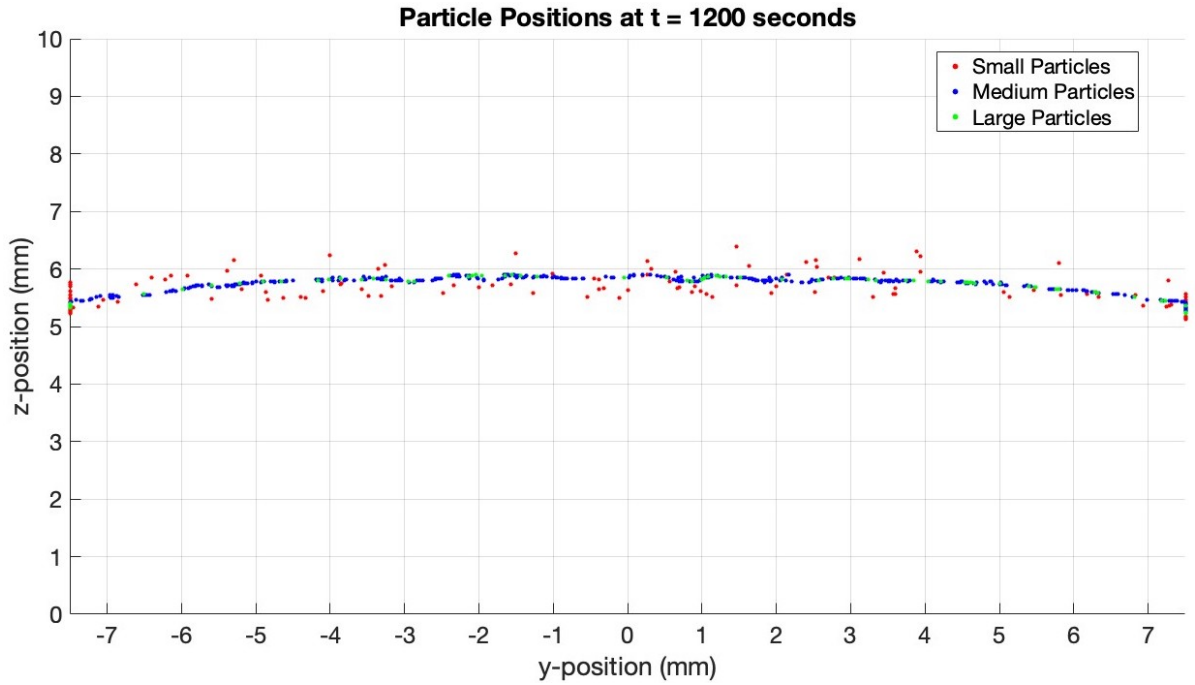

Figure 2.11: The evolution of the position of the particles at t=1200 s

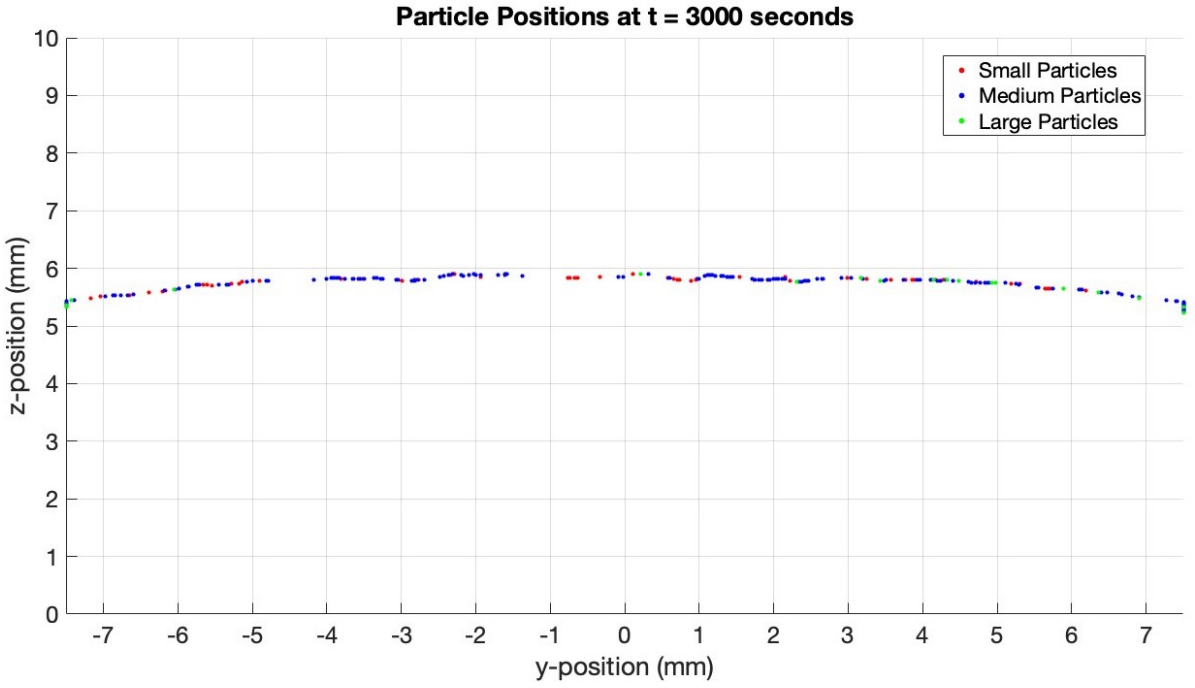

Figure 2.12: The evolution of the position of the particles at t=3000 s

Direct comparison between experimental and simulation results is challenging, since the model assumes a dilute suspension in which hydrodynamic interactions are neglected. In the experiment a much higher concentration of particles is involved which implies that the local volume fraction is higher than 10^{-5}. As a result particle-particle interaction and particle clustering becomes relevant, phenomena which are not captured in the current model. However, the main goal of the simulation is not to replicate every experimental detail, but rather to highlight the underlying physical trends observed during the experiments.

When a 100% saturation concentration of $\mathrm{MnCl_2}$ was used in the experiments, graphite particles reached a stable levitation height between 5 and 6 mm [5]. The simulation reproduced this behaviour as the particles did converge to a levitation height between 5-6 mm, independent of their size.

Some interesting observations from the experiments were that the graphite particles did tend to move laterally and accumulate at the boundaries of the container as shown in Figure 2.10-Figure 2.12. In the beginning, the cause of this behaviour was not well understood, but running the simulations it became clear. Initially, only dominant magnetic field contributions $\mathrm{B_z}\frac{\partial \mathrm{Bz}}{\partial \mathrm{z}}$ and $\mathrm{B_y}\frac{\partial \mathrm{By}}{\partial \mathrm{y}}$ terms from the magnetic force $(\vec{B}\cdot\nabla)\vec{B}$ expression were considered. Under this assumption, particles migrate toward the centre, resulting in a more curved distribution, as shown in Figure 2.13.

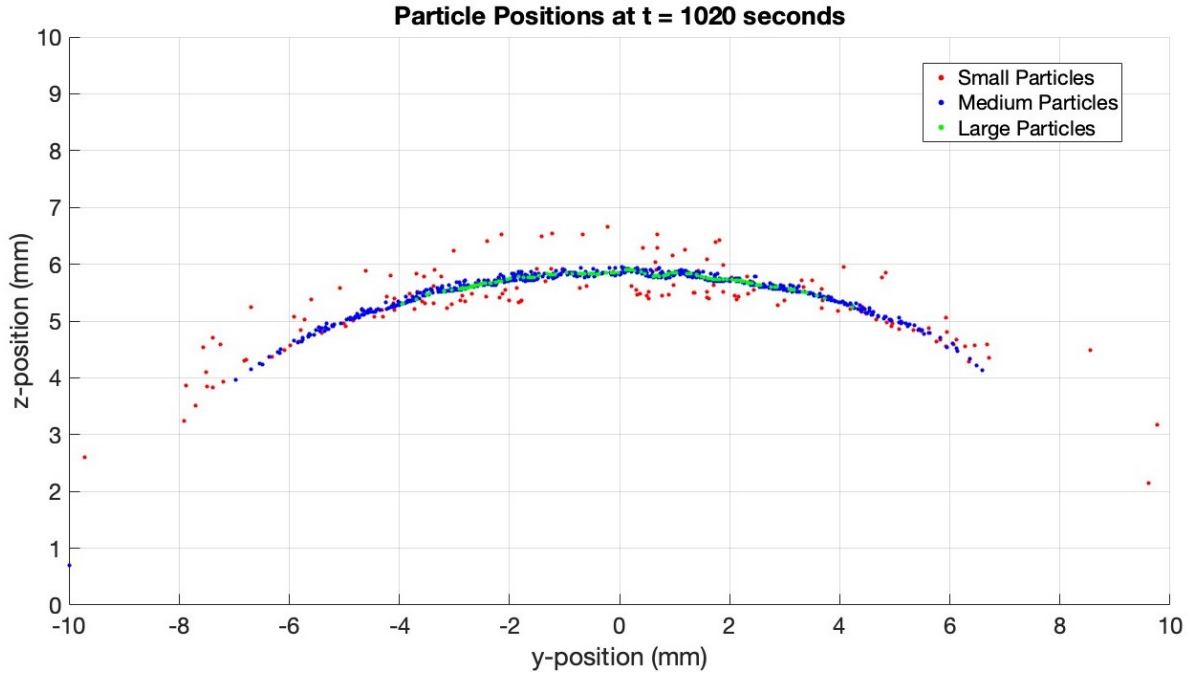

Figure 2.13: Particle position for simplified field neglecting cross-gradient terms.

However, neglecting cross-gradient terms such as $B_z\frac{\partial By}{\partial z}$ and $B_y\frac{\partial Bz}{\partial y}$ led to an underestimation of the lateral forces. Including these components resulted in a significant improvement of the spatial positioning of the particles and a better alignment with the experimental results. These results suggest that the lateral movement and accumulation of the particles near the sides of the container are primarily driven by the magnetic field, specifically through the influence of cross-gradient components. Nonetheless, other factors such as boundary effects, hydrodynamic interactions or the hydrophobic nature of graphite, might also contribute to lateral displacement but were not investigated in this model. The agreement between simulation and experiment confirms that the simplified force balance accurately predicts the levitation height.

Simulation results reveal that smaller (red) particles require more time to reach their equilibrium height compared to medium and large particles. As shown in Figure 2.10 and Figure 2.11, larger particles accumulate faster near the levitation height, while smaller particles remain more dispersed. This behaviour can be explained using the velocity expressions described in Equation 2.11 and Equation 2.12, where both components scale with the square of the particle diameter (d^2). Consequently larger particles experience stronger magnetic and gravitational forces, resulting in higher velocities and faster convergence to the equilibrium. This trend is confirmed by the computed average velocities: 1.9127×10^{-6}, 3.8884×10^{-6} and 6.9870×10^{-6} m/s for small, medium and large particles, respectively. At equilibrium, the net force acting on the particle becomes zero, resulting in a steady-state condition with negligible

velocity.

$$\frac{\chi_p - \chi_m}{\mu_0}(B \cdot \nabla)B\frac{1}{6}\pi d^3 = -(\rho_m - \rho_p)\frac{1}{6}\pi d^3 g \tag{2.15}$$

The d^3 term cancels out, confirming that the equilibrium height is independent of particle size. However, the time required to reach the equilibrium position is strongly size-dependent. Smaller particles experience smaller net forces and travel more slowly and thus take longer to settle.

To estimate settling time, initially a velocity-based equilibrium criterion was applied, where particles were assumed to have reached equilibrium, when their vertical velocity fell below a defined threshold. Simulations were conducted for particle sizes ranging from 5 µm to 50 µm (in 2.5 µm increments) using a time step of $\Delta t = 0.1$s and for each simulation run 100 particles were randomly distributed over the domain. The number of iterations required to reach the velocity threshold was recorded for velocity thresholds of $v_{pz} \leq 10^{-7}$ m/s and $v_{pz} \leq 10^{-8}$ m/s, confirming that the settling time decreases with increasing particle sizes (shown in appendix B.2).

Since the equilibrium position in the experiments was judged visually, the velocity-based stopping criterion in the simulations was found to be too strict. The model predicts that all particles converge to the same equilibrium position. However, in reality particles do not converge to the same position and as particles accumulate near the levitation region, the local volume fraction increases, violating the dilute suspension assumption. This reduces the accuracy of the predicted velocities and alters the particle trajectories, since hydrodynamic interactions become significant and should be taken into account. These effects justify the use of a more practical, position-based equilibrium criterion. Particles are assumed to have reached their equilibrium position when their vertical positions fall between 5-7 mm. The results are shown in Figure 2.14.

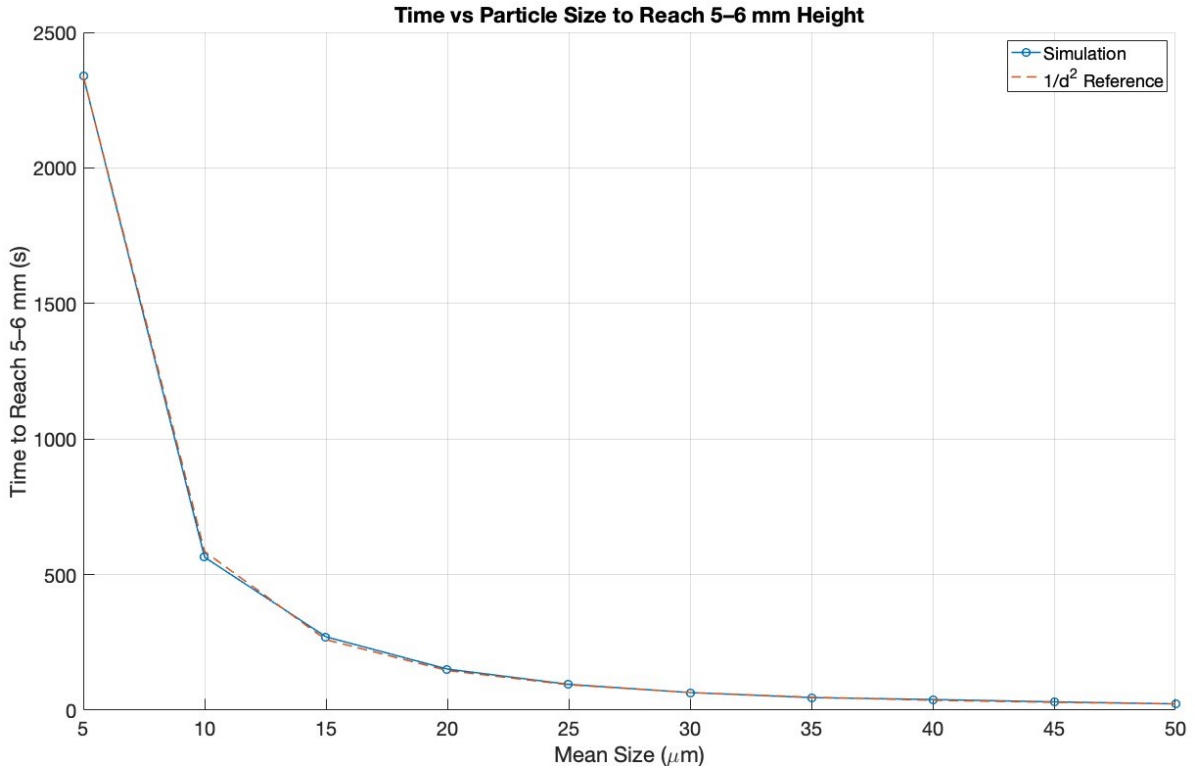

Figure 2.14: Average iterations before particles have reached a levitation height between 5-7 mm

The figure illustrates that settling time scales with $1/d^2$, with smaller particles taking significantly longer to reach equilibrium. Experiments showed that particles reached their equilibrium position within 1-2 minutes. The model predicts that particles with an average size of 20 µm (the reported average size for graphite in black mass material [44]) reach the 5-7 mm range in about 140 s, which aligns well with

experimental observations. Furthermore, some particles were observed to lag behind. This supports the hypothesis that there is a broad variation in particle size, with smaller particles settling more slowly than larger ones.

While the exact settling time may be less important for the separation of relatively uniform anodic graphite particles, it becomes more important in the context of black mass materials. These contain a broad distribution of particle sizes and densities. In such cases, understanding both levitation and settling dynamics is essential to evaluate the feasibility and efficiency of MDS. If settling is too slow or if equilibrium heights between different materials are narrowly spaced, the separation process may become impractical at industrial scale.

The following sub questions raised at the beginning of this chapter can now be addressed.

SQ2) How does the particle size affect the levitation height and settling time of graphite particles in a paramagnetic medium?

From the simulation results, it is observed that the final levitation height is independent of particle size, as all force terms scaling with d^3 cancel out at equilibrium. Consequently, all particles converge to the same levitation band (5-6mm). However, the size of the particles strongly affects the time required to reach this equilibrium height. This is because the velocity expressions derived from the force balance scale with the square of the particle diameter. As a result, larger particles experience a stronger net force and move faster toward their equilibrium position. In contrast, smaller particles experience weaker net forces and take longer to settle. This behaviour was especially observed in the early stages of the simulation, where smaller particles lagged behind larger ones. Experimental results corroborated this finding, showing a distinct accumulation of particles around the levitation height, with a portion of particles remaining dispersed throughout the fluid. This dispersion is likely due to differences in particle sizes within the suspension. This highlights the importance of considering particle size distributions when designing industrial-scale MDS systems, particularly for black mass, which contains a heterogeneous mixture of particles. The introduced position-based equilibrium criterion further validated this effect, showing that the average time to reach equilibrium scaled inversely with the square of the particle size.

SQ3) To what extent does the simulation reproduce experimental trends in vertical graphite clustering and lateral distribution?

The simulation successfully reproduced the experimentally observed vertical clustering and lateral distribution of graphite particles. In both the experiment and the simulation, the graphite particles gradually converged to a levitation height between 5-6 mm. Additionally, the simulation captured the lateral movement and accumulation of the particles near the container walls. Initially only the dominant magnetic force components $B_z \frac{\partial Bz}{\partial z}$ and $B_y \frac{\partial By}{\partial y}$ were considered. However, this simplification led to inaccurate lateral positioning and levitation heights, with particles converging toward the centre of the container. Including the cross gradient terms such as $B_z \frac{\partial By}{\partial z}$ and $B_y \frac{\partial Bz}{\partial y}$, improved the spatial accuracy of the simulation significantly. The resulting sideward drift in the simulation matched the experimental observations. This underscores the importance of including these components to accurately model particle trajectories.

3

Analysis of a shrinking core model

This chapter presents a two-part analysis of the leaching behaviour of lithium cobalt oxide ($LiCoO_2$) using shrinking core models. First, building on the general framework of the SCM and its dimensionless form (introduced in subsection 1.2.2 and subsection 1.2.3), the model is adapted to simulate $LiCoO_2$ leaching in sulfuric acid (H_2SO_4). Key process parameters are introduced, and a sensitivity analysis is performed to identify which parameters have the largest impact on the leaching time. Simulation results are then compared to experimental data to assess model performance. In the second part, a previously developed SCM describing the leaching of $LiCoO_2$ with hydrochloric acid (HCl) and hydrogen peroxide (H_2O_2) is reconstructed. This model incorporates the formation of a Co_3O_4 crust around the shrinking core and accounts for the role of H_2O_2 as a reducing agent. This model is then applied to sulfuric acid leaching to evaluate its applicability under different chemical conditions. Finally, the two models are compared to experimental data.

In this chapter the following sub questions will be addressed

SQ4) Which parameters affect the leaching time and efficiency of $LiCoO_2$ particles most according to the dimensionless shrinking core model?

SQ5) How does the shrinking core model with varying crust improve the representation of diffusion and reaction processes compared to the dimensionless model?

SQ6) To what extent does the shrinking core model with a varying crust replicate experimental leaching trends for $LiCoO_2$ in sulfuric acid, such as lithium and cobalt recovery under varying operational conditions?

3.1. Dimensionless shrinking core model

The SCM introduced in subsection 1.2.2 is applied to the leaching of $LiCoO_2$ particles, a commonly used cathode material in LIBs. Li and Co can be recovered through a hydrometallurgical leaching process, using H_2SO_4 as a leaching agent and H_2O_2 as a reducing agent. Co in $LiCoO_2$ exists predominantly in its 3+ oxidation state, which is not soluble in sulfuric acid. Adding H_2O_2 is crucial, as it reduces Co^{3+} to more soluble Co^{2+} which enhances the dissolution of Co, thereby improving leaching efficiency. The leaching reaction proceeds in two steps.

1. **Primary leaching step:** $LiCoO_2$ reacts with H_2SO_4 and H_2O_2 to form lithium sulfate (Li_2SO_4), cobalt sulfate ($CoSO_4$), solid cobalt oxide (Co_3O_4), along with water (H_2O) and oxygen (O_2):

$$4LiCoO_{2(s)} + 3H_2SO_{4(aq)} + H_2O_{2(aq)} \rightarrow Co_3O_{4(s)} + 2Li_2SO_{4(aq)} + CoSO_{4(aq)} + 4H_2O_{(aq)} + O_{2(g)} \tag{3.1}$$

2. **Secondary leaching step:** The solid $\mathrm{Co_3O_4}$ further dissolves in the presence of additional $\mathrm{H_2SO_4}$ and $\mathrm{H_2O_2}$:

$$\mathrm{Co_3O_{4(s)} + 3H_2SO_{4(aq)} + H_2O_{2(aq)} \rightarrow\ 3CoSO_{4(aq)} + 4H_2O_{(aq)} + O_{2(g)}} \tag{3.2}$$

Combining Equation 3.1 and Equation 3.2 yields the overall global leaching reaction [45]:

$$\mathrm{4LiCoO_{2(s)} + 6H_2SO_{4(aq)} + 2H_2O_{2(aq)} \rightarrow\ 4CoSO_{4(aq)} + 2Li_2SO_{4(aq)} + 8H_2O_{(aq)} + 2O_{2(g)}} \tag{3.3}$$

In the context of the SCM, $\mathrm{LiCoO_2}$ serves as the solid reactant (the shrinking core) and sulfuric acid is treated as the liquid reactant which diffuses through the product layer towards the unreacted core. By normalizing Equation 3.4, the following is obtained:

$$\mathrm{\frac{2}{3}LiCoO_2}(s) + \mathrm{H_2SO_4} + \frac{1}{3}\mathrm{H_2O_2} \rightarrow\ \frac{2}{3}\mathrm{CoSO_4}(aq) + \frac{1}{3}\mathrm{Li_2SO_4}(aq) + \frac{4}{3}\mathrm{H_2O} + \frac{1}{3}\mathrm{O_2} \tag{3.4}$$

This normalized reaction indicates that for each mole of liquid reactant consumed, 2/3 moles of solid reactant are consumed. Consequently, the stoichiometric coefficient b is $\frac{2}{3}$.

The general equations for the SCM, described in subsection 1.2.2, can be tailored for the leaching of $\mathrm{LiCoO_2}$ using sulfuric acid and hydrogen peroxide described in Equation 3.4. These equations describe the concentration of sulfuric acid at the core, the shrinking radius of the unreacted $\mathrm{LiCoO_2}$ core and the change of the bulk sulfuric acid concentration over time. The concentration of the sulfuric acid at the core surface is expressed as:

$$C_{\mathrm{H_2SO_4,core}} = \frac{C_{\mathrm{H_2SO_4,bulk}}}{1 + \left(\frac{r_c}{r_s}\right)^2 \left(\frac{k}{k_m}\right) + \left(\frac{k r_c}{D_e}\right)\left(1 - \frac{r_c}{r_s}\right)} \tag{3.5}$$

The rate of change of the unreacted core radius is described by:

$$\frac{dr_{\mathrm{c}}}{dt} = -\frac{\frac{2}{3}M_{\mathrm{LiCoO_2}}}{\rho_{\mathrm{LiCoO_2}}} \frac{C_{\mathrm{H_2SO_4,bulk}}}{\frac{1}{k} + \left(\frac{r_{\mathrm{c}}}{r_{\mathrm{s}}}\right)^2 \frac{1}{k_{\mathrm{m}}} + \frac{r_{\mathrm{c}}}{D_{\mathrm{e}}}\left(1 - \frac{r_{\mathrm{c}}}{r_{\mathrm{s}}}\right)} \tag{3.6}$$

The decrease in the bulk concentration of sulfuric acid over time is described by:

$$\frac{dC_{\mathrm{H_2SO_4,bulk}}}{dt} = -\frac{3M_{\mathrm{LiCoO_2}}\, k}{\rho_{\mathrm{LiCoO_2}}\, r_{\mathrm{s}}} \left(\frac{r_{\mathrm{c}}}{r_{\mathrm{s}}}\right)^2 C_{\mathrm{LiCoO_2},0}\, C^{\mathrm{n}}_{\mathrm{H_2SO_4,core}} \tag{3.7}$$

The SCM can be formulated in a dimensionless form to generalize its application, as introduced in subsection 1.2.3. To adapt it to the specific case of leaching using $\mathrm{H_2SO_4}$ and $\mathrm{H_2O_2}$, the dimensionless shrinking radius r^*_{c} as a function of the dimensionless time τ is given by:

$$\frac{dr^*_c}{d\tau} = -\left(\frac{\frac{2}{3}M_{\mathrm{LiCoO_2}}}{\rho_{\mathrm{LiCoO_2}}}\right) \frac{C_{\mathrm{H_2SO_4,bulk},0} - \frac{3}{2}C_{\mathrm{LiCoO_2},0}(1 - r^{*3}_{\mathrm{c}})}{\frac{1}{\mathrm{Da}} + (r^*_{\mathrm{c}})^2\left(\frac{1}{\mathrm{Sh}}\right) + \frac{1}{\epsilon^{3/2}}\, r^*_{\mathrm{c}}(1 - r^*_{\mathrm{c}})} \tag{3.8}$$

The shrinking of the dimensionless core radius r^*_{c} involves the dimensionless Da and Sh numbers and several other physical and chemical parameters. The baseline values for these parameters, listed in Table 3.1, serve as a reference case for analysing how variations influence the total dissolution time of $\mathrm{LiCoO_2}$ particle radius of $\mathrm{LiCoO_2}$.

Table 3.1: Overview of variables influencing the SCM applied to $LiCoO_2$ leaching, including baseline values.

Symbol	Description	Baseline Value	Units
$M_{\mathrm{LiCoO_2}}$	Molecular weight of $LiCoO_2$	0.09787	[kg/mol]
$\rho_{\mathrm{LiCoO_2}}$	Density of $LiCoO_2$ particles	4800	[kg/m^3]
Pulp density	Mass of solid per volume of solution	50	[kg/m^3]
$C_{\mathrm{LiCoO_2},0}$	Initial solid reactant concentration	510.88	[mol/m^3]
$C_{\mathrm{H_2SO_4,bulk},0}$	Initial sulfuric acid concentration in bulk	2500	[mol/m^3]
ε	Porosity of product layer	1	[–]
$k(T)$	Rate constant	2.17×10^{-8}	[m/s]
$D_{\mathrm{m}}(T, C_{\mathrm{H_2SO_4}})$	Molecular diffusion coefficient	2.401×10^{-9}	[m^2/s]
r_{s}	Initial particle radius	5×10^{-6}	[m]
T	Temperature	25	[°C]
$Da = \frac{kr_s}{D_m}$	Damköhler number	4.506×10^{-5}	[–]
$Sh = \frac{k_m r_s}{D_m}$	Sherwood number	2	[–]

Pulp density refers to the mass of solid reactant suspended in a given volume. The initial concentration of the solid reactant $C_{\mathrm{LiCo_2},0}$ depends on the pulp density and can be calculated with

$$C_{\mathrm{LiCo_2},0} = \frac{\text{Pulp Density}}{M_{\mathrm{LiCoO_2}}} = \frac{50}{0.09787}\frac{\mathrm{kg/m^3}}{\mathrm{kg/mol}} = 510.88\,\frac{\mathrm{mol}}{\mathrm{m^3}} \tag{3.9}$$

In Figure 3.1 it is shown how the dimensionless core radius shrinks over time for this baseline scenario.

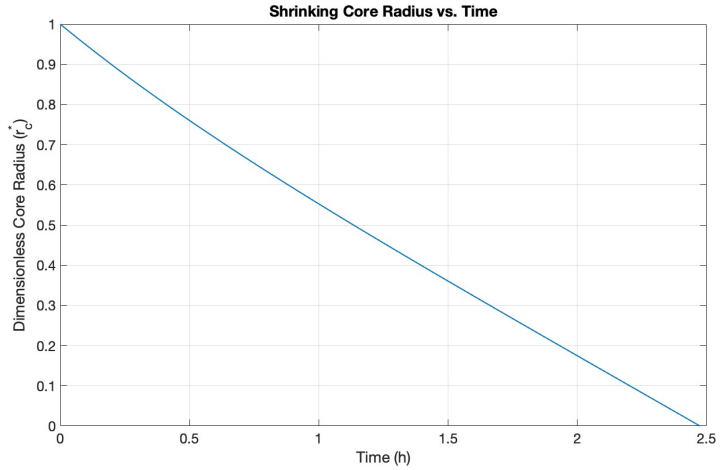

Figure 3.1: Dimensionless radius r_c^* as a function of time for the baseline situation.

The core radius completely shrinks after approximately 2.47 hours, which indicates complete dissolution of the solid particle. The linear profile of the shrinking core radius is characteristic of a process controlled by chemical reaction kinetics [32]. Building on this baseline, a series of sensitivity analyses were performed by systematically varying one parameter while keeping the other parameters fixed at their baseline values to evaluate the effect of each parameter on the dissolution time. The following parameters were investigated: the bulk sulfuric acid concentration, the pulp density, the Sh number, the porosity of the product layer, the particle radius and the temperature. The Sh number and the porosity were found to have a minor effect on the dissolution time and are not discussed further.

Effect of sulfuric acid concentration

In Figure 3.2, the effect of the sulfuric acid concentration on the dissolution time is shown. The figure shows that increasing the sulfuric acid concentration leads to a significantly shorter dissolution time, especially at lower concentrations. In the figure (and in subsequent figures), the dissolution time for the baseline scenario is indicated by a red marker.

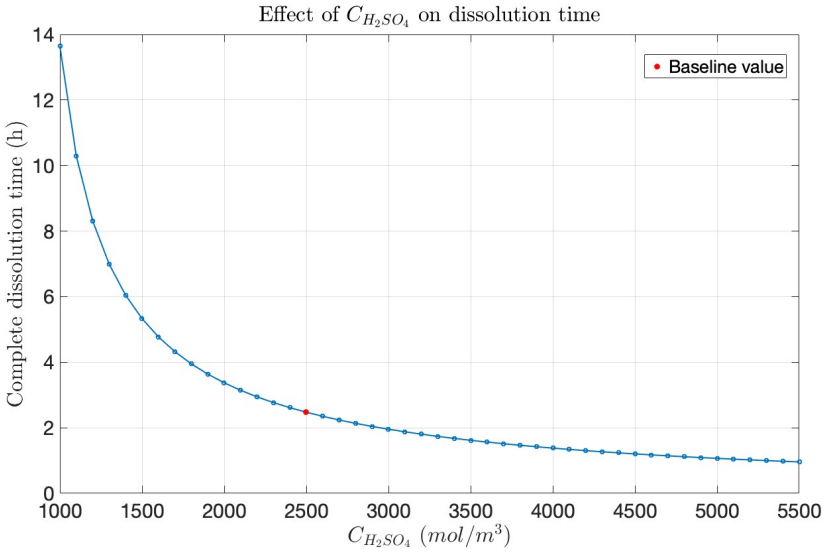

Figure 3.2: Time for complete dissolution of the radius as a function of $C_{\mathrm{H_2SO_4}}$

Increasing $\mathrm{C_{H_2SO_4}}$ from 1000 to 2500 $\mathrm{mol/m^3}$ results in a substantial decrease of the dissolution time. However, further increases beyond 3500-4000 $\mathrm{mol/m^3}$ yield marginal improvements. This highlights an important trade-off in hydrometallurgical leaching, where higher acid concentrations accelerate the leaching but also increase the chemical usage and costs. An optimal concentration must balance efficiency with economic and environmental considerations. At sulfuric acid concentrations below 700 $\mathrm{mol/m^3}$, the model predicts incomplete particle dissolution. The dissolution process is extremely slow and the shrinking of the core effectively stagnates.

Effect of pulp density

In Figure 3.3, the effect of the pulp density on the dissolution time is shown, indicates a longer dissolution time for higher pulp densities.

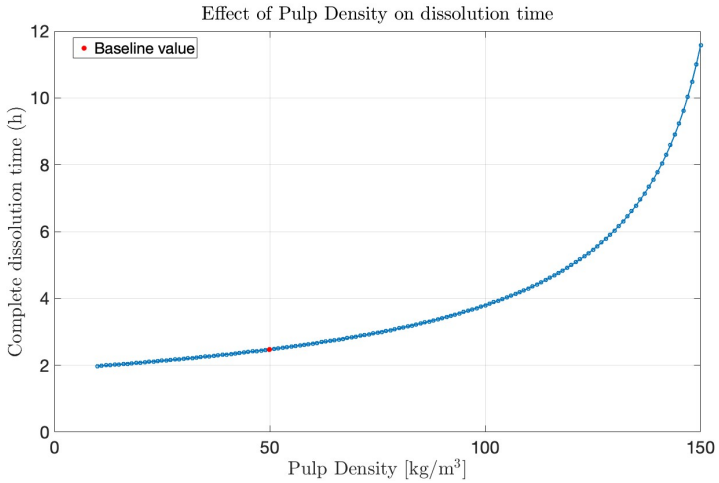

Figure 3.3: Time for complete dissolution of the radius as a function of the pulp density

Increasing the pulp density from 10 to 100 $\mathrm{kg/m^3}$ doubles the dissolution time from 2 to 4 hours. However, beyond 100 $\mathrm{kg/m^3}$ the dissolution time increases significantly. This trend can be attributed to the reduced available surface area per unit volume solution for higher pulp densities, which limits the acid access to particle surfaces and slows the dissolution process [7]. For pulp densities above 150 $\mathrm{kg/m^3}$, complete dissolution is no longer possible and the shrinking of the core stagnates.

Effect of particle radius

The particle radius has a substantial effect on the total dissolution time of $\mathrm{LiCoO_2}$ particles. As shown in Figure 3.4, a non-linear relationship is observed: increasing the particle radius from 5 µm to 10 µm increases the dissolution time from 2.67 hours to 10.67 hours.

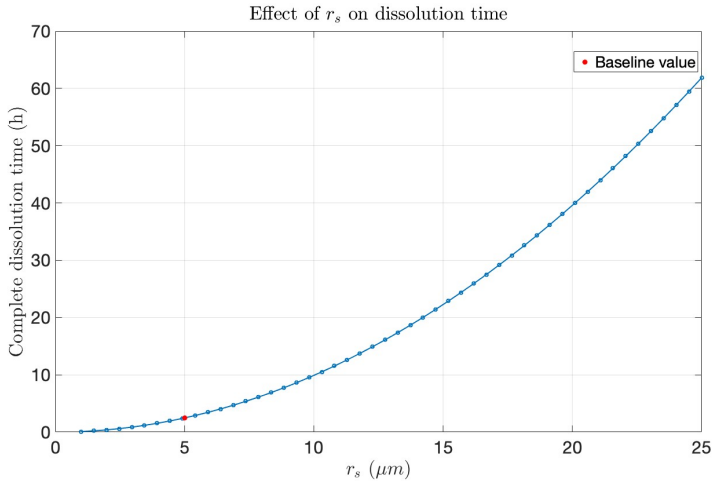

Figure 3.4: Time for complete dissolution of the radius as a function of r_s

This increase is primarily due to two factors: smaller particles have a higher surface area-to-volume ratio, enabling faster acid access and reaction, whereas the acid must diffuse deeper for large particles which slows down the leaching process.

Effect of Temperature

In Figure 3.5, the effect of the temperature on the dissolution time is shown.

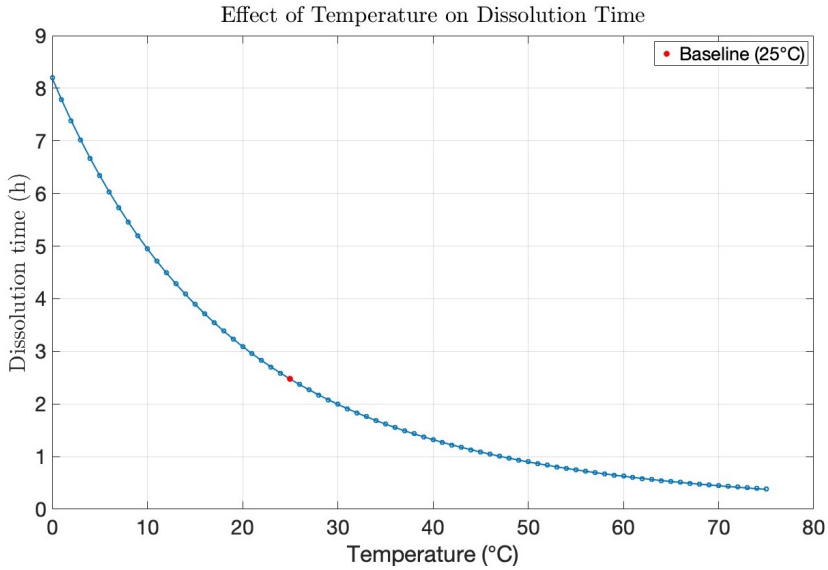

Figure 3.5: Time for complete dissolution of the radius as a function of T

The Da number depends on the rate constant and the diffusion coefficient which are both strongly temperature dependent and follow Arrhenius-type behaviour. A more detailed explanation for this can be found in Appendix C. Since both k and D_{m} increase exponentially with temperature, analysing temperature effects provide therefore a practical way to understand the effect of the Da number on the dissolution time. Increasing the temperature significantly reduces the dissolution time due to faster reaction kinetics. Above 50 °C, the dissolution time drops below one hour, with a further decrease up to 75 °C, in agreement with experimental data [7].

While it may seem beneficial to increase the temperature beyond $75°\mathrm{C}$, the improvements in leaching efficiency have been reported in literature to be marginal [7][46]. The simulation results also show little improvement. For example, increasing the temperature from 25 to 75 $°\mathrm{C}$ reduces the leaching time from 148 minutes to 22.2 minutes, whereas a further increase to $90°\mathrm{C}$ only reduces it to 14.2 minutes. This diminishing return suggest a practical upper limit, offering a balance between leaching efficiency and the additional energy input required for heating.

Based on the sensitivity analysis of the SCM, the optimal leaching conditions were determined by considering the combined effect of temperature, sulfuric acid concentration and the pulp density. For this analysis a particle radius of 5 µm was considered.

Increasing temperature, enhances both the diffusion coefficient and reaction rate, accelerating sulfuric acid transport and surface reaction. A temperature of 75 °C was selected as the optimal, offering a practical balance between leaching efficiency and energy input. Regarding the sulfuric acid concentration, increasing $C_{\mathrm{H_2SO_4}}$ significantly reduced the dissolution time, specifically up to 2500-3000 $\mathrm{mol/m^3}$. Therefore, from an economic and environmental perspective the optimal sulfuric acid concentration lies between 2000 and 3000 $\mathrm{mol/m^3}$. Lower pulp densities improve leaching kinetics due to a higher acid-to-solid ratio, but results in smaller batch yields. To balance kinetics and throughput, the optimal pulp density was identified as the point where two half pulp density experiments would take longer than one full density experiment. This crossover occurred when two individual experiments at 60 $\mathrm{kg/m^3}$ required more time than a single experiment at 120 $\mathrm{kg/m^3}$, which was selected as the optimal value. As shown in Table 3.2, the selected optimal conditions in this study are in close agreement with those reported in literature.

Table 3.2: Comparison of Optimal Leaching Conditions from Literature and Current Study

Parameter	Swain et al. (2007)[46]	Jha et al. (2013) [7]	Current Study
Temperature [°C]	75	75	75
Sulfuric Acid Conc. [mol/m^3]	2000	2000	2500–3000
Particle Radius [µm]	4.15	5	5
Pulp Density [g/L]	100	100	120
H_2O_2 Concentration [vol%]	5	5	–

Both Swain et al.[46] and Jha et al.[7] used comparable temperatures, sulfuric acid concentrations, and pulp densities, supporting the validity of the identified trends. However, it should be noted that these studies used an $\mathrm{H_2O_2}$ concentration of 5 vol%, which was not explicitly accounted for in the current model.

3.2. Comparison to experimental results

To evaluate the validity of the model, a comparison was made to experimental results [7]. This study also focused on the leaching behaviour of $\mathrm{LiCoO_2}$ particles using sulfuric acid and hydrogen peroxide, and the effects of sulfuric acid concentration, temperature, pulp density and hydrogen peroxide concentration were analysed. According to their findings, the optimal leaching conditions were a 2 M sulfuric acid concentration at 75 °C with a pulp density of 100 g/L and a 5 $\%$ (v/v) $\mathrm{H_2O_2}$ concentration. Under these conditions, after 60 minutes, 99.1% of Li and 70% of Co were leached. These leaching conditions are used as input for the developed model, which predicts complete dissolution of the $\mathrm{LiCoO_2}$ particles after 62.5 minutes. Assuming that Li leaching directly corresponds to the shrinking particle core, the

leaching efficiency of Li can be calculated as follows [32]:

$$X = 1 - \frac{\text{unreacted volume}}{\text{initial volume}} = 1 - \frac{\frac{4}{3}\pi r_c^3}{\frac{4}{3}\pi r_s^3} = 1 - \frac{r_c^3}{r_s^3} \tag{3.10}$$

in which X represents the fraction of Li extracted, with:

- X=0 meaning no Li has been leached yet ($r_c = r_s$)
- X≈1 meaning all Li has been leached ($r_c \approx 0$)

Since the model tracks the shrinking core radius over time, the leaching efficiency was calculated. In Figure 3.6 the leaching efficiencies obtained from the model are compared to the experimental results.

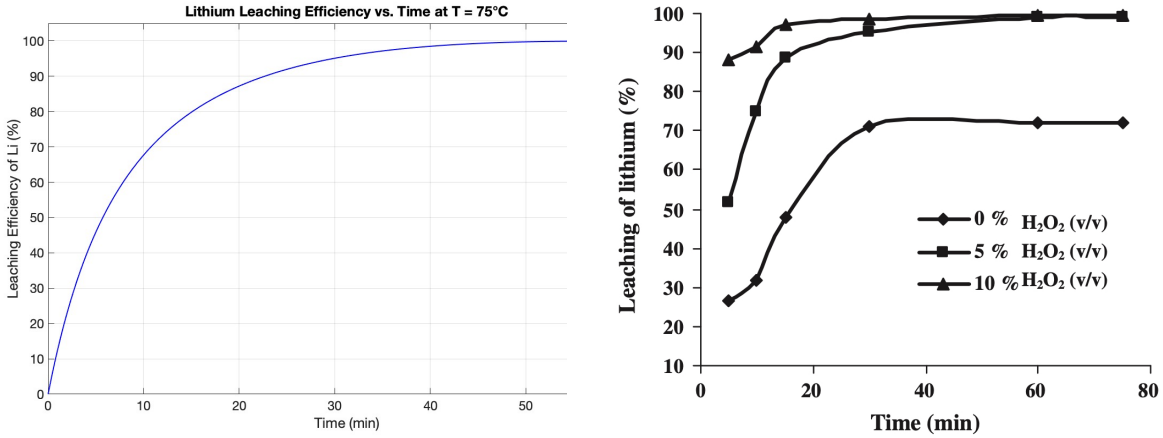

(a) Leaching efficiency of Li from the model

(b) Leaching efficiency of Li from the experiment [7]

Figure 3.6: Comparison between modelled (a) and experimental (b) leaching efficiencies of lithium

The modelled lithium leaching efficiency is shown in Figure 3.6a, using a dimensionless SCM and previously defined parameters, including the rate constant k. The value for k was adopted from a study based on the leaching of$\mathrm{LiCoO_2}$ using hydrochloric acid in the absence of $\mathrm{H_2O_2}$. Consequently, the modelled results should be compared to the experimental data in Figure 3.6b corresponding to 0 vol% $\mathrm{H_2O_2}$, where no reducing agent was used.

From this comparison, it becomes evident that the model overestimates the lithium leaching efficiency. The model predicts 100% Li extraction within the first 50 minutes, while the experimental data show that Li leaching plateaus around 70%. This discrepancy likely originates from the model's assumption that Li diffuses easily and faces little resistance when exiting the $\mathrm{LiCoO_2}$ particle. This assumption might be valid at the start of the leaching process, as Li is partly located near the particle surface and does not undergo a chemical reaction during leaching, but instead dissolves rapidly into the solution. This assumption no longer holds as the reaction proceeds. Li extraction becomes increasingly limited due to the formation of a cobalt oxide crust around the shrinking core. This crust formation introduces a growing diffusion barrier, reducing the effective mobility of lithium ions. Experimental data supports this, showing that Li extraction slows down and eventually plateaus around 70%, indicating a maximum amount of Li that can be recovered under these conditions.

The model treats Li and Co dissolution independently; however, they are in fact chemically and physically coupled. As Co is leached and $\mathrm{Co_3O_4}$ is formed, it obstructs the pathway for Li ions and reduces the lithium leaching efficiency. The thickness of the $\mathrm{Co_3O_4}$ crust not only impedes Li transport, but also increases the diffusion length, thereby increasing the resistance to both Li and acid diffusion. From the sensitivity analysis, it was found that varying the porosity had a negligible effect on the dissolution time of the $\mathrm{LiCoO_2}$ particles. The Bruggeman model used to describe porosity does not adequately capture the physical resistance imposed by the crust.

The following sub question raised at the beginning of this chapter can now be addressed.

SQ4) Which parameters affect the leaching time and efficiency of $LiCoO_2$ particles most according to the dimensionless shrinking core model?

The parameters with the greatest impact on leaching time and efficiency of $\mathrm{LiCoO_2}$ particles were temperature (affecting the rate constant and diffusion coefficient), sulfuric acid concentration, pulp density and particle radius. It was found that higher acid concentrations and elevated temperatures substantially reduced the leaching time, while larger particle radii increased it significantly. Larger pulp density increased the dissolution time due to reduced acid-to-solid ratio, with a more pronounced slowdown observed at values beyond 120 $\mathrm{kg/m^3}$. Sensitivity analysis identified the optimal leaching conditions as a temperature of $75°$C, a sulfuric acid concentration of 2500–3000 mol/m^3, a pulp density of 120 kg/m^3 and a particle radius of 5 µm. The trends observed in how these parameters affect leaching performance were consistent with those reported in literature and similar optimal leaching conditions were found. However, the model overestimates Li leaching efficiency compared to experimental result, which show nearly 100% Li efficiency within 30 minutes. In contrast, the model predicts a stagnation in leaching efficiency around 70%. This discrepancy arises partly because the model assumes that Li can diffuse freely out of the $\mathrm{LiCoO_2}$ particle, without fully accounting for the increasing resistance caused by the formation of a $\mathrm{Co_3O_4}$ crust. Additionally, the model does not differentiate between Li and Co leaching and does not account for the effect of $\mathrm{H_2O_2}$. These limitations will be addressed in the SCM described in the next section.

3.3. A shrinking core model with varying crust

This section presents a redefined model for the leaching of $\mathrm{LiCoO_2}$ particles in acidic media, based on the model developed by Cerrillo-Gonzalez. The model incorporates the transition from reaction-controlled to diffusion-controlled regimes, as a result of the formation of a $\mathrm{Co_3O_4}$ crust around the $\mathrm{LiCoO_2}$ particle. The formation of a $\mathrm{Co_3O_4}$ crust during the leaching was confirmed through X-ray Photoelectron Spectroscopy analysis, which enabled analysis of the composition of different layers of the solid particles [47]. The outer layer was found to consist mainly of $\mathrm{Co_3O_4}$, while the inner regions retained the original structure of $\mathrm{LiCoO_2}$. This layered composition suggests that Li was removed from the surface and that $\mathrm{Co_3O_4}$ was formed as an insoluble layer. This passivating layer hinders acid penetration and, in the absence of a strong reducing agent, slows down Li and Co recovery [48]. Unlike the previous model, this one separately tracks the leaching efficiencies of Li and Co. Additionally, it takes into account the effect of the varying $\mathrm{Co_3O_4}$ crust and assesses the effect of the $\mathrm{H_2O_2}$ concentration on the leaching kinetics.

For the leaching of $\mathrm{LiCoO_2}$ in this model, hydrochloric acid (HCl) was used. According to the literature, chloride ions (Cl^-) could act as reducing agents by facilitating the reduction of $\mathrm{Co^{3+}}$ to $\mathrm{Co^{2+}}$. This expectation is based on the standard electrode potential ($E°$) of the following half-reactions:

$$\mathrm{Co^{3+} + e^- \rightarrow Co^{2+}} \quad E° = +1.920\ \mathrm{V} \tag{3.11}$$

$$\mathrm{Cl_2 + 2e^- \rightarrow 2Cl^-} \quad E° = +1.358\ \mathrm{V} \tag{3.12}$$

The reduction potential for Equation 3.11 is higher than that of Equation 3.12, and therefore, the reduction of $\mathrm{Co^{3+}}$ to $\mathrm{Co^{2+}}$ is thermodynamically favourable in principle. However, experimental results indicate that chloride ions do not act as the reducing agent. Instead, water is oxidized to oxygen gas, serving as the electron donor. Based on these observations, the following redox reactions were proposed [6].

- **Reaction 1**:

$$\mathrm{LiCoO_2\ (s) + 2H^+ \rightarrow Li^+ + \frac{1}{2}Co^{2+} + \frac{1}{6}Co_3O_4\ (s) + H_2O + \frac{1}{6}O_2} \tag{3.13}$$

- **Reaction 2**:

$$\mathrm{Co_3O_4 + 6H^+ \rightarrow 3Co^{2+} + 3H_2O + \frac{1}{2}O_2} \tag{3.14}$$

Equation 3.13 shows that Li dissolves readily as $\mathrm{Li^+}$, while only a fraction of Co dissolves as $\mathrm{Co^{2+}}$. The remaining Co forms a solid $\mathrm{Co_3O_4}$ crust around the unreacted core. Over time, the $\mathrm{Co_3O_4}$ crust

converts into Co^{2+} (as shown in Equation 3.14), and this is a slow reaction. To minimize crust formation and enhance Li and Co dissolution, the addition of H_2O_2 is suggested, as it enhances the reduction of Co^{3+} to Co^{2+} and improves the leaching efficiency [45]. This gives the following reactions:

- **Reaction 3**:

$$LiCoO_2 + 3H^+ + \frac{1}{2}H_2O_2 \rightarrow Li^+ + Co^{2+} + 2H_2O_2 + \frac{1}{2}O_2 \tag{3.15}$$

- **Reaction 4**:

$$Co_3O_4 + 6H^+ + H_2O_2 \rightarrow 3Co^{2+} + 4H_2O_2 + O_2 \tag{3.16}$$

From Equation 3.15, it can be observed that no solid Co_3O_4 forms. Other studies have demonstrated that the addition of H_2O_2 significantly enhances the dissolution of $LiCoO_2$ in HCl solution. This improvement was thermodynamically supported by lower Gibbs free energy values for the reactions involving H_2O_2 compared to those without H_2O_2 [49].

Model Assumptions

1. The dissolution of $LiCoO_2$ using hydrochloric acid as a leaching agent and hydrogen peroxide as a reducing agent follows Equations: 3.13-3.16, which occur simultaneously.
2. The particles in the model are spherical and have a radius r_s=5 µm. The total particle size and number of particles remain constant, while the radius of the unreacted core r_c decreases over time.
3. The kinetic rates of the reactions 1, 2, 3 and 4 (eq: 3.13-3.16) are given as:

$$r_1 = k_1 \left(\frac{N_p 4\pi r_c^2}{V_r} \right) C_{H^+}^{core} \tag{3.17}$$

$$r_2 = k_2 \left(C_{Co_3O_4} \right) \left(C_{H^+}^{core} \right)^{2/3} \tag{3.18}$$

$$r_3 = k_3 \left(\frac{N_p 4\pi r_c^2}{V_r} \right) \left(C_{H^+}^{core} \right)^{1/3} \left(C_{H_2O_2} \right)^2 \tag{3.19}$$

$$r_4 = k_4 \left(C_{Co_3O_4} \right) \left(C_{H^+}^{core} \right)^{2/3} \left(C_{H_2O_2} \right)^2 \tag{3.20}$$

   These expressions depend on the surface area, proton concentration, hydrogen peroxide concentration and the rate constants k_1, k_2, k_3 and k_4, which were estimated by parametric fitting to experimental data and are shown in Table 3.3. The influence of solid Co_3O_4 was incorporated into the kinetics, as its mass changes over time and affects diffusion resistance. A more detailed explanation on this is provided in section D.2.
4. The production rates of Li^+, Co^{2+}, H^+, H_2O_2 and Co_3O_4 are equal to the change in concentration of the species and are given by:

$$\frac{dC_{Li^+}}{dt} = r_{Li^+} = r_1 + r_3 \tag{3.21}$$

$$\frac{dC_{Co^{2+}}}{dt} = r_{Co^{2+}} = \frac{1}{2}r_1 + 3r_2 + r_3 + 3r_4 \tag{3.22}$$

$$\frac{dC_{H^+}}{dt} = r_{H^+} = -2r_1 - 6r_2 - 3r_3 - 6r_4 \tag{3.23}$$

$$\frac{dC_{H_2O_2}}{dt} = r_{H_2O_2} = -\frac{1}{2}r_3 - r_4 \tag{3.24}$$

$$\frac{dC_{Co_3O_4}}{dt} = r_{Co_3O_4} = \frac{1}{6}r_1 - r_2 - r_4 \tag{3.25}$$

5. The self-ionization reaction of water is

$$\mathrm{H_2O} \rightleftharpoons \mathrm{H^+} + \mathrm{OH^-} \tag{3.26}$$

with an equilibrium constant:

$$K_\mathrm{w} = [H^+][OH^-] = 10^{-14} \tag{3.27}$$

In the model, it is assumed that the system maintains equilibrium. This means that any change in the $\mathrm{H^+}$ concentration as a result of acid addition or leaching reaction will result in an adjustment of $\mathrm{OH^-}$. This ensures accurate pH control during the process. However, in the reconstructed model this equilibrium adjustment was not included.

6. The activity coefficient for ions in a solution quantifies the deviation between the physical concentration and the ideal value. The effective concentrations are used for the kinetics:

$$a_\mathrm{i} = \gamma_\mathrm{i} C_\mathrm{i} \tag{3.28}$$

in which a_i is the effective concentration. γ_i is the activity coefficient and C_i is the actual molar concentration [50]. With activity coefficients of γ_i=0.75 for monovalent ions such as $\mathrm{Li^+}$ and $\mathrm{H^+}$ and γ_i=0.3 for divalent ions such as $\mathrm{Co^{2+}}$. Therefore, the kinetic rate expressions described in equations:3.17-3.20 use $\mathrm{C_{H^+}^{core,\ eff}} = 0.75 * \mathrm{C_{H^+}^{core}}$

7. As the leaching of $\mathrm{LiCoO_2}$ proceeds, the concentration of $\mathrm{Co_3O_4}$ starts to increase and a porous outer layer of $\mathrm{Co_3O_4}$ around the $\mathrm{LiCoO_2}$ forms and the overall particle size remains constant. The diffusion of $\mathrm{H^+}$ through the solid porous crust of $\mathrm{Co_3O_4}$ can be described by

$$V_\mathrm{r} \frac{dC_{\mathrm{H^+}}^{\text{bulk}}}{dt} = -\frac{D_{\mathrm{H^+}}^{\text{eff}} (C_{\mathrm{H^+}}^{\text{bulk}} - C_{\mathrm{H^+}}^{\text{core}})}{(r_\mathrm{s} - r_\mathrm{c})} N_\mathrm{p} (4\pi r_\mathrm{s} r_\mathrm{c}) \tag{3.29}$$

Here, $\mathrm{C_{H^+}^{bulk}}$ and $\mathrm{C_{H^+}^{core}}$ are the $\mathrm{H^+}$ concentration in the bulk and at the core respectively. $\mathrm{D_{H^+}^{eff}}$ is the effective diffusion coefficient of $\mathrm{H^+}$ through the $\mathrm{Co_3O_4}$ layer and is described by

$$D_{\mathrm{H^+}}^{\text{eff}} = D_{\mathrm{H^+}} \varepsilon \, exp(k_\mathrm{D}(r_\mathrm{s} - r_\mathrm{c})(1 - \varepsilon)) \tag{3.30}$$

Here, $D_{\mathrm{H^+}}$ = 9.311×10^{-9} $\mathrm{m^2\ s^{-1}}$ is the diffusion coefficient at infinite dilution, $\mathrm{k_D}$ ($\mathrm{m^{-1}}$) quantifies the increase in resistance to mass transport as the $\mathrm{Co_3O_4}$ crust grows, and ε is the porosity which changes as the $C_{\mathrm{Co_3O_4}}$ changes and can be determined as follows:

$$\varepsilon = 1 - \frac{V_{\text{solid}}}{V_{\text{shell}}} = 1 - \frac{C_{\mathrm{Co_3O_4}} M_{\mathrm{Co_3O_4}} V_r}{N_\mathrm{p} \rho_{\mathrm{Co_3O_4}} \frac{4}{3}\pi (r_\mathrm{s}^3 - r_\mathrm{c}^3)} \tag{3.31}$$

and a derivation is shown in appendix D.3.

8. In the model, it is determined whether the process is controlled by chemical reaction at the $\mathrm{LiCoO_2}$ core or by diffusion through the product layer. This is evaluated using the Da number which is defined as the ratio of the chemical reaction rate to the mass transfer rate.

$$Da = \frac{\text{kinetic rate}}{\text{diffusion rate}} \tag{3.32}$$

To determine the Da number, two limiting cases are considered:

   (a) The chemical reaction rate is calculated by assuming that the proton concentration at the core is equal to the bulk concentration $C_{\mathrm{H^+}}^{\text{core}} = C_{\mathrm{H^+}}^{\text{bulk}}$.

   (b) The diffusion rate is calculated by assuming that the proton concentration at the core is zero $C_{\mathrm{H^+}}^{\text{core}} = 0$

Both reactions in Equation 3.13 and Equation 3.15 require protons to be transported to the core. As $\mathrm{Co_3O_4}$ is formed, proton transport is increasingly hindered. Therefore the diffusion rate for both reactions is given by:

$$r_{1,3\text{diffusion}} = -\frac{D_{\mathrm{H^+}}^{\text{eff}} \left(C_{\mathrm{H^+}}^{\text{bulk}} - C_{\mathrm{H^+}}^{\text{core}}\right)}{(r_\mathrm{s} - r_\mathrm{c})} \frac{N_\mathrm{p} (4\pi r_\mathrm{s} r_\mathrm{c})}{V_\mathrm{r}} \tag{3.33}$$

The Da numbers for reaction r_1 and r_3 are calculated as:

$$Da_1 = \frac{r_{1,\text{kinetic}}}{r_{1,\text{ diffusion}}} = \frac{k_1(\frac{N_p 4\pi r_c^2}{V_r})C_{H^+,core}}{D_{eff}\frac{(C_{H^+,bulk}-0)}{(r_s-r_c)}\frac{N_p(4\pi r_s r_c)}{V_r}} \tag{3.34}$$

$$Da_3 = \frac{r_{3,\text{kinetic}}}{r_{3,\text{ diffusion}}} = \frac{k_3(\frac{N_p 4\pi r_c^2}{V_r})C_{H^+core}^{1/3}C_{H_2O_2}^2}{D_{eff}\frac{(C_{H^+,bulk}-0)}{(r_s-r_c)}\frac{N_p(4\pi r_s r_c)}{V_r}} \tag{3.35}$$

This results in two Da numbers, one for r_1 and one for r_3. In the scheme below, it is explained which kinetic regime governs the process.

Chemical Reaction Control ($Da_{II} \leq 1$):

$$r_1 = k_1\left(\frac{n_p\,4\pi r_c^2}{V_r}\right)\left(C_{H^+,core}\right)$$
$$r_2 = k_2\,C_{Co_3O_4}\left(C_{H^+,core}\right)^{2/3}$$
$$r_3 = k_3\left(\frac{n_p\,4\pi r_c^2}{V_r}\right)\left(C_{H^+,core}\right)^{1/3}\left(C_{H_2O_2}\right)^2$$
$$r_4 = k_4\,C_{Co_3O_4}\left(C_{H^+,core}\right)^{2/3}\left(C_{H_2O_2}\right)^2$$

Diffusion Control ($Da_{II} > 1$):

$$r_1 = \frac{D_{H^+}^{eff}\left(C_{H^+,bulk}-C_{H^+,core}\right)}{(R_p-r_c)}\left(\frac{n_p\,4\pi R_p r_c}{V_r}\right)$$
$$r_2 = k_2\,C_{Co_3O_4}\left(C_{H^+,bulk}\right)^{2/3}$$
$$r_3 = \frac{D_{H^+}^{eff}\left(C_{H^+,bulk}-C_{H^+,core}\right)}{(R_p-r_c)}\left(\frac{n_p\,4\pi R_p r_c}{V_r}\right)$$
$$r_4 = k_4\,C_{Co_3O_4}\left(C_{H^+,bulk}\right)^{2/3}\left(C_{H_2O_2}\right)^2$$

Table 3.3: Parameters and their (initial) values used in simulation results.

Parameter	Description	Value	Units
k_1	Rate constant, Eq. 3.13	2.17×10^{-8}	[m/s]
k_2	Rate constant, Eq. 3.14	8.33×10^{-9}	[$m^2 mol^{-2/3} s^{-1}$]
k_3	Rate constant, Eq. 3.15	6.67×10^{-11}	[$m^5 mol^{-4/3} s^{-1}$]
k_4	Rate constant, Eq. 3.16	1.67×10^{-12}	[$m^8 mol^{-8/3} s^{-1}$]
k_D	Diffusion factor	-3.2×10^7	[m^{-1}]
D_H	Diffusion coefficient	9.311×10^{-9}	[m^2/s]
V_r	Reaction volume	50×10^{-6}	[m^3]
ρ_{LiCoO_2}	Density of $LiCoO_2$	4800	[kg/m^3]
M_{LiCoO_2}	Molar mass of $LiCoO_2$	0.09787	[kg/mol]
$\rho_{Co_3O_4}$	Density of Co_3O_4	6110	[kg/m^3]
$M_{Co_3O_4}$	Molar mass of Co_3O_4	0.2408	[kg/mol]
m_{LiCoO_2}	Mass of $LiCoO_2$	2.5	[g]
n_{LiCoO_2}	Moles of $LiCoO_2$	0.0255	[mol]
N_p	Number of particles	10^9	[–]
$C_{Co_3O_4,0}$	Initial Co_3O_4 concentration	0	[mol/m^3]
$C_{Li^+,0}$	Initial Li^+ concentration	0	[mol/m^3]
$C_{Co^{2+},0}$	Initial Co^{2+} concentration	0	[mol/m^3]
$C_{LiCoO_2,0}$	Initial $LiCoO_2$ concentration	510	[mol/m^3]
$C_{H_2O_2}$	Initial H_2O_2 concentrations	[0, 86, 163, 260]	[mol/m^3]
$C_{H^+,bulk}$	Bulk proton concentration	[500, 1500, 2500]	[mol/m^3]

The original model was developed in COMSOL Multiphysics [6]. However, the model was rebuilt and implemented in MATLAB using an ODE solver. At each time step the ODE solver updates the system state, which includes the concentrations of Li^+, Co^{2+}, H^+ and H_2O_2, as well as the formation and dissolution of Co_3O_4 and the shrinking of the $LiCoO_2$ radius. All initial values for the parameters are given in Table 3.3. Compared to the original COMSOL model, two main modifications were introduced. The first modification was that the proton concentration at the particle surface $C_{H^+,core}$ is continuously updated over time, rather than the abrupt change assuming either $C_{H^+,core} = C_{H^+,bulk}$ or $C_{H^+,core} = 0$. Secondly, the reaction rates r_2 and r_3 were modified, using a maximum function between the core and bulk proton concentrations to ensure that dissolution can proceed even when $C_{H^+,core}$ becomes low due to diffusion limitation. In appendix D.4 a detailed description of the MATLAB model workflow is provided.

3.4. Leaching dynamics and Co_3O_4 Formation

The SCM with a varying crust, originally developed by Cerrillo-Gonzalez et al., was successfully reconstructed in this study. Figure 3.7 presents the model's predictions for Li and Co extraction, as well as the concentrations of H^+ and H_2O_2 as a function of time. These values were evaluated based on the initial values listed in Table 3.3 considering C_{H^+} of 500, 1500 and 2500 mol/m^3 and $C_{H_2O_2}$ of 0, 86, 173 and 260 mol/m^3.

The model developed by Cerrillo-Gonzalez et al. closely matched experimental data for $LiCoO_2$ leaching in hydrochloric acid and is shown in appendix D.1. The results shown in Figure 3.7 reproduce the same extraction trends for Li and Co under identical conditions. Therefore, it can be considered that the reconstructed model effectively describes the experimental leaching efficiencies.

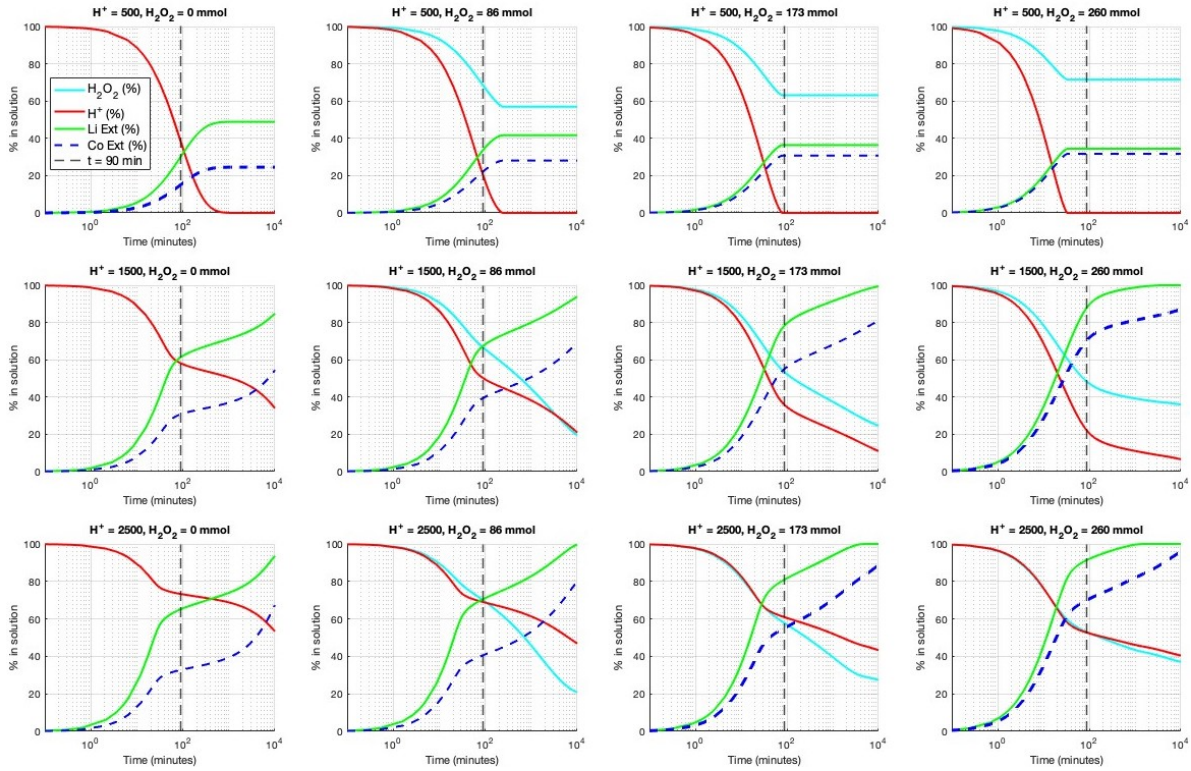

Figure 3.7: Model results for the leaching efficiency of Li and Co under various H^+ and H_2O_2 concentrations

The results show that in general Li is extracted faster and to a greater extent than Co during the earlier stages of leaching (90 minutes). Higher H^+ concentrations enhance both the extraction efficiency and leaching kinetics. In the absence of H_2O_2, Li leaches at approximately twice the rate of Co, following a 2:1 stoichiometric ratio. At low acid concentrations the process can become limited by proton availability. Increasing the H_2O_2 concentration significantly improves Co extraction and also leads to high Li extraction.

To evaluate the effect of $C_{H_2O_2}$, the evolution of the Da number, the extraction percentage of Li and Co, the accumulation of Co_3O_4 and the core radius were analysed for the first two hours for two different H_2O_2 concentrations: 0 and 173 mol/m^3, while maintaining a constant H^+ concentration of 2500 mol/m^3. The results are shown in Figure 3.8a-c and Figure 3.9a-c.

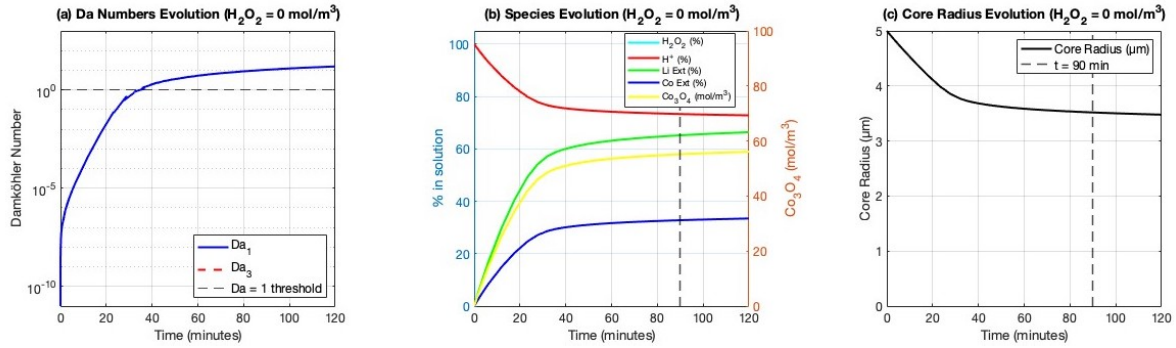

Figure 3.8: Evolution of the Da number, species and radius for the first 120 minutes for $C_{\mathrm{H_2O2}} = 0\ \mathrm{mol/m^3}$ and $C_{\mathrm{H_2SO_4}}$=2500 $\mathrm{mol/m^3}$

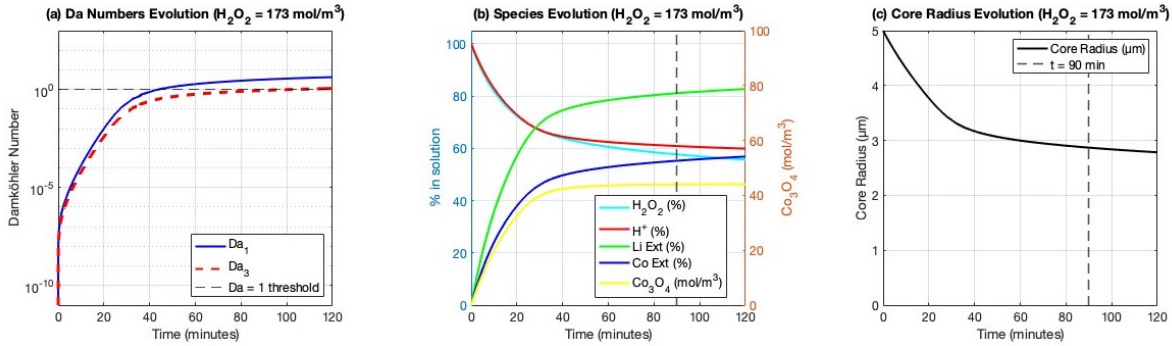

Figure 3.9: Evolution of the Da number, species and radius for the first 120 minutes for $C_{\mathrm{H_2O2}} = 173\ \mathrm{mol/m^3}$ and $C_{\mathrm{H_2SO_4}} = 2500\mathrm{mol/m^3}$

Both systems exhibit a rapid increase in metal extraction within the first 20-40 minutes, which is typical for a kinetically controlled regime. This behaviour is further confirmed by the evolution of the Da numbers ($\mathrm{Da_1}$ and $\mathrm{Da_3}$) remaining below 1 during this initial stage, indicating that the surface reaction at the $\mathrm{LiCoO_2}$ core is the rate-limiting step, with negligible diffusion resistance. As the leaching proceeds, $\mathrm{Co_3O_4}$ gradually forms on the particle surface, creating a diffusion resistance for the proton transport. The key results after 120 minutes of leaching for systems with and without $\mathrm{H_2O_2}$ are summarized in Table 3.4.

Table 3.4: Comparison of metal extraction, Co_3O_4 accumulation, and core radius after 120 minutes of leaching.

Parameter	**Without H_2O_2**	**With H_2O_2**
Cobalt extraction [%]	33.4	56.8
Lithium extraction [%]	66.4	82.7
$C_{\mathrm{Co_3O_4}}$ [mol/m^3]	60	45
Core radius [µm]	3.48	2.78
Time when $\mathrm{Da_1} > 1$ [min]	35	44
Time when $\mathrm{Da_3} > 1$ [min]	NA	102

In the absence of $\mathrm{H_2O_2}$, the Li and Co extraction reaches 66.4% and 33.4%, respectively. In contrast, leaching with $\mathrm{H_2O_2}$ increases Li extraction to 82.7% and Co to 56.8%. This is due to $\mathrm{H_2O_2}$ facilitating the reduction of $\mathrm{Co^{3+}}$ to soluble $\mathrm{Co^{2+}}$ and thereby preventing the formation of a $\mathrm{Co_3O_4}$ layer. This is confirmed by the significantly higher accumulation of $\mathrm{Co_3O_4}$ in systems without $\mathrm{H_2O_2}$, which increases

the diffusion resistance for H^+ ions. This effect is reflected in the evolution of the Da numbers (Da_1 and Da_3), which mark the transition of a kinetically controlled regime towards a diffusion-controlled regime. In the absence of H_2O_2 the transition from kinetic to diffusion control (indicated by $Da_1 > 1$) occurs after 35 minutes, while in the presence of H_2O_2 the transition is delayed to 44 minutes, while for Da_3 it occurs at 102 minutes. Overall, the addition of H_2O_2 not only increases the Li and Co extraction and also reduces the formation of Co_3O_4, thereby delaying the onset of diffusion control. In Figure 3.10a-c and Figure 3.11a-c the results are shown for a leaching duration of 120 minutes to 10000 minutes ($\approx$ 9 days).

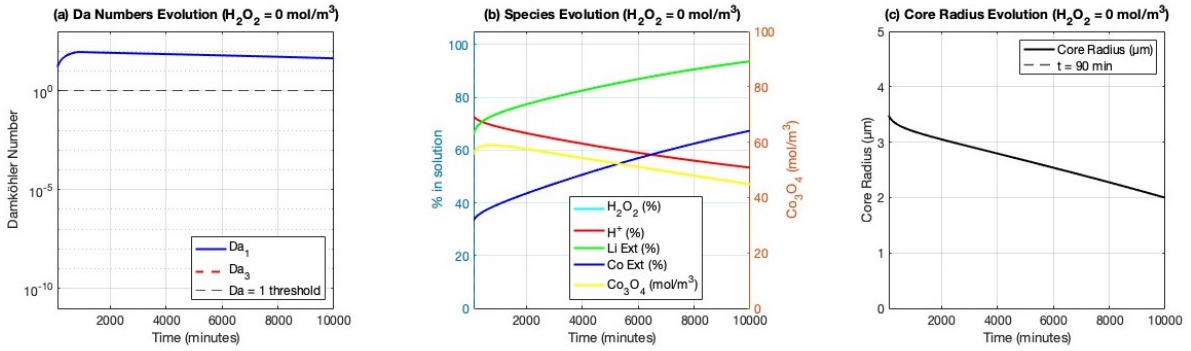

Figure 3.10: Evolution of Da number, species concentrations and core radius from 120 to 10000 minutes for $C_{H_2O2} = 0$ mol/m^3 and $C_{H_2SO_4}$=2500 mol/m^3

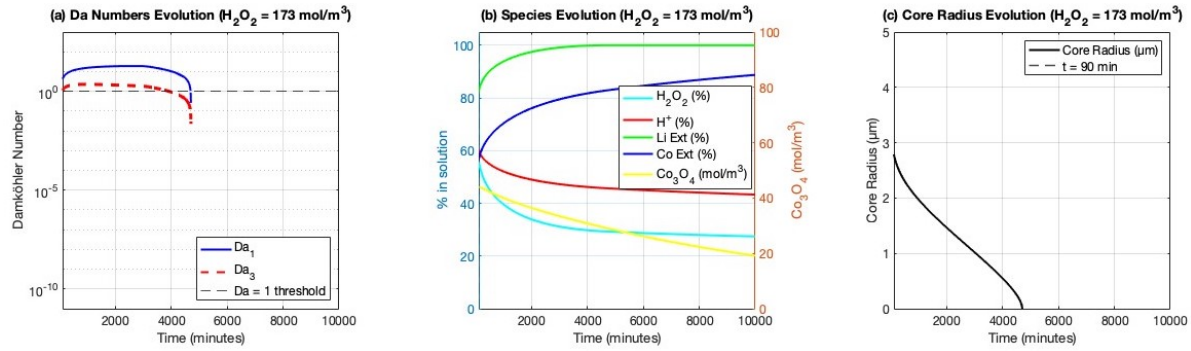

Figure 3.11: Evolution of Da number, species concentrations and core radius from 120 to 10000 minutes for $C_{H_2O2} = 173$ mol/m^3 and $C_{H_2SO_4}$=2500 mol/m^3

The key results after 10000 minutes of leaching for systems with and without H_2O_2 are listed in Table 3.5:

Table 3.5: Comparison of metal extraction, Co_3O_4 accumulation, and core radius after 10000 minutes of leaching.

Parameter	Without H_2O_2	With H_2O_2
Cobalt extraction [%]	67.3	88.7
Lithium extraction [%]	93.6	99.97
Co_3O_4 concentration [mol/m^3]	44.8	19.1
Core radius [µm]	2	0

In the absence of H_2O_2 the evolution of the Da number stabilizes above 1, indicating that the system has entered the diffusion-controlled regime as illustrated in Figure 3.10a. As a result, the Co_3O_4 de-

creases slowly over time, limiting the Li and Co extraction. After 1000 minutes, Li and Co extraction reach 93.8% and 67.3% , respectively. While Li extraction is relatively high, the remaining core radius of approximately 2 µm indicates that complete particle dissolution has not yet been achieved.

In the presence of $\mathrm{H_2O_2}$ significantly faster extraction of Li and Co is observed. Both Da_1 and Da_3 remain larger than 1, confirming a diffusion controlled regime. However, due to a reduced accumulation of $\mathrm{Co_3O_4}$ during the first 120 minutes (19.4 vs 45 $\mathrm{mol/m^3}$) the diffusion barrier is less pronounced, resulting in substantial higher metal recovery. After approximately 4200 minutes, the core radius of the $\mathrm{LiCoO_2}$ particles has shrunk to zero, coinciding with Li extraction reaching nearly 100%. The Co extraction continues beyond this point through the dissolution of the remaining $\mathrm{Co_3O_4}$. The Da numbers become undefined once the core radius shrinks to zero, as the kinetic rate expressions are radius dependent. To conclude, the presence of $\mathrm{H_2O_2}$ leads to higher metal extraction as the $\mathrm{Co_3O_4}$ build-up is limited and delays diffusion limitations. In contrast, without $\mathrm{H_2O_2}$, $\mathrm{Co_3O_4}$ build up is higher, leading to earlier diffusion limitation and lower Li and Co recovery.

3.5. Application to sulfuric acid-driven leaching

Following the recommendations outlined in the work of Cerrillo-Gonzalez et al. [6], the model developed in this study is expanded to simulate the leaching behaviour using sulfuric acid. The model is based on the proton activity rather than $\mathrm{Cl^-}$, and the key reaction, the reduction of $\mathrm{Co^{3+}}$ to $\mathrm{Co^{2+}}$ remains the same. Therefore, the model is expected to be applicable to sulfuric acid with $\mathrm{H_2O_2}$ as a reducing agent.

A previous study demonstrated that complete leaching of both Li and Co can be achieved within 10 minutes using a 2 M $\mathrm{H_2SO_4}$ solution with 5 vol% $\mathrm{H_2O_2}$ at a pulp density of 100 $\mathrm{g/L}$ and a temperature of 75°C [46]. Based on these findings, the model parameters were adjusted to evaluate the model's applicability to sulfuric acid systems.

In the updated model $\mathrm{H_2SO_4}$ replaces HCl as the leaching agent. Since each $\mathrm{H_2SO_4}$ molecule could theoretically donate 2 protons, the concentration in the system is approximated as $C_{\mathrm{H^+}}$=4 M for a 2 M $\mathrm{H_2SO_4}$ solution, although not all protons may dissociate. While the $\mathrm{H_2O_2}$ concentration is given in volume percent, the model uses a molar concentration ($\mathrm{mol/m^3}$). The conversion method is described in appendix D.5. To apply the model at $75\,^{\circ}\mathrm{C}$, the rate constants were adjusted using the Arrhenius equation, with activation energies of $E_{\mathrm{a,Co}}$ = 59.81 $\mathrm{kJ/mol}$ and $E_{\mathrm{a,Li}}$= 32.4$\mathrm{kJ/mol}$ [7]. The temperature-adjusted rate constants are calculated as follows:

$$
\begin{aligned}
k_{1,new} &= k_1 \exp\left(\frac{E_{a,\mathrm{Li}}}{R}\left(\frac{1}{298}-\frac{1}{348}\right)\right)\\
k_{2,new} &= k_2 \exp\left(\frac{E_{a,\mathrm{Co}}}{R}\left(\frac{1}{298}-\frac{1}{348}\right)\right)\\
k_{3,new} &= k_3 \exp\left(\frac{E_{a,\mathrm{Li}}}{R}\left(\frac{1}{298}-\frac{1}{348}\right)\right)\\
k_{4,new} &= k_4 \exp\left(\frac{E_{a,\mathrm{Co}}}{R}\left(\frac{1}{298}-\frac{1}{348}\right)\right)
\end{aligned}
\tag{3.36}
$$

The activation energies were assigned based on the primary metal involved in each reaction step. Reactions 1 and 3 primarily describe the dissolution of Li and therefore k_1 and k_3 are corrected using $E_{a,\mathrm{Li}}$. Reaction 2 and 4 describe the dissolution of Co and therefore k_2 and k_4 are corrected using $E_{a,\mathrm{Co}}$. The baseline for the model parameters used in the sulfuric acid leaching simulations is listed in Table 3.6.

Table 3.6: Baseline conditions and rate constants used for sulfuric acid leaching simulations at $75°$C.

Parameter	Value	Units
$C_{\mathrm{H_2SO_4}}$	2000	[mol/m^3]
$C_{\mathrm{H_2O_2}}$	500	[mol/m^3]
Pulp density	100	[g/L]
T	75	[°C]
r_{s}	4.15×10^{-6}	[m]
V_{r}	500	[mL]
$k_{1,\mathrm{new}}$	1.42×10^{-7}	[m/s]
$k_{2,\mathrm{new}}$	2.67×10^{-7}	[m^2 mol$^{-2/3}$ s^{-1}]
$k_{3,\mathrm{new}}$	4.37×10^{-10}	[m^5 mol$^{-4/3}$ s^{-1}]
$k_{4,\mathrm{new}}$	5.36×10^{-11}	[m^8 mol$^{-8/3}$ s^{-1}]

In the following analysis, all variables will be held constant except one. This variable will be varied over a defined range to evaluate its effect on the leaching efficiencies of Li and Co and to compare to experimental results.

Effect of $\mathrm{H_2O_2}$ concentration

The $\mathrm{H_2O_2}$ concentration was varied from 0 to 2500 $\mathrm{mol/m^3}$ and the leaching efficiencies after 30 minutes are shown in Figure 3.12.

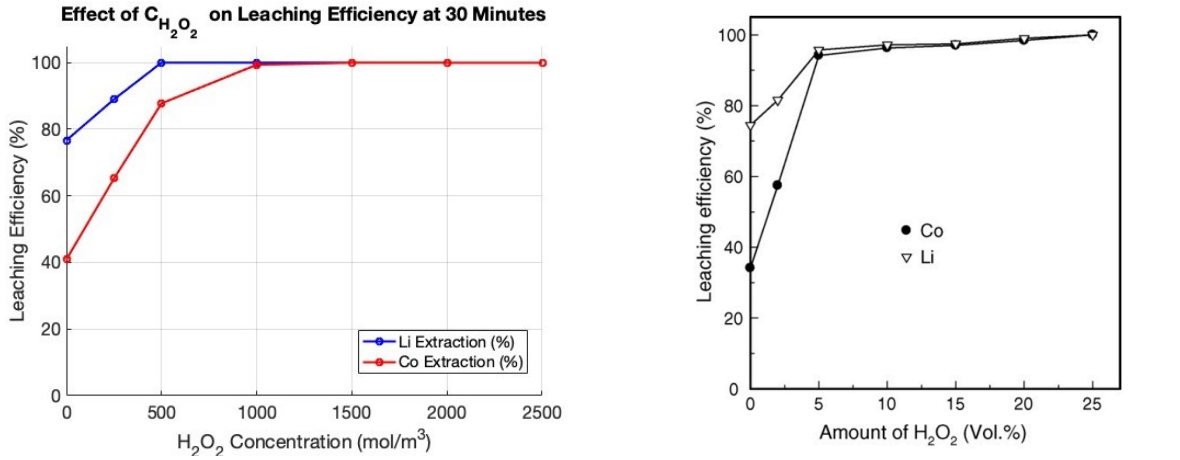

(a) Model: Leaching efficiency vs. $\mathrm{H_2O_2}$ concentration

(b) Experiment: Leaching efficiency vs. $\mathrm{H_2O_2}$ concentration [51].

Figure 3.12: Comparison between modelled (a) and experimental (b) leaching efficiencies as a function of $\mathrm{H_2O_2}$ concentration.

Both modelled and experimental data show that increasing $\mathrm{H_2O_2}$ concentrations significantly improves the leaching efficiency of Li and Co. Without $\mathrm{H_2O_2}$, notably lower leaching efficiencies are obtained, particularly for Co. This is consistent with previous findings where Co becomes trapped as $\mathrm{Co_3O_4}$ which dissolves slowly, leading to a transition to a diffusion-controlled system. The model predicts complete Li extraction at a concentration of 500 $\mathrm{mol/m^3}$, while the experimental data show a more gradual increase in Li recovery, continuing up to 25 vol % $\mathrm{H_2O_2}$. However, the overall trend of enhanced extraction with increasing acid concentration is consistent between model and experiment. In appendix D.6 an analysis of the effect of $\mathrm{H_2O_2}$ concentration on the leaching efficiencies is described in more detail.

Effect of $\mathrm{H_2SO_4}$ concentration

To study the effect of sulfuric acid concentration, $C_{\mathrm{H^+}}$ was varied from 0 to 8000 $\mathrm{mol/m^3}$, assuming complete dissociation of $\mathrm{H_2SO_4}$. The results after 30 minutes are shown in Figure 3.13.

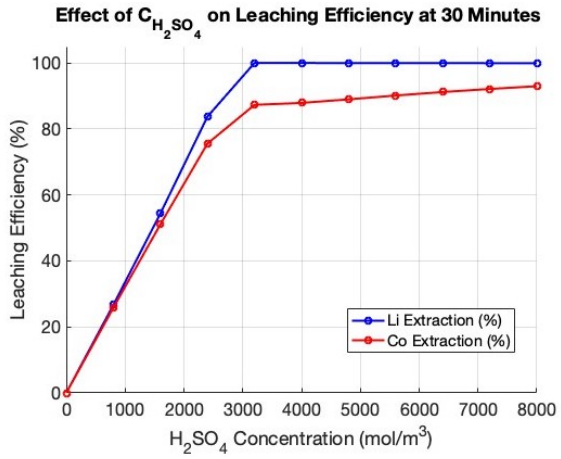

(a) Model: Leaching efficiency vs. H_2SO_4 concentration.

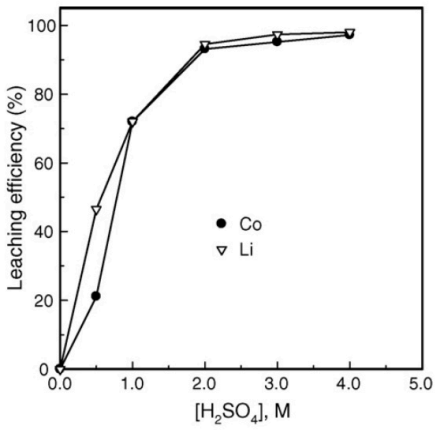

(b) Experiment: Leaching efficiency vs. H_2SO_4 [51].

Figure 3.13: Comparison between modelled (a) and experimental (b) leaching efficiencies as a function of H_2SO_4 concentration.

From Figure 3.13 several notable differences are observed. The model predicts similar leaching efficiencies for both Li and Co for low acid concentrations and divergence for higher concentrations. In contrast, the experimental data show that at low acid concentrations, the Li and Co extraction efficiencies differ and converge for higher concentrations. Additionally, the model overestimates the sulfuric acid concentration required for complete Li extraction. Nevertheless, both the model and experimental data show that an increase in sulfuric acid concentration enhances the Li and Co extraction rates.

Effect of temperature

The effect of temperature was investigated by varying it from 20 to 90 °C. Leaching efficiencies after 30 minutes are shown in Figure 3.14.

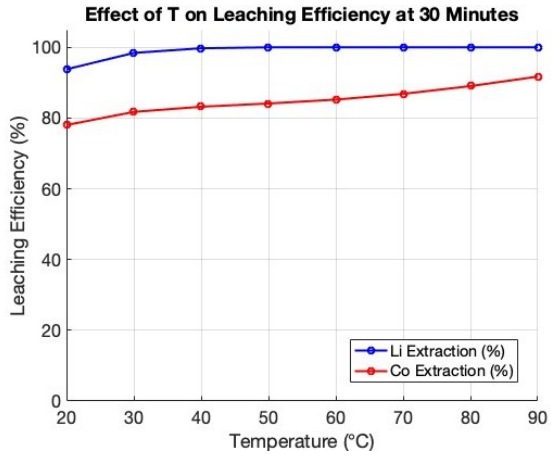

(a) Model: Leaching efficiency vs. T

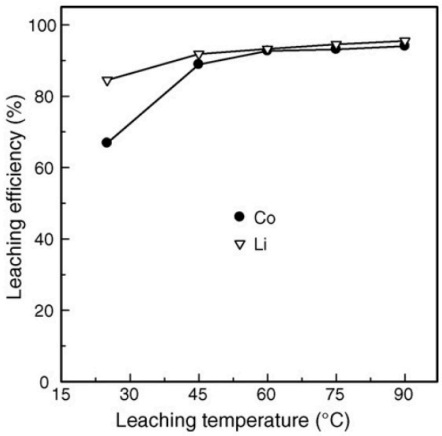

(b) Experiment: Leaching efficiency vs. T [51].

Figure 3.14: Comparison between modelled (a) and experimental (b) leaching efficiencies as a function of T

Both model and experimental data show increased Li and Co leaching efficiencies with temperature. However, the model overestimates the leaching efficiencies at low temperatures. For instance, predicting 95% Li and 80% Co extraction at T=25°C, while the experimental results are lower. Additionally, Li extraction reaches completion at lower temperatures in the model than in the experiments, while Co extraction increases more gradually with similar efficiencies observed in both the model and experimental data.

Effect of pulp density

Pulp density was varied from 10 to 125 g/L and leaching efficiencies after 30 minutes are shown in Figure 3.15.

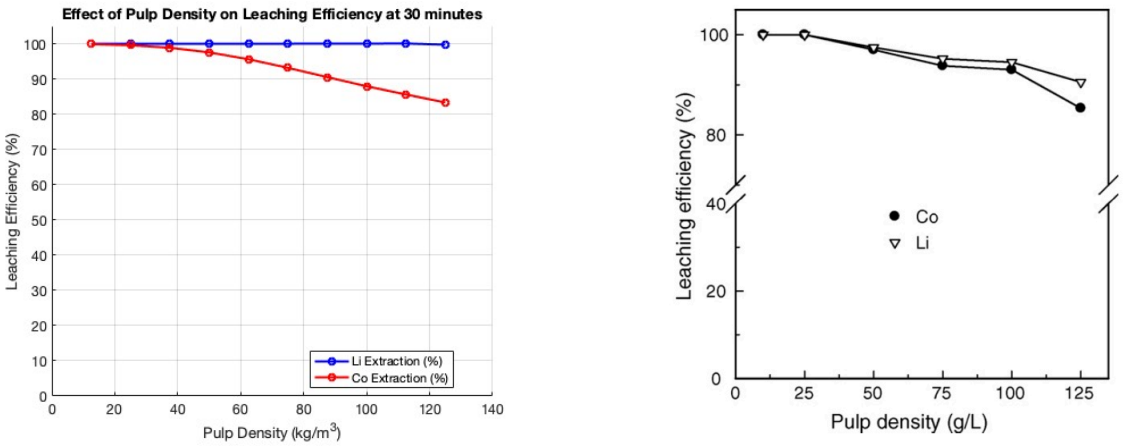

(a) Model: Leaching efficiency vs. pulp density

(b) Experiment: Leaching efficiency vs. pulp density [51].

Figure 3.15: Comparison between modelled (a) and experimental (b) leaching efficiencies as a function of T

Increasing the pulp density does not result in a noticeable effect on the Li leaching efficiency. This contrasts with the experimental results, which show a slight decrease in the leaching efficiency of Li at higher pulp densities. In the case of Co, both model and experimental results show a small decline in leaching efficiencies at higher pulp densities. This reduction in leaching efficiency can be attributed to a reduced available surface area per unit volume of solution, as previously discussed.

Effect of particle radius

The effect of the particle radius on the leaching efficiencies was investigated by increasing the particle radius of $LiCoO_2$ particles from 5 µm to 50 µm. The leaching efficiencies predicted by the model after 30 minutes are shown in Figure 3.12.

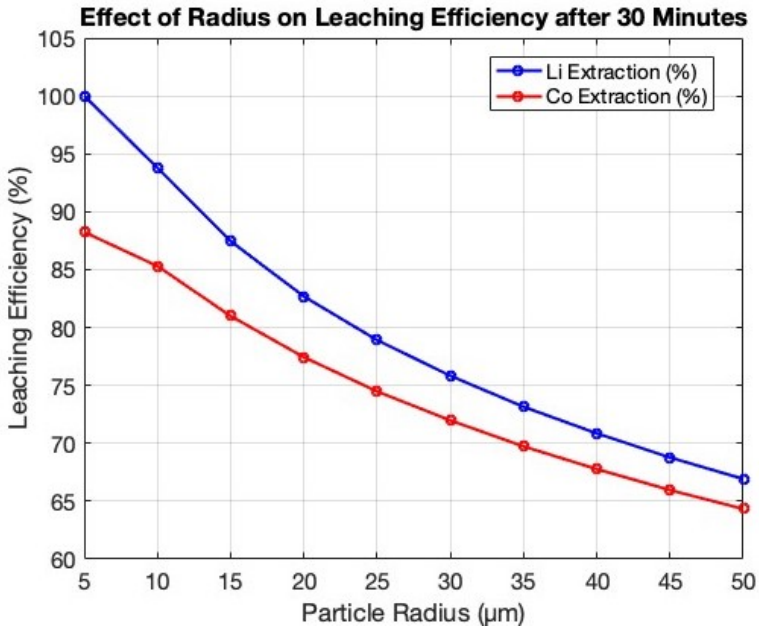

Figure 3.16: Leaching efficiency vs. particle radius

The results show that leaching efficiencies decrease significantly for increasing particle radius. As the particle radius increases from 5 µm to 50 µm, the Li leaching efficiency decreases from nearly 100% to 66%, while Co leaching decreases from 89% to 64%. This behaviour is attributed to two main factors: a lower surface area-to-volume ratio for larger particles, resulting in slower reaction rates and a longer diffusion path length. Both hinder the leaching process. These findings are consistent with a previous experimental study, which reported lower leaching efficiencies for both Li and Co in larger $\mathrm{LiCoO_2}$ particles when using ascorbic acid as a leaching agent [52]. This behaviour is also illustrated in Figure 3.17 and Figure 3.18, in which the leaching of $\mathrm{LiCoO_2}$ was modelled for two particle sizes: r_s= 5 µm and r_s= 50 µm.

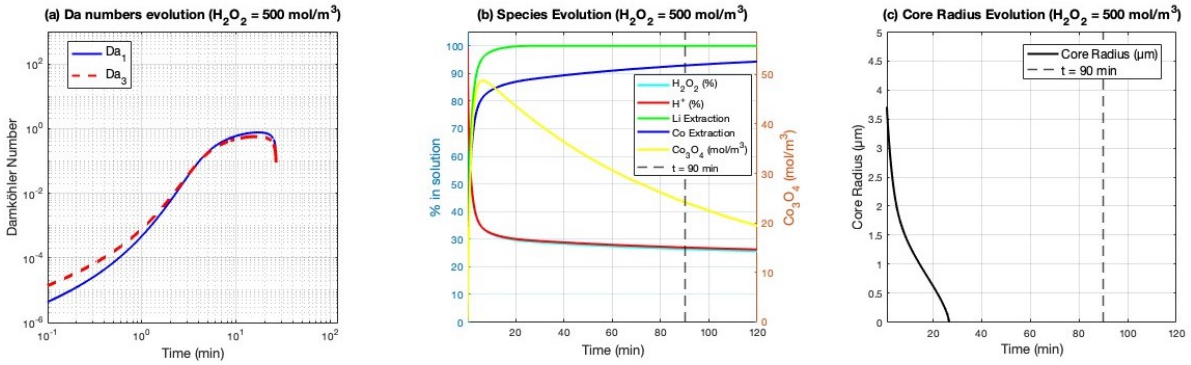

Figure 3.17: Evolution of Da number, species concentrations and core radius for r_s=5 µm

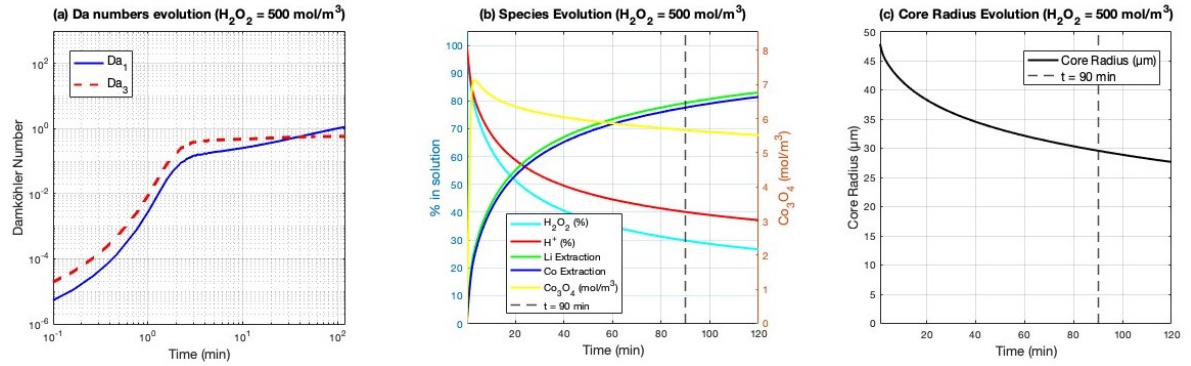

Figure 3.18: Evolution of Da number, species concentrations and core radius for r_s=50 µm

For particles with a radius of r_s=5 µm, the dissolution of the metals occurs rapidly with a higher leaching efficiency for Li than for Co, which is consistent with Li being more easily accessible and more mobile. From Figure 3.17a it can be seen that both Da numbers stay well below 1, indicating that the system remains in the kinetically controlled regime. Complete radius shrinkage occurs after about 26 minutes. In contrast, increasing the particle radius to r_s = 50 µm, results in significantly lower leaching efficiencies for Li and Co. From Figure 3.18b, it is observed that the leaching efficiencies of Li and Co converge and core radius shrinks more slowly. This is due to the transition to a diffusion-controlled regime, indicated by $\mathrm{Da_1} > 1$ after approximately 94 minutes. The convergence in Li and Co extraction is linked to the dependence of the reaction rates $\mathrm{r_1}$ and $\mathrm{r_3}$ on the available reactive surface area. As shown in Equation 3.17 and Equation 3.19, the reaction rates depend on the total surface area of all $\mathrm{LiCoO_2}$ particles, which can be expressed as:

$$r_1, r_3 \propto N_\mathrm{p} r_\mathrm{c}^2 \tag{3.37}$$

The number of particles N_p is inversely proportional to the cube of the particle radius r_s given by:

$$N_\mathrm{p} = \frac{V_\mathrm{solid}}{V_\mathrm{particle}} = \frac{\frac{m_\mathrm{solid}}{\rho_\mathrm{solid}}}{\frac{4}{3}\pi r_\mathrm{s}^3} \propto \frac{1}{r_\mathrm{s}^3} \tag{3.38}$$

Substituting this into the reaction rates and assuming r_s=r_c shows that:

$$r_1, r_3 \propto \frac{1}{r_s} \tag{3.39}$$

Thus, r_1 and r_3 scale inversely with the particle radius r_s. As particle size increases, the total reactive surface area per unit volume decreases, resulting in lower overall reaction rates. Since the Li extraction rate depends on the available surface area, it becomes limited as surface availability decreases, leading to a convergence of Li and Co leaching rates at larger particle sizes. A comparison of Figure 3.17 and Figure 3.18 shows that the total Co_3O_4 concentration formed is significantly less for larger particles (50 µm) compared to smaller ones (5 µm). This reduction aligns with the decreased reactive surface area in larger particles and supports the use of $C_{Co_3O_4}$ as an approximation of the effective surface area in rate expressions r_2 and r_4.

Despite the lower total accumulation of Co_3O_4 in larger particles, both Li and Co leaching rates are reduced. This apparent contradiction can be explained by two coupled effects. While the total amount of Co_3O_4 formed is lower for larger particles, the amount that forms per particle is higher. Since larger particles reduce the number of particles at fixed pulp density, more Co_3O_4 per particle, reducing the porosity of the product layer and thereby decreasing the effective diffusion coefficient H^+ as described in Equation 3.30 and Equation 3.31. Secondly larger particles have a thicker crust and longer diffusion path lengths, which further lowers the rate at which H^+ ions can reach the unreacted core. Together, these effects result in lower leaching efficiencies for both Li and Co at larger particle sizes, despite lower total Co_3O_4 accumulation in the system.

3.6. Comparison between developed models

To evaluate the differences in predictive capability of the models developed in section 3.1 and section 3.3, simulations were carried out under the following leaching conditions: $C_{H_2SO_4} = 2000\ mol/m^3$, a pulp density of 100 g/L, and a temperature of 75 °C. Since the model developed in section 3.1 does not account for the presence of H_2O_2, it is assumed that $C_{H_2O_2}$=0 mol/m^3. The simulation results for both models are shown in Figure 3.19.

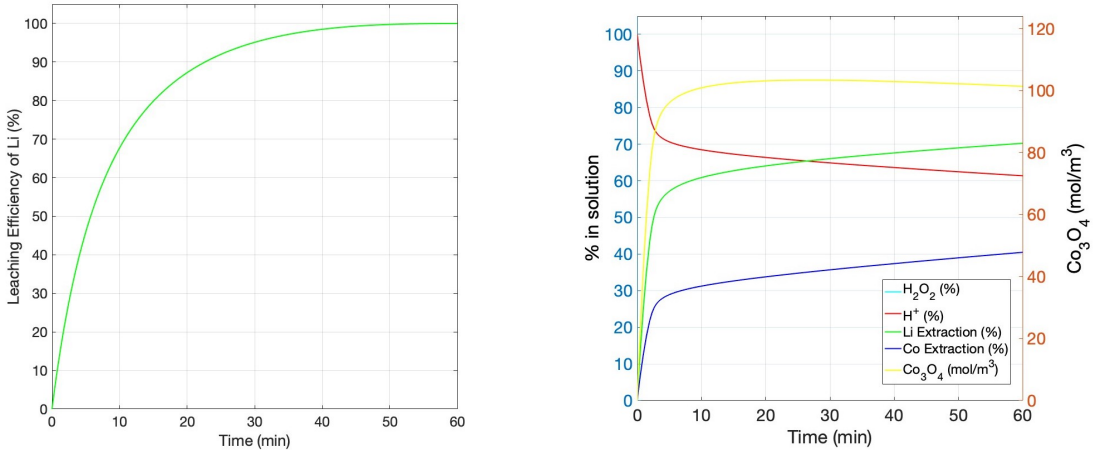

(a) Leaching using the dimensionless SCM

(b) Leaching using SCM with a varying crust

Figure 3.19: Comparison of leaching behaviour using the dimensionless SCM (a) and the SCM with varying crust(b)

The dimensionless SCM predicts Li leaching solely based on the shrinking radius of the unreacted $LiCoO_2$ core. In this model, Li is treated as the species of interest and the model does not differentiate between Li and Co dissolution or their interaction during the leaching. The diffusion of Li out of the $LiCoO_2$ particle experiences little resistance. In contrast, the SCM with varying crust provides a more detailed description of the leaching behaviour, capturing the leaching efficiencies of Li and Co separately and also the formation and dissolution of Co_3O_4.

Experimental results show that in the absence of H_2O_2 only 30% of Co and 70% of Li was leached

under similar conditions [7]. The dimensionless SCM predicts nearly complete Li dissolution after 60 minutes. In contrast, the SCM with varying crust shows a steep initial increase, followed by a slower increase in both Li and Co leaching. This can be attributed to the large amount of Co_3O_4 that has formed.

Overall, the SCM with varying crust provides a more realistic leaching profile. The stagnation in Li and Co leaching efficiencies aligns more closely with the experimental trends, supporting that the dimensionless SCM does not capture the resistance introduced by the formation of the crust. This highlights the need to incorporate physical barriers, such as the Co_3O_4 layer, to simulate realistic leaching behaviour of $LiCoO_2$ in sulfuric acid.

The following sub questions raised at the beginning of this chapter can now be addressed.

SQ5) How does the shrinking core model with varying crust improve the representation of diffusion and reaction processes compared to the dimensionless model?

The SCM with varying crust developed in this study introduces various important extensions compared to the SCM developed in section 3.1. First, it accounts for the formation and dissolution of a passivating Co_3O_4 layer during the leaching process, a phenomenon confirmed by experimental observations. This layer significantly affects the leaching kinetics, as it creates a diffusion resistance to proton transport, which is not captured in the dimensionless SCM. Second, the model distinguishes between the leaching behaviours of Li and Co, rather than treating the material as a single entity. Separate kinetic expressions are defined for the dissolution of $LiCoO_2$ and Co_3O_4, which provides a more accurate representation of the leaching of the different species. Third, the model also incorporates the concentration of H_2O_2 and its effect on dissolution behaviour. H_2O_2 acts as a reducing agent which promotes the reduction of Co^{3+} to Co^{2+}, accelerating the Co leaching. This effect was not represented in the dimensionless SCM. Finally, the model evaluates the transition from a kinetically-controlled to a diffusion-controlled regime by calculating the dimensionless Da_1 and Da_3 numbers.

These improvements are reflected in simulations results using a sulfuric acid concentration of 2000 mol/m^3. Adding 173 mol/m^3 of H_2O_2 increased Co extraction from 33.4% to 56.8% and Li from 66.4% to 82.7% after 120 minutes. The Co_3O_4 concentration also decreased from 60 to 45 mol/m^3, delaying the onset of diffusion control. Together, these enhancements enable the model to more accurately capture the physical and chemical complexities of the leaching process, resulting in a more realistic prediction of Li and Co leaching under different operational conditions.

SQ6) To what extent does the shrinking core model with a varying crust replicate experimental leaching trends for $LiCoO_2$ in sulfuric acid, such as lithium and cobalt recovery under varying operational conditions?

A previously developed SCM using HCl as a leaching agent was first reconstructed and shown to closely match both the original model and corresponding experimental data. The simulation results show that higher HCl concentrations lead to increased leaching efficiencies and that in the absence of H_2O_2, Li is leached in higher rates than Co, approximately in a 2:1 stoichiometric ratio. The addition of H_2O_2 significantly increases the Co leaching efficiency and also improved Li extraction.

The developed model was subsequently adapted to simulate leaching using sulfuric acid and successfully reproduced key experimental trends. It captures the trend that higher leaching efficiencies for both Li and Co are obtained for higher H_2SO_4 and H_2O_2 concentrations, as well as at elevated temperatures. It shows a decline in Co leaching efficiency at higher pulp densities due to limited acid availability, similar to the experimental results. Additionally, the model was tested for larger particle sizes and showed reduced leaching efficiencies for both Li and Co due to a reduced available surface area, consistent with experimental observations.

However, also some discrepancies between the experimental data and model were observed. Specifically, it overestimates leaching at low acid concentrations and fails to capture the decline at higher pulp densities. One possible cause for this discrepancy is the uncertainty in the rate constants, which were not experimentally determined at T=$75°$C but extrapolated using the Arrhenius equation. Despite

these limitations, the model overall captures the dominant trends from the experimental data and can provide a solid basis for describing the leaching behaviour of $\mathrm{LiCoO_2}$ using sulfuric acid.

Finally, the SCM with varying crust and the dimensionless SCM were compared to experimental results under the optimal leaching conditions, without $\mathrm{H_2O_2}$. The dimensionless SCM only predicted the dissolution of the $\mathrm{LiCoO_2}$ particle, which was translated to the leaching efficiency of Li. The model predicted 100% Li leaching and did account for the resistance build up during the process for Li leaching. In contrast, the SCM with varying crust showed a rapid increase in both Li and Co leaching efficiencies followed by a slowdown as a result of the accumulated $\mathrm{Co_3O_4}$ crust. The model predicted final leaching efficiencies of approximately 70% for Li and 30% for Co, which closely matched experimental data.

4

Conclusion and recommendations

This master thesis investigated two recycling methods focussed on the recovery of valuable materials from spent LIB: (i) the physical separation of graphite via Magnetic Density Separation (MDS), and (ii) the chemical recovery of lithium and cobalt from $LiCoO_2$ by hydrometallurgical leaching, modelled using a Shrinking Core Model (SCM). The goal of this thesis was to develop these models and assess their ability to reproduce experimentally observed trends. Chapter 2 focused on a model for MDS to simulate the levitation of graphite particles suspended in a paramagnetic $MnCl_2$ solution in a non-uniform magnetic field. First, the magnetic susceptibility of the $MnCl_2$ solution was studied. Thereafter, a particle tracking model was developed to simulate particle motion under the influence of the magnetic, gravitational, buoyant and drag force, using a magnetic field extracted from COMSOL. In Chapter 3, a SCM was developed to simulate the leaching behaviour of $LiCoO_2$ particles using sulfuric acid. Initially, a dimensionless model was built to describe the dissolution of $LiCoO_2$ particles and a sensitivity analysis was performed to identify key parameters influencing the dissolution process. Subsequently, a SCM with a varying Co_3O_4 product layer was rebuilt to incorporate additional physical and chemical effects, such as the influences of H_2O_2 concentration and Co_3O_4 formation. Finally, the model was adapted to sulfuric acid systems and evaluated for its ability to reproduce experimental trends under various leaching conditions.

4.1. Conclusions and recommendations

This section addresses the two research questions posed at the beginning of this thesis.

Research question 1

Can computational modelling predict the levitation behaviour of graphite in a Magnetic Density Separation system, and how well does it align with experimental observations?

A previous study demonstrated the physical feasibility of levitation of graphite particles in a saturated $MnCl_2$ solution. In the experiment, exposing the solution to a magnetic field caused graphite particles to levitate 5-6 mm above the bottom of the vial. Furthermore, ring-shaped particle clustering at the edges of the vial occurred and most particle movement had stopped after approximately 1-2 minutes. However, not all particles reached the same levitation height and some remained more dispersed throughout the medium.

Based on a force balance including magnetic, gravitational, buoyant and drag forces acting on graphite particles in a saturated $MnCl_2$ solution, a computational particle tracking model was developed to simulate the motion of 1000 graphite particles in two dimensions. The simulations used experimentally validated magnetic susceptibility values to ensure realistic force calculations. The model successfully reproduced the observed levitation height, with particles converging to 5-6 mm, and predicted lateral drift toward the vial walls.

The model also offered insights into the mechanisms behind these behaviours. It showed that smaller particles settled more slowly than larger ones, consistent with the force balance, where the time to reach equilibrium scaled inversely with the square of the particle diameter ($1/d^2$). To determine when a particle reached levitation height, two criteria were tested: a velocity-based criterion, defining equilibrium as a vertical velocity below $v_{\mathrm{pz}} < 10^{-8}$ and a position-based equilibrium, defining equilibrium as a vertical position between 5-7 mm. While the velocity-based criterion was more precise, the position-based criterion aligned better with visual observations and was used to assess settling time. Using this method the model showed that 20 µm-sized particles (average graphite size) reached equilibrium in about two minutes, matching experimental timescales. The model further attributed the observed horizontal drift to cross-gradient components in the magnetic force, arising from spatial variations in multiple directions of the magnetic field. When these components were omitted in the force balance, particles moved toward the centre, confirming their role in forming the ring-shaped clustering pattern.

This study demonstrates a computationally tractable model that accurately reproduces key spatial patterns such as levitation height and lateral clustering, and explains settling dynamics based on particle properties and magnetic field structure. It shows that relatively simple force-based simulations can support the design and optimization of MDS systems for LIB recycling, reducing reliance on costly experiments. Nevertheless, the current model has limitations that offer opportunities for future research to improve the model's accuracy and applicability to complex and more industrial-scale applications.

- **Dilute suspension assumption**:
  The model assumes a dilute suspension with a volume fraction below the 10^{-5} threshold for neglecting particle interactions. However, in regions of particle accumulation (e.g. levitation height or near the vial walls), local volume fraction likely exceeds this threshold. In these areas hydrodynamic interactions between particles may significantly affect the settling dynamics. To improve the predictions in these regions, future research should incorporate two-way or four-way coupling to account for fluid-particle and particle-particle interactions.
- **Simplified particle size and density distribution**:
  The current model only uses three distinct particle sizes with identical densities. This simplification does not capture the full heterogeneity in real black mass from spent LIBs, showing a wide variation in particle sizes, densities and magnetic properties. Future studies should experimentally characterize black mass distributions and use this data to extend the model's ability to predict the separation performance of these heterogeneous particle mixtures. This is particularly important for scaling MDS for industrial-scale application, where effective separation and sufficiently short settling times are essential for process feasibility.
- **Two-dimensional magnetic field representation**:
  The magnetic field was modelled in two dimensions (y and z directions). While this simplified approach was sufficient to capture levitation height and lateral drift, this simplification omits 3D effects that could influence particle clustering and dynamics. Future studies should focus on extending the model to a full 3D magnetic field, which would improve accuracy for scaling up the MDS process.
- **Particle aggregation**:
  Aggregation effects were not captured in the model, yet aggregation was observed in experiments and is expected to be more prominent in black mass materials. Aggregation could significantly affect particle behaviour and separation outcomes. Future studies should incorporate particle aggregation effects by modelling hydrodynamic interactions, to improve the accuracy of the MDS predictions.

Research question 2

Can a Shrinking Core Model predict lithium and cobalt recovery from $LiCoO_2$ during sulfuric acid leaching and how well does it replicate experimental results across varying conditions?

Two Shrinking Core Models (SCMs) were developed to simulate the leaching behaviour of $\mathrm{LiCoO_2}$ in sulfuric acid ($\mathrm{H_2SO_4}$). The first, a dimensionless SCM, assumed uniform particle shrinkage and was used to explore the effect of key leaching parameters. Sensitivity analysis identified the sulfuric

acid concentration, pulp density, temperature and particle size as most impactful parameters affecting the dissolution time. The model correctly predicted qualitative trends: higher acid concentration and temperature increased the leaching efficiency, while higher pulp densities and larger particles reduced it due to lower acid availability and larger diffusion resistance. However, the model overestimated Li recovery, predicting 100% extraction within 60 minutes. In contrast, experimental data showed Li recovery stagnating at 70% after 30 minutes. This discrepancy was due to the model excluding the formation of a Co_3O_4 layer during leaching, which progressively hinders acid diffusion to the core and Li diffusion out. Additionally, the model could not distinguish between Li and Co recovery, as the shrinking radius of the $LiCoO_2$ core was directly equated to Li dissolution and did not account for the catalytic effect of hydrogen peroxide (H_2O_2), both known to significantly influence leaching kinetics.

To address these limitations, a second SCM was developed based on the leaching of $LiCoO_2$ using hydrochloric acid (HCl). It incorporated the progressive formation of a porous Co_3O_4 crust around each $LiCoO_2$ particle and dynamically linked porosity to the amount of Co_3O_4 precipitated. This evolving directly influenced the effective diffusion coefficient of the acid, introducing a time-dependent diffusion resistance to mass transport. Li and Co dissolution were modelled separately using kinetic expressions determined for both $LiCoO_2$ and Co_3O_4, leading to a more precise representation of their leaching behaviour. The effect of H_2O_2 was also explicitly included and showed that higher H_2O_2 concentrations improved the dissolution rates of both metals, particularly cobalt. Additionally, the model used Dämkohler numbers, ratios of reaction rate to diffusion rate, to distinguish between diffusion- and reaction-controlled regimes.

The model was then adapted for sulfuric acid conditions and validated against experimental data. For example, under leaching without H_2O_2 it closely matched the experimentally observed leaching curves, capturing a rapid rise in extraction rates followed by a stagnation around 70% for Li and 30% for Co. In contrast the dimensionless SCM incorrectly predicted complete Li recovery. The SCM with varying crust also captured qualitative trends such as increased Li and Co recovery with higher H_2SO_4 and H_2O_2 concentrations, and found that higher temperatures accelerated extraction, while larger particles and higher pulp densities suppressed the leaching efficiency. While Co recovery matched well with experiments, Li recovery was consistently overestimated.

This work presents a novel SCM framework that integrates dynamic crust formation, porosity-controlled diffusion, metal-specific dissolution kinetics and the catalytic effect of H_2O_2 into a unified, physics-based model. Applied to sulfuric acid leaching of $LiCoO_2$, it accurately reproduces both the qualitative and quantitative leaching behaviour of Li and Co. Beyond capturing experimental trends, the model serves as a practical tool for identifying rate-limiting steps and optimizing leaching conditions, reducing reliance on experimental iteration. However, several important limitations remain and should be addressed in future research.

- **Assuming a quiescent fluid environment**:
  Both models assume a stagnant liquid with a uniform sulfuric acid concentration in the bulk. However, in realistic leaching processes, especially in stirred reactors, fluid flow can cause significant local differences in acid transport and reactant availability. In particular, turbulence can enhance mass transfer by increasing relative velocity between the fluid and particle surfaces. It can cause uneven distributions of H^+ ions in the fluid, meaning that some particles may be exposed to higher acid concentrations than others depending on their location in the flow. Additionally, the turbulent flow may affect particles of different sizes unequally, leading to non-uniform leaching rates across the particle population. These effects can significantly accelerate leaching compared to what the current model predicts. Since these flow-related phenomena are not yet considered, future research should explore how fluid motion and local hydrodynamic conditions influence the dissolution process. For example, the model could be extended to include a particle size distribution and simulate how turbulence impacts the leaching behaviour of a heterogeneous particle population.

- **Simplified treatment of porosity and tortuosity**:
  Porosity effects in the SCM with varying crust were approximated based on the amount of $\mathrm{Co_3O_4}$ formed around each particle. Since it is difficult to measure directly, its calculation relied on estimation in this thesis. However, porosity significantly influences the effective diffusion coefficient of acid and, consequently, the overall leaching kinetics. Future studies should aim to experimentally characterize the evolution of porosity and tortuosity over time, through porosimetry for example. Accurately capturing the evolution of the porosity over time improves the model's prediction of diffusion behaviour and better represents the dynamic development of the crust.
- **Uncertainties in diffusion and rate constants**:
  Due to a lack of available experimental data at elevated temperatures, key parameters such as the diffusion coefficients and rate constants were extrapolated to higher temperatures using the Arrhenius equation. These estimates could not be validated against experimental results. The rate constant, in particular, had a major impact on the model's predictions, meaning that inaccurate values could significantly impact the calculated leaching efficiency. For instance, in the SCM with varying crust Li recovery was consistently overestimated across several conditions, suggesting that the dissolution kinetics or diffusion resistance for Li may not be fully captured by the current model. Future work should focus on experimentally determining these parameters under realistic sulfuric acid conditions to improve the model's reliability and predictive accuracy
- **Uncertainty in surface crust composition**:
  The SCM with varying crust assumes that a $\mathrm{Co_3O_4}$ crust forms on the surface of the shrinking $\mathrm{LiCoO_2}$ particles during leaching, based on literature and X-ray photoelectron spectroscopy (XPS) measurements. However, the exact cobalt oxidation states from the XPS data collected during the leaching remain unconfirmed, and other oxides (e.g. CoO or $\mathrm{Co_2O_4}$) may form. This introduces uncertainty into the model, as it relies on the assumption that a $\mathrm{Co_3O_4}$ crust forms during the leaching. If other cobalt oxides are present, their different leaching behaviour, surface reactivity, or impact on porosity could lead to under- or overestimation of the crust's effect. To improve the reliability of the model, future research should identify the exact cobalt oxide using advanced XPS or other spectroscopy methods and modify the model to take into account the different oxide phases that may form under various leaching conditions. This would strengthen the evidence for surface layer formation and clarify which factors are limiting $\mathrm{LiCoO_2}$ leaching.
- **Extending the model to other electrode materials**:
  Future studies should investigate the applicability of the SCM for other electrode materials such as NMC, LFP, or LNMO. Gosh et al (2021) applied a SCM to model NCM cathode degradation, treating particles as shrinking cores surrounded by a growing surface layer, incorporating both diffusion and reaction kinetics at the core-shell interface [53]. Although their study focuses on electrochemical degradation rather than chemical leaching, the core-shell structure and transport-reaction interactions provide a useful analogy. Since black mass from LIBs typically contains a mixture of metal-bearing particles, it would be valuable to asses whether similar mechanisms can describe the leaching behaviour of these materials. This could contribute to the development of more generalised and predictive models for LIB recycling.

Bibliography

[1] T Kobayashi, T Mori, Y Akiyama, F Mishima, and S Nishijima. Study on separation of structural isomer with magneto-archimedes method. In *Journal of Physics: Conference Series*, volume 897, page 012018. IOP Publishing, 2017.

[2] Viktor Mikhailovich Boiko, Andrei Aleksandrovich Pivovarov, and SV Poplavski. Measurement of gas velocity in a high-gradient flow, based on velocity of tracer particles. *Combustion, Explosion, and Shock Waves*, 49:548–554, 2013.

[3] Christos D Tsakiroglou, Katerina Terzi, Christos Aggelopoulos, and Maria Theodoropoulou. A statistical shrinking core model to estimate the overall dechlorination rate of pce by an assemblage of zero-valent iron nanoparticles. *Chemical Engineering Science*, 167:191–203, 2017.

[4] H Scott Fogler. *Essentials of chemical reaction engineering: essenti chemica reactio engi*. Pearson education, 2010.

[5] Irene Hooijkaas. Assessing the viability of magnetic density separation for the recovery of graphite from black mass. Master's thesis, Delft University of Technology, Delft, Netherlands, October 2024. Instructor: L. Botto.

[6] María del Mar Cerrillo-Gonzalez, M Villen-Guzman, Carlos Vereda-Alonso, José Miguel Rodríguez-Maroto, and Juan Manuel Paz-Garcia. Acid leaching of licoo2 enhanced by reducing agent. model formulation and validation. *Chemosphere*, 287:132020, 2022.

[7] Manis Kumar Jha, Anjan Kumari, Amrita Kumari Jha, Vinay Kumar, Jhumki Hait, and Banshi Dhar Pandey. Recovery of lithium and cobalt from waste lithium ion batteries of mobile phone. *Waste management*, 33(9):1890–1897, 2013.

[8] Fortune Business Insights. Lithium-ion battery market size, share industry analysis, by type (lithium cobalt oxide, lithium iron phosphate, lithium nickel cobalt aluminum oxide, lithium manganese oxide, lithium nickel manganese cobalt, and lithium titanate oxide), by application (consumer electronics, automotive, energy storage system, industrial, and others), and regional forecast, 2024-2032, 2025. Accessed: 2025-03-18.

[9] Milan Grohol and Constanze Veeh. *Study on the Critical Raw Materials for the EU 2023*. Publications Office of the European Union, 2023.

[10] Youping Miao, Lili Liu, Yuping Zhang, Quanyin Tan, and Jinhui Li. An overview of global power lithium-ion batteries and associated critical metal recycling. *Journal of Hazardous Materials*, 425:127900, 2022.

[11] Bahar Moradi and Gerardine G Botte. Recycling of graphite anodes for the next generation of lithium ion batteries. *Journal of Applied Electrochemistry*, 46:123–148, 2016.

[12] Madhumitha Jaganmohan. Global graphite production and its implications for europe and the us. Statista, 2023. Accessed: 2023-06-14.

[13] Anna Vanderbruggen, Neil Hayagan, Kai Bachmann, Alexandra Ferreira, Denis Werner, Daniel Horn, Urs Peuker, Rodrigo Serna-Guerrero, and Martin Rudolph. Lithium-ion battery recycling—influence of recycling processes on component liberation and flotation separation efficiency. *ACS ES&T Engineering*, 2(11):2130–2141, 2022.

[14] CIRS Group. China imposes export control measures on graphite materials, 2023. Accessed: 2025-05-06.

[15] Anna Vanderbruggen, Aliza Salces, Alexandra Ferreira, Martin Rudolph, and Rodrigo Serna-Guerrero. Improving separation efficiency in end-of-life lithium-ion batteries flotation using attrition pre-treatment. *Minerals*, 12(1):72, 2022.

[16] International Energy Agency. *The role of critical minerals in clean energy transitions*. OECD Publishing, 2021.

[17] Natcha Wongnaree, Tapany Patcharawit, Tanongsak Yingnakorn, and Sakhob Khumkoa. Leaching kinetics of valuable metals from calcined material of spent lithium-ion batteries. *ACS omega*, 9(47):46822–46833, 2024.

[18] EU Regulation. 1542 of the european parliament and of the council of 12 july 2023 concerning batteries and waste batteries, amending directive 2008/98/ec and regulation (eu) 2019/1020 and repealing directive 2006/66/ec, 2023.

[19] David J Griffiths. *Introduction to electrodynamics*. Cambridge University Press, 2023.

[20] John MD Coey. *Magnetism and magnetic materials*. Cambridge university press, 2010.

[21] Daniel D Stancil and Anil Prabhakar. *Spin waves: problems and solutions*. Springer Nature, 2021.

[22] Jeff Sanny (Loyola Marymount University) Samuel J. Ling (Truman State University) and Bill Moebs. Magnetic field lines. https://phys.libretexts.org/Bookshelves/University_Physics/University_Physics_%28OpenStax%29/University_Physics_II_-_Thermodynamics_Electricity_and_Magnetism_%28OpenStax%29/11%3A_Magnetic_Forces_and_Fields/11.03%3A_Magnetic_Fields_and_Lines, Unknown. Accessed: 2024-10-26.

[23] Liang-Shih Fan and Chao Zhu. Principles of gas-solid flows. pages 87–89, 1999.

[24] Gerald Feinberg. Fall of bodies near the earth. *American Journal of Physics*, 33(6):501–502, 1965.

[25] CE Lapple and CB Shepherd. Calculation of particle trajectories. *Industrial & Engineering Chemistry*, 32(5):605–617, 1940.

[26] Clement Kleinstreuer. *Modern fluid dynamics*. Springer, 2018.

[27] JG M. Kuerten. Point-particle dns and les of particle-laden turbulent flow-a state-of-the-art review. *Flow, turbulence and combustion*, 97:689–713, 2016.

[28] HS Fogler. Rate laws. *Elements of chemical reaction engineering*, pages 243–320, 2020.

[29] S Yagi and D Kunii. Fifth international symposium on combustion. *Reinhold, New York*, page 231, 1955.

[30] Vida Safari, Gilnaz Arzpeyma, Fereshteh Rashchi, and Navid Mostoufi. A shrinking particle—shrinking core model for leaching of a zinc ore containing silica. *International Journal of Mineral Processing*, 93(1):79–83, 2009.

[31] JY Park and Octave Levenspiel. The crackling core model for the reaction of solid particles. *Chemical Engineering Science*, 30(10):1207–1214, 1975.

[32] Octave Levenspiel. *Chemical reaction engineering*. John wiley & sons, 1998.

[33] Openstax. Rate laws. https://chem.libretexts.org/Bookshelves/General_Chemistry/Chemistry_1e_(OpenSTAX)/12%3A_Kinetics/12.04%3A_Rate_Laws, unknown. Accessed: 2025-26-01.

[34] Bernhard Tjaden, Samuel J Cooper, Daniel JL Brett, Denis Kramer, and Paul R Shearing. On the origin and application of the bruggeman correlation for analysing transport phenomena in electrochemical systems. *Current opinion in chemical engineering*, 12:44–51, 2016.

[35] Fabio Montagnaro. Sherwood (sh) number in chemical engineering applications—a brief review. *Energies*, 17(17):4342, 2024.

[36] Georgios Maragkos and Tarek Beji. Review of convective heat transfer modelling in cfd simulations of fire-driven flows. *Applied Sciences*, 11(11):5240, 2021.

[37] TM Herrington, MG Roffey, and DP Smith. Densities of aqueous electrolytes mncl2, cocl2, nicl2, zncl2, and cdcl2 from 25 to 72 c at 1 atm. *Journal of chemical and engineering data (Print)*, 31(2):221–225, 1986.

[38] Joseph A Rard and Donald G Miller. Densities and apparent molal volumes of aqueous manganese, cadmium, and zinc chlorides at 25. degree. c. *Journal of Chemical and Engineering Data*, 29(2):151–156, 1984.

[39] Thermo Scientific. Manganese(ii) chloride, 99%, anhydrous, 80 mesh. `https://www.fishersci.se/shop/products/manganese-ii-chloride-99-anhydrous-80-mesh-thermo-scientific/p-44598`, 2025. Accessed: 2025-04-23.

[40] Shigeki Egami, Hideaki Monjushiro, and Hitoshi Watarai. Magnetic susceptibility measurements of solutions by surface nanodisplacement detection. *Analytical sciences*, 22(9):1157–1162, 2006.

[41] Katherine A Mirica, Sergey S Shevkoplyas, Scott T Phillips, Malancha Gupta, and George M Whitesides. Measuring densities of solids and liquids using magnetic levitation: fundamentals. *Journal of the American Chemical Society*, 131(29):10049–10058, 2009.

[42] O Miura, K Yamagishi, and D Yamamoto. Magneto-archimedes levitation of precious metals under a high magnetic field gradient. In *Journal of Physics: Conference Series*, volume 1054, page 012086. IOP Publishing, 2018.

[43] supermagnete.nl. How do you calculate the magnetic flux density?, n.d. Accessed: 2025-04-02.

[44] Abel van Rooijen. Towards circular batteries: Investigating particle size-based separation of active materials from spent li-ion batteries. Master's thesis, Delft University of Technology, Delft, Netherlands, March 2023. Instructor: L. Botto.

[45] Daniel Alvarenga Ferreira, Luisa Martins Zimmer Prados, Daniel Majuste, and Marcelo Borges Mansur. Hydrometallurgical separation of aluminium, cobalt, copper and lithium from spent li-ion batteries. *Journal of Power Sources*, 187(1):238–246, 2009.

[46] Basudev Swain, Jinki Jeong, Jae-chun Lee, Gae-Ho Lee, and Jeong-Soo Sohn. Hydrometallurgical process for recovery of cobalt from waste cathodic active material generated during manufacturing of lithium ion batteries. *Journal of Power Sources*, 167(2):536–544, 2007.

[47] María del Mar Cerrillo-González, M Villen-Guzman, Carlos Vereda-Alonso, César Gómez-Lahoz, José Miguel Rodríguez-Maroto, and Juan Manuel Paz-García. Recovery of li and co from licoo2 via hydrometallurgical–electrodialytic treatment. *Applied Sciences*, 10(7):2367, 2020.

[48] Maria del Mar Cerrillo-Gonzalez, Maria Villen-Guzman, Luis Fernando Acedo-Bueno, Jose Miguel Rodriguez-Maroto, and Juan Manuel Paz-Garcia. Hydrometallurgical extraction of li and co from licoo2 particles–experimental and modeling. *Applied Sciences*, 10(18):6375, 2020.

[49] D Sebastián Drajlin, Daniela S Suarez, Norman Toro, Edelmira D Gálvez, Eliana G Pinna, and Mario H Rodriguez. Comparative study of the dissolution of lco in hcl medium with and without h2o2. *Metals*, 12(5):727, 2022.

[50] LibreTexts. Activity coefficients, 2024. Accessed: March 21, 2025.

[51] Shun Myung Shin, Nak Hyoung Kim, Jeong Soo Sohn, Dong Hyo Yang, and Young Han Kim. Development of a metal recovery process from li-ion battery wastes. *Hydrometallurgy*, 79(3-4):172–181, 2005.

[52] Sibananda Sahu and Niharbala Devi. Two-step leaching of spent lithium-ion batteries and effective regeneration of critical metals and graphitic carbon employing hexuronic acid. *RSC advances*, 13(11):7193–7205, 2023.

[53] Abir Ghosh, Jamie M Foster, Gregory Offer, and Monica Marinescu. A shrinking-core model for the degradation of high-nickel cathodes (nmc811) in li-ion batteries: passivation layer growth and oxygen evolution. *Journal of The Electrochemical Society*, 168(2):020509, 2021.

[54] Shigeru Umino and John Newman. Temperature dependence of the diffusion coefficient of sulfuric acid in water. *Journal of the Electrochemical Society*, 144(4):1302, 1997.

[55] Lien-Chun Weng, Alexis T Bell, and Adam Z Weber. Modeling gas-diffusion electrodes for co 2 reduction. *Physical Chemistry Chemical Physics*, 20(25):16973–16984, 2018.

[56] Sigma-Aldrich. Hydrogen peroxide, 30% (w/w) in h2o, reagent grade, $\geq 99.0\%, 2024$.

A

Derivations for the shrinking core model

A.1. Concentration profile in the product layer

To describe the mass transfer of the liquid reactant diffusing through a small thin spherical shell inside the porous product layer, from r to r + Δr. With pseudo-steady-state conditions it is assumed that the amount of liquid reactant in this shell does not change over time. This means that the amount of liquid reactant diffusing into this shell, must be equal to the amount diffusing out. The mass balance over the spherical shell reads

$$(N_{\mathrm{LR}})_r - (N_{\mathrm{LR}})_{r+\Delta r} = 0 \tag{A.1}$$

The liquid reactant diffusing into the shell can be described by Fick's law Equation 1.23 multiplied by the cross-sectional area of the shell

$$\left(-\pi r^2 D_{\mathrm{e}} \frac{dC_{\mathrm{LR}}}{dr}\right)_r - \left(-\pi r^2 D_{\mathrm{e}} \frac{dC_{\mathrm{LR}}}{dr}\right)_{r+\Delta r} = 0 \tag{A.2}$$

Where D_{e} is the effective diffusivity. Dividing by πr^2 and taking the limit $\Delta r \to 0$ gives

$$\frac{d}{dr}\left(r^2 D_{\mathrm{e}} \frac{dC_{\mathrm{LR}}}{dr}\right) = 0 \tag{A.3}$$

Integrating twice gives the general solution for the concentration profile:

$$C_{\mathrm{LR}}(r) = -\frac{A}{r D_{\mathrm{e}}} + B \tag{A.4}$$

Applying the boundary conditions $C_{\mathrm{LR}}(r = r_{\mathrm{s}}) = C_{\mathrm{LRs}}$ and $C_{\mathrm{LR}}(r = r_{\mathrm{c}}) = C_{\mathrm{LRc}}$, the integrating constants A and B can be calculated:

$$A = \frac{(C_{\mathrm{LRs}} - C_{\mathrm{LRc}})D_{\mathrm{e}}}{\frac{1}{r_{\mathrm{c}}} - \frac{1}{r_s}}, \quad B = C_{\mathrm{LRc}} + \frac{(C_{\mathrm{LRs}} - C_{\mathrm{LRc}})D_{\mathrm{e}}}{r_{\mathrm{c}} D_{\mathrm{e}}(\frac{1}{r_{\mathrm{c}}} - \frac{1}{r_{\mathrm{s}}}} \tag{A.5}$$

Substituting A and B into the general equation gives:

$$C_{\mathrm{LR}}(r) = C_{\mathrm{LRc}} + (C_{\mathrm{LRs}} - C_{\mathrm{LRc}}) \left(\frac{1 - \frac{r_{\mathrm{c}}}{r}}{1 - \frac{r_{\mathrm{c}}}{r_{\mathrm{s}}}}\right) \tag{A.6}$$

This is the final expression for the concentration profile $C_{\mathrm{LR}}(r)$, which depicts how the concentration of the liquid reactant $C_{\mathrm{LR}}(r)$ varies radially within the porous product layer. Differentiating the concentration profile, evaluated at $r = r_{\mathrm{c}}$, gives the gradient at the reaction interface

$$\left(\frac{dC_{\mathrm{LR}}}{dr}\right)_{r=r_{\mathrm{c}}} = \frac{C_{\mathrm{LRs}} - C_{\mathrm{LRc}}}{r_{\mathrm{c}}\,(1 - r_{\mathrm{c}}/r_{\mathrm{s}})} \tag{A.7}$$

Substituting Equation A.7 into Equation 1.24 yields the diffusion rate at the core:

$$\frac{dN_{\mathrm{LR}}}{dt} = -4\pi r_{\mathrm{c}} D_{\mathrm{e}} \frac{C_{\mathrm{LRs}} - C_{\mathrm{LRc}}}{(1 - r_{\mathrm{c}}/r_{\mathrm{s}})} \tag{A.8}$$

Due to the pseudo steady-state assumption (mass transfer = diffusion = reaction), Equation 1.22 and Equation 1.27 are equal and result in:

$$C_{\mathrm{LRs}} = C_{\mathrm{LRb}} - \frac{r_{\mathrm{c}}^2}{r_{\mathrm{s}}^2} \frac{k}{k_{\mathrm{m}}} C_{\mathrm{LRc}}^n \tag{A.9}$$

Since Equation A.8 and Equation 1.27 are equal this results in:

$$C_{\mathrm{LRs}} = C_{\mathrm{LRc}} + \frac{k r_{\mathrm{c}} \left(1 - \frac{r_{\mathrm{c}}}{r_{\mathrm{s}}}\right) C_{\mathrm{LRc}}^n}{D_{\mathrm{e}}} \tag{A.10}$$

Equating the expressions for C_{LRs} found in Equation A.9 and Equation A.10 when $n = 1$ gives:

$$C_{\mathrm{LRc}} = \frac{C_{\mathrm{LRb}}}{1 + \left(\frac{r_{\mathrm{c}}}{r_{\mathrm{s}}}\right)^2 \left(\frac{k}{k_{\mathrm{m}}}\right) + \left(\frac{k r_{\mathrm{c}}}{D_{\mathrm{e}}}\right) \left(1 - \frac{r_{\mathrm{c}}}{r_{\mathrm{s}}}\right)} \tag{A.11}$$

Which gives an expression for the concentration of the LR at the unreacted core surface as a function of the concentration of the LR in the bulk

A.2. Time evolution of the shrinking core radius

Under the pseudo-steady-state assumption, the mass transfer rate, diffusion rate and reaction rate are equal. The overall LR rate consumption per solid particle, denoted by R_p in mol/s corresponds to the surface reaction rate (Equation 1.27) and is given by:

$$R_p = -\frac{dN_{\mathrm{LR}}}{dt} = 4\pi r_{\mathrm{c}}^2 k C_{\mathrm{LRc}}^n \tag{A.12}$$

The rate at which the solid reactant is consumed follows from the volume of the shrinking core, assuming a spherical volume the molar rate of consumption is given by:

$$\frac{dN_{\mathrm{SR}}}{dt} = \frac{\rho_{\mathrm{s}}}{M_{\mathrm{SR}}} \frac{d}{dt} \left(\frac{4}{3}\pi r_{\mathrm{c}}^3\right) = \frac{4\pi r_{\mathrm{c}}^2 \rho_{\mathrm{s}}}{M_{\mathrm{SR}}} \frac{dr_{\mathrm{c}}}{dt} \tag{A.13}$$

Where ρ_{s} is the density of the SR (kg/m^3) and M_{SR} is the molecular weight of the SR (kg/mol). From the general reaction in Equation 1.16, the reaction rates of the LR and SR are related as

$$\frac{dN_{\mathrm{LR}}}{dt} = \frac{1}{b} \frac{dN_{\mathrm{SR}}}{dt} = \frac{4\pi r_{\mathrm{c}}^2 \rho_{\mathrm{s}}}{b M_{\mathrm{SR}}} \left(\frac{dr_{\mathrm{c}}}{dt}\right) \tag{A.14}$$

In which b represents the stoichiometric coefficient. Equating Equation A.12 and Equation A.14 gives the rate of core shrinkage:

$$\frac{dr_{\mathrm{c}}}{dt} = -\frac{b M_{\mathrm{SR}} k}{\rho_{\mathrm{s}}} C_{\mathrm{LRc}}^n \tag{A.15}$$

To express this completely in terms of the bulk concentration, the expression for C_{LRc} derived in section A.1 is substituted, resulting in

$$\frac{dr_{\mathrm{c}}}{dt} = -\frac{b M_{\mathrm{SR}}}{\rho_{\mathrm{s}}} \frac{C_{\mathrm{LRb}}}{\frac{1}{k} + \left(\frac{r_{\mathrm{c}}}{r_{\mathrm{s}}}\right)^2 \left(\frac{1}{k_{\mathrm{m}}}\right) + \left(\frac{r_{\mathrm{c}}}{D_{\mathrm{e}}}\right) \left(1 - \frac{r_{\mathrm{c}}}{r_{\mathrm{s}}}\right)} \tag{A.16}$$

Which captures how the unreacted shrinking core radius evolves over time as a function of the bulk concentration, system's stoichiometry, reaction kinetics and transport limitations.

A.3. Coupling between bulk concentration and core radius

The evolution of the shrinking radius r_{c} depends on the concentration of the LR in the bulk (C_{LRb}). However, this concentration is not constant over time. As the reaction progresses, the LR is continuously consumed at the particle surface, causing C_{LRb} to decrease over time. This lowers the C_{LRc} and slows down the reaction rate. The core radius $r_{\mathrm{c}}(t)$ shrinks as the reaction progresses which leads to a lower reaction rate. As a result the concentration of the liquid reactant in the bulk and the shrinking radius are coupled to each other. $C_{\mathrm{LRb}}(t)$ influences $r_{\mathrm{c}}(t)$ via the reaction rate and $r_{\mathrm{c}}(t)$ influences $C_{\mathrm{LRb}}(t)$ via the shrinking surface area. The reaction rate per particle is defined as

$$R_{\mathrm{p}} = 4\pi r_{\mathrm{c}}^2 C_{\mathrm{LRc}} \tag{A.17}$$

To compute how C_{LRb} changes over time a mass balance is performed over the entire batch. The mole balance reads

$$R_p \cdot \rho_{\mathrm{SR}} + \frac{dC_{\mathrm{LRb}}}{dt} = 0 \tag{A.18}$$

This balance ensures that the total rate of LR is equal to the rate of concentration change in the bulk, and ρ_{SR} is the number of solid particles per unit volume of suspension and is calculated as follows:

$$\rho_{\mathrm{SR}} = \frac{C_{\mathrm{SR0}} M_{\mathrm{SR}}}{\rho_{\mathrm{s}} \cdot \frac{4}{3}\pi r_{\mathrm{s}}^3} \tag{A.19}$$

in which C_{SR0} is the initial molar concentration of the SR in the suspension (mol/l), M_{SR} is the molecular weight of the solid reaction (g/l) and $\rho_{\mathrm{s}} \cdot \frac{4}{3}\pi r_{\mathrm{s}}^3$ is the mass of a single particle of the solid reactant (g). Combining these expressions yields:

$$\frac{dC_{\mathrm{LRb}}}{dt} = -\frac{3M_{\mathrm{SR}}k}{\rho_{\mathrm{s}} r_{\mathrm{s}}} \left(\frac{r_{\mathrm{c}}}{r_{\mathrm{s}}}\right)^2 C_{\mathrm{SR0}} C_{\mathrm{LRc}}^n \tag{A.20}$$

This expression describes how the LR concentration decreases over time due to the unreacted shrinking cores.

A.4. Dimensionless concentration at the core surface

The expression for the LR concentration at the core, previously given in Equation 1.28, can be written in dimensionless form using:

$$C_{\mathrm{LRc}}^* = \frac{C_{\mathrm{LRc}}}{C_{\mathrm{LRb,0}}}, \quad C_{\mathrm{LRb}}^* = \frac{C_{\mathrm{LRb}}}{C_{\mathrm{LRb,0}}}, \quad r_{\mathrm{c}}^* = \frac{r_{\mathrm{c}}}{r_{\mathrm{s}}}, \quad \tau = \frac{D_{\mathrm{m}}\, t}{r_{\mathrm{s}}^2}, \tag{A.21}$$

$$\mathrm{Da} = \frac{k r_{\mathrm{s}} C_{\mathrm{LRb,0}}^{n-1}}{D_{\mathrm{m}}}, \quad \mathrm{Sh} = \frac{k_{\mathrm{m}} r_{\mathrm{s}}}{D_{\mathrm{m}}}, \quad \frac{\mathrm{Da}}{\mathrm{Sh}} = \frac{k C_{\mathrm{LRb,0}}^{n-1}}{k_{\mathrm{m}}} \tag{A.22}$$

For n=1, the dimensionless concentration at the core surfaces becomes:

$$C_{\mathrm{LRc}}^* \cdot C_{\mathrm{LRb,0}} = \frac{C_{\mathrm{LRb}}^* \cdot C_{\mathrm{LRb,0}}}{1 + (r_{\mathrm{c}}^*)^2 \left(\frac{\mathrm{Da}}{\mathrm{Sh}}\right) + \frac{\mathrm{Da}}{\epsilon^{3/2}} r_{\mathrm{c}}^* (1 - r_{\mathrm{c}}^*)} \tag{A.23}$$

$$C_{\mathrm{LRc}}^* = \frac{C_{\mathrm{LRb}}^*}{1 + (r_{\mathrm{c}}^*)^2 \left(\frac{\mathrm{Da}}{\mathrm{Sh}}\right) + \frac{\mathrm{Da}}{\epsilon^{3/2}} r_{\mathrm{c}}^* (1 - r_{\mathrm{c}}^*)} \tag{A.24}$$

A.5. Dimensionless evolution of core radius

The rate of the shrinking core is given by:

$$\frac{dr_{\mathrm{c}}}{dt} = -\frac{bM_{\mathrm{SR}}k}{\rho_{\mathrm{s}}} C_{\mathrm{LRc}}^n \tag{A.25}$$

and can be written in dimensionless form using:

$$\frac{dr_{\mathrm{c}}}{dt} = \frac{d\tau}{dt} \cdot \frac{dr_{\mathrm{c}}}{d\tau}, \quad \frac{d\tau}{dt} = \frac{D_{\mathrm{m}}}{r_{\mathrm{s}}^2}, \quad \frac{dr_{\mathrm{c}}}{d\tau} = r_{\mathrm{s}} \cdot \frac{dr_{\mathrm{c}}^*}{d\tau}, \quad k = \frac{D_{\mathrm{m}}\, \mathrm{Da}}{r_{\mathrm{s}} C_{\mathrm{LRb,0}}^{n-1}}$$

substituting these in yields

$$\frac{dr_{\mathrm{c}}^*}{d\tau} = -\frac{r_{\mathrm{s}}^2 b M_{\mathrm{SR}}}{\rho_{\mathrm{SR}} r_{\mathrm{s}} D_{\mathrm{m}}} k \left(C_{\mathrm{LRc}}\right)^n = -\frac{r_{\mathrm{s}}^2 b M_{\mathrm{SR}}}{\rho_{\mathrm{SR}} r_{\mathrm{s}} D_{\mathrm{m}}} \frac{D_{\mathrm{m}} \mathrm{Da}}{r_{\mathrm{s}} C_{\mathrm{LRb},0}^{n-1}} \left(C_{\mathrm{LRc}}\right)^n \tag{A.26}$$

Simplifying further gives

$$\frac{dr_{\mathrm{c}}^*}{d\tau} = -\frac{b M_{\mathrm{SR}} \mathrm{Da} C_{\mathrm{LRb},0}}{\rho_{\mathrm{SR}}} \left(\frac{C_{\mathrm{LRc}}}{C_{\mathrm{LRb},0}}\right)^n \tag{A.27}$$

Finally, expressing the result in its most compact form:

$$\frac{dr_{\mathrm{c}}^*}{d\tau} = -\frac{b M_{\mathrm{SR}} \mathrm{Da}\, C_{\mathrm{LRb},0}}{\rho_{\mathrm{SR}}} \left(C_{\mathrm{LRc}}^*\right)^n \tag{A.28}$$

This describes the dimensionless form of the shrinking radius as a function of time. Now Equation A.24 can be used for $n = 1$ to fill in the expression above:

$$\frac{dr_{\mathrm{c}}^*}{d\tau} = -\left(\frac{b M_{\mathrm{SR}} \mathrm{Da}\, C_{\mathrm{LRb},0}}{\rho_{\mathrm{SR}}}\right) \cdot \frac{C_{\mathrm{LRb}}^*}{1 + (r_{\mathrm{c}}^*)^2 \left(\frac{\mathrm{Da}}{\mathrm{Sh}}\right) + \left(\frac{\mathrm{Da}}{\epsilon^{3/2}}\right) r_{\mathrm{c}}^* (1 - r_{\mathrm{c}}^*)} \tag{A.29}$$

A.6. Dimensionless bulk concentration over time

The LR concentration of the bulk is described as:

$$\frac{dC_{\mathrm{LRb}}}{dt} = -\frac{3 M_{\mathrm{SR}} k r_{\mathrm{c}}^2 C_{\mathrm{SR0}} C_{\mathrm{LRc}}^n}{\rho_{\mathrm{s}} r_{\mathrm{s}}^3} \tag{A.30}$$

and be written in dimensionless form as follows:

$$\frac{D_{\mathrm{m}} C_{\mathrm{LRb},0}}{r_{\mathrm{s}}^2} \frac{dC_{\mathrm{LRb}}^*}{d\tau} = -\frac{3 M_{\mathrm{SR}} k (r_{\mathrm{c}}^* r_{\mathrm{s}})^2 C_{\mathrm{SR0}} (C_{\mathrm{LRc}}^* C_{\mathrm{LRb},0})^n}{\rho_{\mathrm{s}} r_{\mathrm{s}}^3} \tag{A.31}$$

$$\frac{dC_{\mathrm{LRb}}^*}{d\tau} = -\frac{3 M_{\mathrm{SR}} k r_{\mathrm{c}}^{*2} r_{\mathrm{s}} C_{\mathrm{SR0}} C_{\mathrm{LRc}}^{*n} C_{\mathrm{LRb},0}^n C_{\mathrm{LRb},0}^{-1}}{\rho_{\mathrm{s}} D_{\mathrm{m}}} \tag{A.32}$$

$$\frac{dC_{\mathrm{LRb}}^*}{d\tau} = -\frac{3 M_{\mathrm{SR}} k r_{\mathrm{s}} C_{\mathrm{LRb},0}^{n-1} C_{\mathrm{SR0}} r_{\mathrm{c}}^{*2} C_{\mathrm{LRc}}^{*n}}{\rho_{\mathrm{s}} D_{\mathrm{m}}} \tag{A.33}$$

Inserting the formula for the Da number gives:

$$\frac{dC_{\mathrm{LRb}}^*}{d\tau} = -\left(\frac{3 M_{\mathrm{SR}} C_{\mathrm{SR0}} \mathrm{Da}}{\rho_{\mathrm{s}}}\right) C_{\mathrm{LRc}}^{*n} r_{\mathrm{c}}^{*2} \tag{A.34}$$

Which is the dimensionless concentration in the bulk as a function of the dimensionless time

B

Magnetic separation simulation results

B.1. Levitation height calculation

This section presents the calculated levitation height of graphite particles in a paramagnetic $\mathrm{MnCl_2}$ solution. The results are based on the applied force balance, described in Equation 2.5, and show how the levitation height varies with different magnetic susceptibility values reported in the literature. The calculated levitation heights for the values provided by Miura, Egami, and Mirica are shown in Table B.1, Table B.2, and Table B.3, respectively.

Table B.1: Levitation calculation using magnetic susceptibility from Miura

Conc. [mol/L]	Density [g/cm^3]	χ^{V}	Levitation Height [mm]
0.7916	1.0781	8.919×10^{-5}	0.000
0.9739	1.0963	1.118×10^{-4}	0.000
1.1720	1.1159	1.364×10^{-4}	0.000
1.3867	1.1370	1.630×10^{-4}	0.000
1.6155	1.1594	1.914×10^{-4}	0.000
1.8607	1.1831	2.219×10^{-4}	0.000
2.1187	1.2080	2.539×10^{-4}	0.000
2.3900	1.2340	2.876×10^{-4}	0.000
2.6732	1.2610	3.227×10^{-4}	0.902
2.9939	1.2914	3.625×10^{-4}	1.864
3.2642	1.3169	3.960×10^{-4}	2.525
3.5186	1.3408	4.276×10^{-4}	3.006
3.9008	1.3763	4.750×10^{-4}	3.667
4.2459	1.4083	5.179×10^{-4}	4.208
4.6637	1.4466	5.697×10^{-4}	4.750
5.0929	1.4856	6.230×10^{-4}	5.291
5.7500	1.5444	7.045×10^{-4}	6.072

Table B.2: Levitation calculation using magnetic susceptibility from Egami

Conc. [mol/L]	Density [g/cm^3]	χ^{V}	Levitation Height [mm]
0.7916	1.0781	1.334×10^{-4}	0.000
0.9739	1.0963	1.663×10^{-4}	0.000
1.1720	1.1159	2.019×10^{-4}	0.000
1.3867	1.1370	2.406×10^{-4}	0.000
1.6155	1.1594	2.817×10^{-4}	0.000
1.8607	1.1831	3.259×10^{-4}	0.301
2.1187	1.2080	3.723×10^{-4}	1.503
2.3900	1.2340	4.212×10^{-4}	2.345
2.6732	1.2610	4.721×10^{-4}	3.066
2.9939	1.2914	5.299×10^{-4}	3.728
3.2642	1.3169	5.785×10^{-4}	4.208
3.5186	1.3408	6.243×10^{-4}	4.629
3.9008	1.3763	6.931×10^{-4}	5.170
4.2459	1.4083	7.552×10^{-4}	5.651
4.6637	1.4466	8.304×10^{-4}	6.192
5.0929	1.4856	9.077×10^{-4}	6.673
5.7500	1.5444	1.026×10^{-3}	7.395

Table B.3: Levitation calculation using magnetic susceptibility from Mirica

Conc. [mol/L]	Density [g/cm^3]	χ^{V}	Levitation Height [mm]
0.7916	1.0781	2.310×10^{-6}	0.000
0.9739	1.0963	4.925×10^{-6}	0.000
1.1720	1.1159	7.768×10^{-6}	0.000
1.3867	1.1370	1.085×10^{-5}	0.000
1.6155	1.1594	1.413×10^{-5}	0.000
1.8607	1.1831	1.765×10^{-5}	0.000
2.1187	1.2080	2.135×10^{-5}	0.000
2.3900	1.2340	2.525×10^{-5}	0.000
2.6732	1.2610	2.931×10^{-5}	0.000
2.9939	1.2914	3.391×10^{-5}	0.000
3.2642	1.3169	3.779×10^{-5}	0.000
3.5186	1.3408	4.144×10^{-5}	0.000
3.9008	1.3763	4.693×10^{-5}	0.000
4.2459	1.4083	5.188×10^{-5}	0.000
4.6637	1.4466	5.787×10^{-5}	0.000
5.0929	1.4856	6.403×10^{-5}	0.000
5.7500	1.5444	7.346×10^{-5}	0.000

B.2. Velocity-based stopping criterion

The velocity-based stopping criterion showed that settling time decreases with increasing particle size, following an approximate $1/\mathrm{d}^2$ scaling trend. Results for both thresholds $v_{\mathrm{pz}} \leq 10^{-7}$ m/s and $v_{\mathrm{pz}} \leq 10^{-8}$ m/s with $\Delta t =$1 s, are shown in Figure B.1 and Figure B.2.

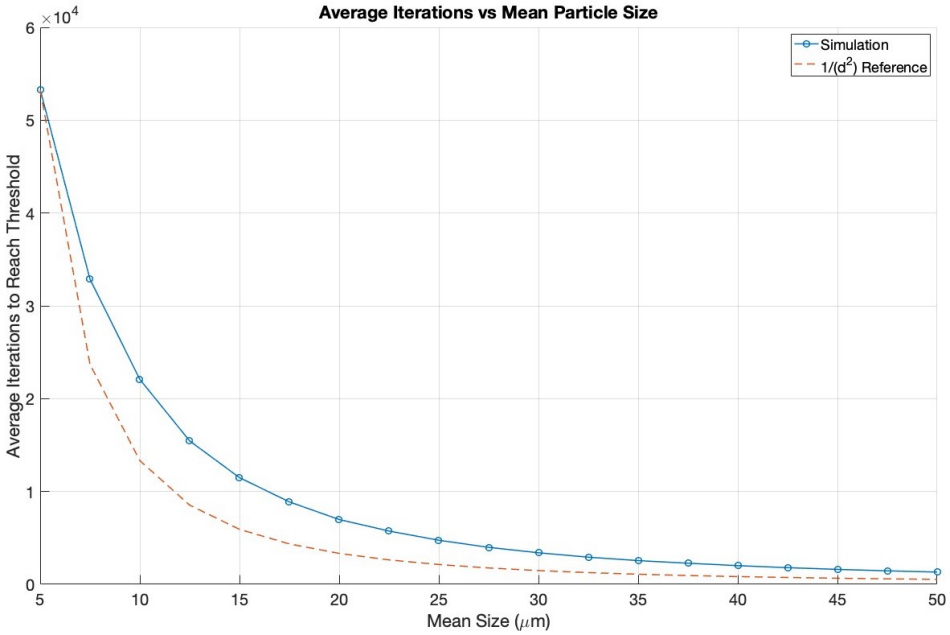

Figure B.1: Average number of iterations for 100 particles of mean size ranging from 5 to 50 μm before the threshold has been reached $\mathrm{v_{pz}} < 10^{-7}$ m/s

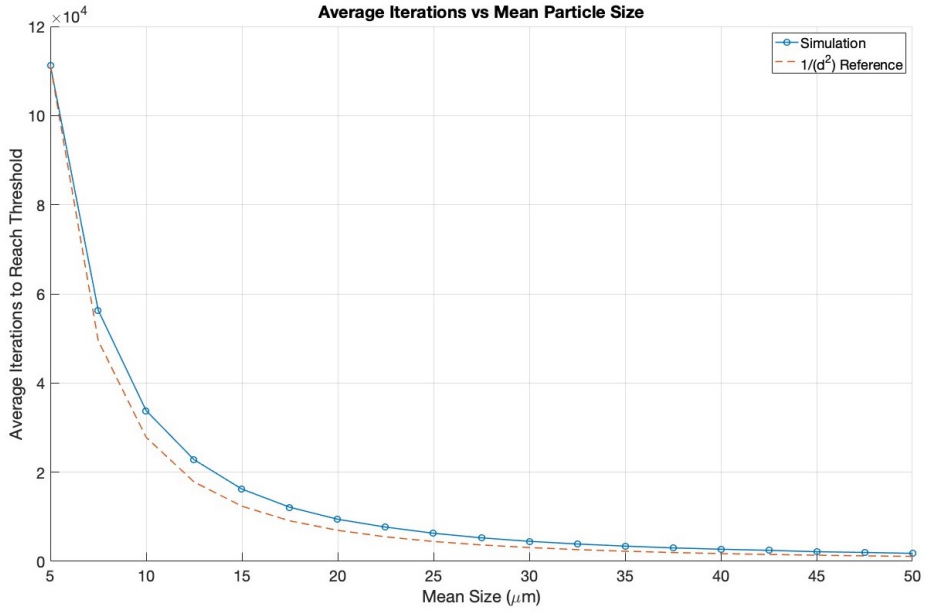

Figure B.2: Average number of iterations for 100 particles of mean size ranging from 5 to 50 μm before the threshold has been reached $\mathrm{v_pz} < 10^{-8}$ m/s

For a lower threshold (10^{-8} m/s), results align more closely with the reference curve and for higher velocity thresholds discrepancies between the simulations and the reference curve become more pronounced.

C

Temperature dependence of rate constant and diffusion coefficient

In the SCM, both the rate constant (k) and the diffusion coefficient (D_{m}) are temperature-dependent parameters which influence the leaching behaviour.

C.1. Rate constant

A baseline value for the rate constant $\mathrm{k}_0 = 2.17 \times 10^{-8}$ m/s at 25°C was adopted from a study which performed parametric fitting to align simulation results and experiments data for the leaching of $\mathrm{LiCoO_2}$ using hydrochloric acid (HCl) [6]. The temperature dependence of k follows an Arrhenius-type relation

$$k = \mathrm{k}_0 \cdot exp(\frac{E_a}{RT}) \tag{C.1}$$

In which R is the universal gas constant, T is the temperature (K) and E_a is the activation energy, which was reported as 32.4 kJ/mol for $\mathrm{LiCoO_2}$ dissolution [7]. The effect of the temperature on k across $T = 0 - 75$°C is shown in Figure C.1.

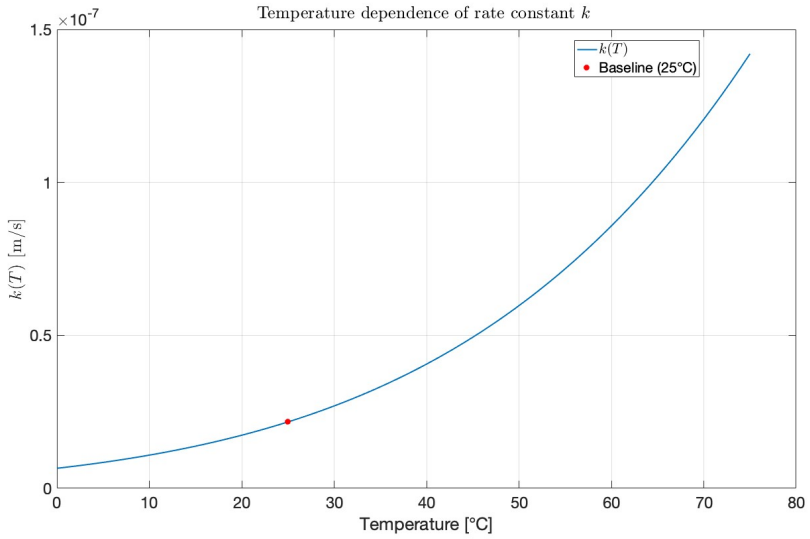

Figure C.1: Effect of temperature on the rate constant

C.2. Diffusion coefficient

The diffusion coefficient of sulfuric acid in water depends on both temperature and acid concentration. Umino et al. (1997) provide an empirical correlation for the diffusion coefficient of sulfuric acid valid for concentrations between 0.5-5.5 mol/L and temperatures between 0-35°C [54]. The diffusion coefficient is given by:

$$D_{\mathrm{m}} = \exp\left[-C_0\left(\frac{1}{T} - \frac{1}{298.15}\right)\right] \cdot C_1 \tag{C.2}$$

The coefficients C_0 and C_1 depend on the sulfuric acid concentration c (mol/L)and are given by:

- $C_0 = exp(7.699 + 0.2352[1 - exp(-12c^{1/2})] - 0.2977c + 0.04164c^{3/2} + 0.02023c^2)$
- $C_1 = exp(-10.56 - 0.3666[1 - exp(-12c^{1/2})] - 0.1107c + 0.2888c^{3/2} + 0.09151c^2)$

In Figure C.2 variation of the diffusion coefficient with temperature and concentration is shown.

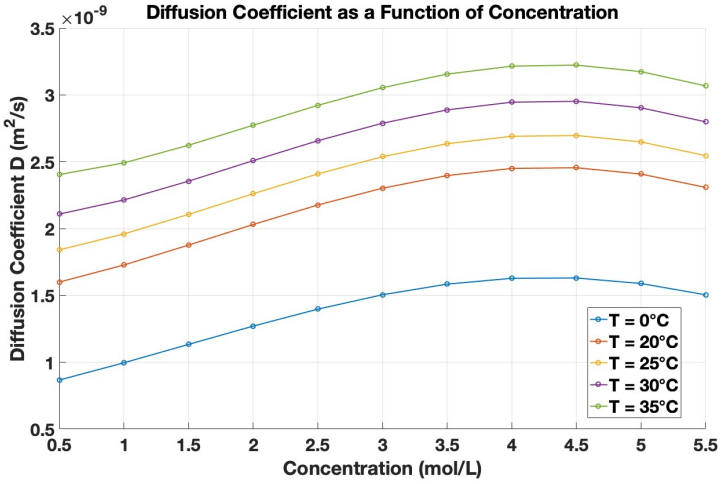

Figure C.2: Diffusion coefficient as a function of concentration for different temperatures

At a temperature of 35 °C and a sulfuric acid concentration of 2.5 mol/L, a reference value of $D_0 = 2.9221 \times 10^{-9}\ \mathrm{m^2/s}$ was found. For temperatures above 35 °C, values were extrapolated using an Arrhenius-type relation.

$$D_{\mathrm{m}} = D_0 \cdot \exp\left(-\frac{E_{\mathrm{A}}}{RT}\right) \tag{C.3}$$

Figure C.3 shows the diffusion coefficient over a temperature range of $T = 0 - 75$°C.

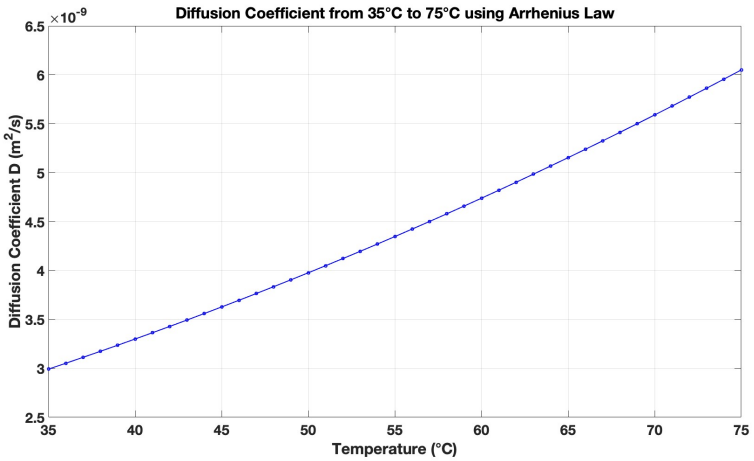

Figure C.3: Effect of the temperature on the diffusion coefficient $\mathrm{D_m}$

D

Model implementation

D.1. Results original model

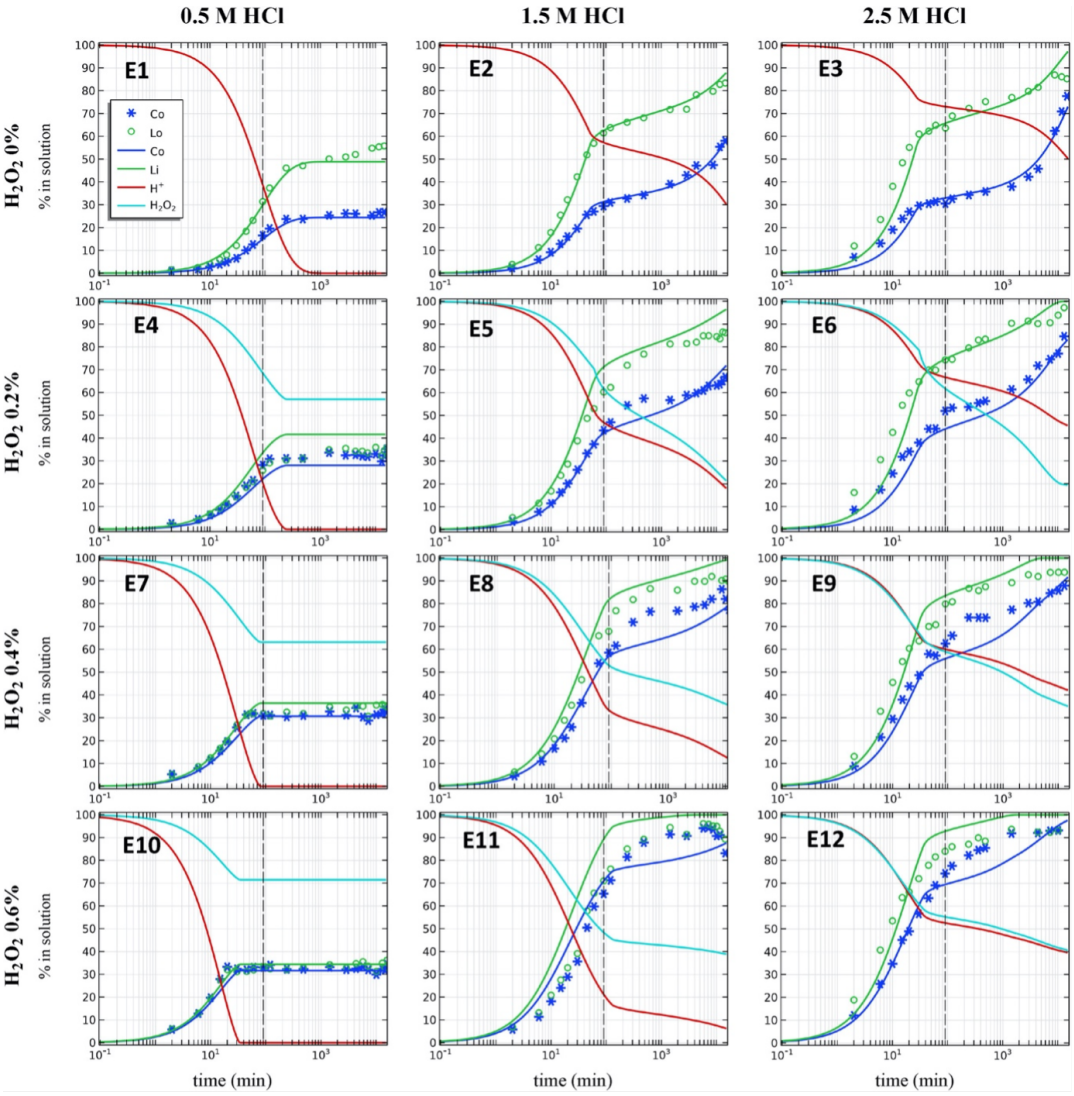

Figure D.1: Experimental (marks) and simulation (lines) results for Li and Co leaching under various H^+ and H_2O_2 conditions [6].

D.2. Concentration of $\mathrm{Co_3O_4}$ in reaction rate

In heterogeneous leaching reactions, the reaction rate is not only governed by the reaction rate constant but also by the available surface area at which the reaction occurs. This is reflected in the reaction rates r_1 and r_3 (for reaction 1 and 3), which are proportional to the surface area of the unreacted $\mathrm{LiCoO_2}$ core. For the rate expressions for reaction 2 and 4, which describe the dissolution of the $\mathrm{Co_3O_4}$ crust, the concentration of solid $\mathrm{Co_3O_4}$ is included in units of $\mathrm{mol/m^3}$. Typically, solid phases are not included in rate expressions as the activity of a pure solid is considered constant and does not influence the reaction rate. In this model, the use of $C_{\mathrm{Co_3O_4}}$ represents a different physical meaning and requires further justification. As the leaching reaction progresses, gradually a $\mathrm{Co_3O_4}$ crust is formed around the shrinking $\mathrm{LiCoO_2}$ core. This crust forms a physical diffusion barrier, limiting the transport of Li, Co and acid. A larger value for $C_{\mathrm{Co_3O_4}}$ represents a larger mass and therefore a greater resistance to further leaching. However, the presence of the $\mathrm{Co_3O_4}$ concentration in reaction rates $\mathrm{r_2}$ and $\mathrm{r_4}$ serves as an approximation for the available surface area. To explain this, consider the total surface area for the $\mathrm{Co_3O_4}$ crust. The total available surface area consists of both external and internal surfaces. The specific surface area of a porous solid is defined as [55]:

$$a_v = \frac{3(1-\varepsilon)}{r_{\mathrm{np}}} \tag{D.1}$$

in which r_{np} is the catalyst nanoparticle radius, and ε is the porosity of the crust. For a single solid particle, the total surface area per unit mass is given by:

$$\frac{\text{Total surface}}{m} = \frac{\text{Int. surface}}{m} + \frac{\text{Ext. surface}}{m} = \frac{4\pi r^2}{m} + \frac{a_v m}{\rho m} \tag{D.2}$$

which simplifies to:

$$\frac{\text{Total surface}}{m} = \frac{4\pi r^2}{m} + \frac{a_v}{\rho} \tag{D.3}$$

For porous materials, in general the internal surface area is much larger than the external surface area, such that $\frac{a_v}{\rho} \gg \frac{4\pi r^2}{m}$. Assuming the specific surface area does not alter significantly, the total surface area per unit mass is approximately constant. Therefore, the $C_{\mathrm{Co_3O_4}}$ can be effectively used as an approximation to capture the total surface area. The resistance the $\mathrm{Co_3O_4}$ concentration imposes to the diffusion of sulfuric acid, will be further discussed in section D.3.

D.3. Calculation of Porosity

The porosity ε is defined as the ratio of the void volume to the total volume of the shell:

$$\varepsilon = \frac{V_{\text{void}}}{V_{\text{shell}}} \tag{D.4}$$

Since the shell consists of both solid and void space, the void volume can be expressed as:

$$V_{\text{void}} = V_{\text{shell}} - V_{\text{solid}} \tag{D.5}$$

Substituting this into the porosity definition gives:

$$\varepsilon = 1 - \frac{V_{\text{solid}}}{V_{\text{shell}}} \tag{D.6}$$

in which V_{shell} is the total volume available for the crust and calculate as:

$$V_{\text{shell}} = \frac{4}{3}\pi\left(r_{\mathrm{s}}^3 - r_{\mathrm{c}}^3\right) \tag{D.7}$$

In which r_{s} is the initial particle radius (before shrinkage), and r_{c} is the current core radius. V_{solid} is the volume occupied by the accumulated solid material (i.e. $\mathrm{Co_3O_4}$. To calculate V_{solid}, the total mass of $\mathrm{Co_3O_4}$ in the system is first calculated as:

$$m_{\mathrm{Co_3O_4}} = C_{\mathrm{Co_3O_4}} M_{\mathrm{Co_3O_4}} V_{\mathrm{r}} \tag{D.8}$$

In which $C_{\mathrm{Co_3O_4}}$ is the total concentration of the accumulated $\mathrm{Co_3O_4}$ in the solution. Although this concentration is defined per unit solution volume according to Equation 3.25, the solid does not dissolve in the bulk but precipitates on the surface of the $\mathrm{LiCoO_2}$ particles, forming the crust. To calculate the mass of $\mathrm{Co_3O_4}$ formed per particle, the total mass is divided by the number of particles.

$$m_{\mathrm{Co_3O_4,particle}} = \frac{C_{\mathrm{Co_3O_4}} M_{\mathrm{Co_3O_4}} V_{\mathrm{r}}}{N_{\mathrm{p}}} \tag{D.9}$$

The volume occupied by the solid $\mathrm{Co_3O_4}$ for one $\mathrm{LiCoO_2}$ particle can be calculated as:

$$V_{\mathsf{solid}} = \frac{m_{\mathsf{Co_3O_4}}}{\rho_{\mathsf{Co_3O_4}}} \tag{D.10}$$

Substituting into the porosity equation gives:

$$\varepsilon = 1 - \frac{V_{\mathsf{solid}}}{V_{\mathsf{shell}}} = 1 - \frac{C_{\mathsf{Co_3O_4}} M_{\mathsf{Co_3O_4}} \cdot V_{\mathrm{r}}}{N_{\mathrm{p}} \cdot \rho_{\mathsf{Co_3O_4}} \cdot \frac{4}{3}\pi (r_{\mathrm{s}}^3 - r_{\mathrm{c}}^3)} \tag{D.11}$$

The equation for porosity takes into account the accumulation of $\mathrm{Co_3O_4}$ which affects the diffusion of acid through the crust as follows:

$$D_{\mathrm{H^+}}^{\mathsf{eff}} = D_{\mathrm{H^+}} \varepsilon exp(k_{\mathrm{D}}(r_{\mathrm{s}} - r_{\mathrm{c}})(1 - \varepsilon)) \tag{D.12}$$

In which the exponential term tries to model the tortuosity, as the crust gets thicker and denser, the resistance increases non-linearly. A higher $C_{\mathrm{Co_3O_4}}$ concentration will decrease the porosity and will lead to a lower effective diffusion coefficient. This is because there is less void space for $\mathrm{H^+}$ ions to diffuse through the denser $\mathrm{Co_3O_4}$ layer and will effectively increase the tortuosity of the path.

To determine the number of particles, first the total volume of $\mathrm{LiCoO_2}$ is calculated from its mass and density:

$$V_{\mathsf{total}} = \frac{\mathsf{mass}}{\rho} = \frac{2.5\ \mathsf{g}}{4.8\ \mathsf{g/cm^3}} = 5.208 \times 10^{-7}\ \mathsf{m^3} \tag{D.13}$$

The volume of a single $\mathrm{LiCoO_2}$ particle is:

$$V_{\mathsf{particle}} = \frac{4}{3}\pi \left(5 \times 10^{-6}\right)^3 = 5.2359 \times 10^{-16}\ \mathsf{m^3} \tag{D.14}$$

Thus, the total number of particles is estimated as

$$N_{\mathrm{p}} = \frac{5.208 \times 10^{-7}}{5.2359 \times 10^{-16}} = 0.9946 \times 10^9 \approx 10^9 \tag{D.15}$$

D.4. Model implementation into MATLAB

The leaching model, originally developed in COMSOL Multiphysics [6], has been rebuilt in MATLAB using an ODE solver. The model simulates the leaching process of $\mathrm{LiCoO_2}$ in HCl using $\mathrm{H_2O_2}$ as reducing agent. The ODE solver calculates:

1. The time-dependent concentrations of $\mathrm{Li^+}$, $\mathrm{Co^{2+}}$, $\mathrm{H^+}$, $\mathrm{H_2O_2}$.
2. The formation and dissolution of $\mathrm{Co_3O_4}$.
3. The shrinking $\mathrm{LiCoO_2}$ radius.

The ODE is solved iteratively and updates each time step the state vector containing: $\mathrm{r_c}$, $C_{\mathrm{H_2O_2}}$, $\mathrm{C_{Co_3O_4}}$, $C_{\mathrm{LiCoO_2}}$, $C_{\mathrm{Li^+}}$, $C_{\mathrm{Co^{2+}}}$ and $C_{\mathrm{H^+,bulk}}$. In the following steps the working principle of the model is explained.

Step 1: Initial values

All initial values for particle properties, species concentrations and other parameters are given in Table 3.3. At the beginning, $C_{\mathrm{H^+,core}} = C_{\mathrm{H^+,bulk}}$ since no $\mathrm{Co_3O_4}$ crust has formed yet.

Step 2a: no Crust-Formation
In this case no crust has formed yet as $\mathrm{C_{Co_3O_4}} = 0$. The diffusion of $\mathrm{H^+}$ is not hindered and $C_{\mathrm{H^+,core}} = C_{\mathrm{H^+,bulk}}$. Continue to step 3.

Step 2b: Crust-Formation
As the reaction proceeds, $\mathrm{Co_3O_4}$ accumulates and forms a solid crust around the shrinking $\mathrm{LiCoO_2}$ core. The diffusion of $\mathrm{H^+}$ is hindered which leads to a decrease in $C_{\mathrm{H^+,core}}$. A gradual change of $C_{\mathrm{H^+,core}}$ is assumed rather than an abrupt change as described in the original model. As the $\mathrm{Co_3O_4}$ accumulates the porosity decreases and this leads to a lower diffusion coefficient D_{eff}. The porosity was calculated as follows.

$$\varepsilon = 1 - \frac{C_{\mathrm{Co_3O_4}} \cdot M_{\mathrm{Co_3O_4}} \cdot V_{\mathrm{r}}}{N_{\mathrm{p}} \cdot \rho_{\mathrm{Co_3O_4}} \cdot \frac{4}{3}\pi(r_{\mathrm{s}}^3 - r_{\mathrm{c}}^3)} \tag{D.16}$$

For a steady-state system, it is assumed that the diffusion rate of $\mathrm{H^+}$ through the $\mathrm{Co_3O_4}$ crust is equal to the consumption rate of $\mathrm{H^+}$. This balance can be expressed as:

$$V_{\mathrm{r}} \cdot (-2r_1 - 3r_3) = -D_{\mathrm{eff}} \cdot \frac{C_{\mathrm{H^+}}^{\mathrm{bulk}} - C_{\mathrm{H^+}}^{\mathrm{core}}}{(r_{\mathrm{s}} - r_{\mathrm{c}})} N_{\mathrm{p}}(4\pi r_{\mathrm{s}} r_{\mathrm{c}}) \tag{D.17}$$

The expressions for the reaction rates r_1 and r_3 are substituted into the expression and yield:

$$V_{\mathrm{r}} \cdot \left(2k_1 \frac{N_{\mathrm{p}} 4\pi r_{\mathrm{c}}^2}{V_{\mathrm{r}}} C_{\mathrm{H^+}}^{\mathrm{core}} + 3k_3 \frac{N_{\mathrm{p}} 4\pi r_{\mathrm{c}}^2}{V_{\mathrm{r}}} \left(C_{\mathrm{H^+}}^{\mathrm{core}}\right)^{\frac{1}{3}} \left(C_{\mathrm{H_2O_2}}\right)^2\right) = D_{\mathrm{eff}} \cdot \frac{C_{\mathrm{H^+}}^{\mathrm{bulk}} - C_{\mathrm{H^+}}^{\mathrm{core}}}{(r_{\mathrm{s}} - r_{\mathrm{c}})} N_{\mathrm{p}}(4\pi r_{\mathrm{s}} r_{\mathrm{c}}) \tag{D.18}$$

Now rearranging the equation gives:

$$C_{\mathrm{H^+}}^{\mathrm{core}} = C_{\mathrm{H^+}}^{\mathrm{bulk}} - \frac{(r_{\mathrm{s}} - r_{\mathrm{c}})}{(r_{\mathrm{s}} r_{\mathrm{c}}) D_{\mathrm{eff}}} \cdot \left(2k_1 r_{\mathrm{c}}^2 C_{\mathrm{H^+}}^{\mathrm{core}} + 3k_3 r_{\mathrm{c}}^2 \left(C_{\mathrm{H^+}}^{\mathrm{core}}\right)^{\frac{1}{3}} \left(C_{\mathrm{H_2O_2}}\right)^2\right) \tag{D.19}$$

This equation is numerically solved in MATLAB, using a solver function at each time step to update $C_{\mathrm{H^+}}^{\mathrm{core}}$. Once this value is obtained, the new production rates are calculated and also the shrinking radius of $\mathrm{LiCoO_2}$ is updated.

Step 3: Compute reaction rates
The model considers four main reactions and the reaction rates describe how quickly the reactions occur. The newly determined $C_{\mathrm{H^+}}^{\mathrm{core}}$ can be used to recalculate the four reaction rates below.

- $\mathrm{LiCoO_2}$ **dissolution** (acidic dissolution in the presence of $\mathrm{H_2O_2}$):

$$r_1 = \left(\frac{k_1 N_{\mathrm{p}} 4\pi r_{\mathrm{c}}^2}{V_{\mathrm{r}}}\right) C_{\mathrm{H^+}}^{\mathrm{core,eff}} \tag{D.20}$$

$$r_3 = \left(\frac{k_3 N_{\mathrm{p}} 4\pi r_{\mathrm{c}}^2}{V_{\mathrm{r}}}\right) \left(C_{\mathrm{H^+}}^{\mathrm{core,eff}}\right)^{\frac{1}{3}} \left(C_{\mathrm{H_2O_2}}\right)^2 \tag{D.21}$$

- $\mathrm{Co_3O_4}$ **dissolution** (acidic dissolution in the presence of $\mathrm{H_2O_2}$):

$$r_2 = k_2 \left(C_{\mathrm{Co_3O_4}}\right) \max\left(C_{\mathrm{H^+}}^{\mathrm{core,eff}}, C_{\mathrm{H^+}}^{\mathrm{bulk}}\right)^{2/3} \tag{D.22}$$

$$r_4 = k_4 \left(C_{\mathrm{Co_3O_4}}\right) \max\left(C_{\mathrm{H^+}}^{\mathrm{core,eff}}, C_{\mathrm{H^+}}^{\mathrm{bulk}}\right)^{2/3} C_{\mathrm{H_2O_2}} \tag{D.23}$$

The reaction rates r_1 and r_3 are modified from the original model, because Equation 3.18 and Equation 3.20 assumed that all $\mathrm{Co_3O_4}$ dissolution occurs only at the core surface. However, once the $\mathrm{Co_3O_4}$ crust forms, the proton concentration at the core $C_{\mathrm{H^+}}^{\mathrm{core,eff}}$ may become zero, which will lead to r_2 and r_4 also being zero. However, in reality $\mathrm{Co_3O_4}$ will form around the shrinking $\mathrm{LiCoO_2}$ core and the outer surface will still be exposed to the bulk concentration ($C_{\mathrm{H^+,bulk}}$). To take this into account, the reaction rates r_2 and r_4 for the dissolution of $\mathrm{Co_3O_4}$ are modified to include both $C_{\mathrm{H^+}}^{\mathrm{core,eff}}$ and $C_{\mathrm{H^+}}^{\mathrm{bulk}}$. This ensures that when $C_{\mathrm{H^+}}^{\mathrm{core,eff}}$ is small due to diffusion limitations, dissolution can still occur due to $C_{\mathrm{H^+}}^{\mathrm{bulk}}$.

Step 4: Compute Species concentrations
With the (updated) reaction rates, the concentrations of the other species are updated according to:

$$\frac{dC_{\mathrm{Li^+}}}{dt} = r_{\mathrm{Li^+}} = r_1 + r_3 \tag{D.24}$$

$$\frac{dC_{\mathrm{Co^{2+}}}}{dt} = r_{\mathrm{Co^{2+}}} = \frac{1}{2}r_1 + 3r_2 + r_3 + 3r_4 \tag{D.25}$$

$$\frac{dC_{\mathrm{H^+,bulk}}}{dt} = r_{\mathrm{H^+}} = -2r_1 - 6r_2 - 3r_3 - 6r_4 \tag{D.26}$$

$$\frac{dC_{\mathrm{H_2O_2}}}{dt} = r_{\mathrm{H_2O_2}} = -\frac{1}{2}r_3 - r_4 \tag{D.27}$$

$$\frac{dC_{\mathrm{Co_3O_4}}}{dt} = r_{\mathrm{Co_3O_4}} = \frac{1}{6}r_1 - r_2 - r_4 \tag{D.28}$$

$$\frac{dC_{\mathrm{LiCoO_2}}}{dt} = -r_1 - r_3 \tag{D.29}$$

Step 5: Calculate and update the shrinking core radius
The rate of dissolution of $\mathrm{LiCoO_2}$ is a good indicator for the shrinking core radius. The rate of $\mathrm{LiCoO_2}$ dissolution can be expressed as:

$$r_{\mathrm{LiCoO_2}} = -r_1 - r_3 \tag{D.30}$$

which is equal to:

$$\frac{1}{V_\mathrm{r}}\frac{dN_{\mathrm{LiCoO_2}}}{dt} = -r_1 - r_3 \tag{D.31}$$

For a single particle, the number of moles of $\mathrm{LiCoO_2}$ is:

$$N_{\mathrm{LiCoO_2}} = \frac{m_{\mathrm{LiCoO_2}}}{M_{\mathrm{LiCoO_2}}} \tag{D.32}$$

Taking the time derivative gives:

$$\frac{dN_{\mathrm{LiCoO_2}}}{dt} = \frac{1}{M_{\mathrm{LiCoO_2}}}\frac{dm_{\mathrm{LiCoO_2}}}{dt} = \frac{1}{M_{\mathrm{LiCoO_2}}}\frac{d\left(\frac{4}{3}\pi r_\mathrm{c}^3\rho_{\mathrm{LiCoO_2}}\right)}{dt} = \frac{4\pi r_\mathrm{c}^2\rho_{\mathrm{LiCoO_2}}}{M_{\mathrm{LiCoO_2}}}\frac{dr_\mathrm{c}}{dt} \tag{D.33}$$

For all particles, the total number of moles over time is:

$$\frac{dN_{\mathrm{LiCoO_2}}}{dt} = \frac{4\pi r_\mathrm{c}^2 N_\mathrm{p}\rho_{\mathrm{LiCoO_2}}}{M_{\mathrm{LiCoO_2}}}\frac{dr_\mathrm{c}}{dt} \tag{D.34}$$

Substituting this value into the kinetics equations gives:

$$\frac{4\pi r_\mathrm{c}^2 N_\mathrm{p}\rho_{\mathrm{LiCoO_2}}}{V_\mathrm{r}M_{\mathrm{LiCoO_2}}}\frac{dr_\mathrm{c}}{dt} = \left[\left(\frac{k_1 N_\mathrm{p} 4\pi r_\mathrm{c}^2}{V_\mathrm{r}}\right)C_{\mathrm{H^+}}^{\mathrm{core}} + \left(\frac{k_3 N_\mathrm{p} 4\pi r_\mathrm{c}^2}{V_\mathrm{r}}\right)\left(C_{\mathrm{H^+}}^{\mathrm{core}}\right)^{\frac{1}{3}}\left(C_{\mathrm{H_2O_2}}\right)^2\right] \tag{D.35}$$

Solving for $\frac{dr_\mathrm{c}}{dt}$ yields:

$$\frac{dr_\mathrm{c}}{dt} = -\frac{M_{\mathrm{LiCoO_2}}}{\rho_{\mathrm{LiCoO_2}}}\frac{V_\mathrm{r}}{4\pi r_\mathrm{c}^2 N_\mathrm{p}}\left[k_1 C_{\mathrm{H^+}}^{\mathrm{core}} + k_3\left(C_{\mathrm{H^+}}^{\mathrm{core}}\right)^{\frac{1}{3}}\left(C_{\mathrm{H_2O_2}}\right)^2\right] \tag{D.36}$$

which can be simplified to:

$$\frac{dr_\mathrm{c}}{dt} = -\frac{M_{\mathrm{LiCoO_2}}}{\rho_{\mathrm{LiCoO_2}}}\left[k_1 C_{\mathrm{H^+}}^{\mathrm{core}} + k_3\left(C_{\mathrm{H^+}}^{\mathrm{core}}\right)^{\frac{1}{3}}\left(C_{\mathrm{H_2O_2}}\right)^2\right] \tag{D.37}$$

This equation describes how the core radius shrinks over time, based on the proton concentration at the core and the hydrogen peroxide concentration.

Step 6: Calculation of the Damköhler number

To evaluate the transition between a reaction-controlled regime and a diffusion-controlled regime, the $\mathrm{Da}_1(\mathrm{II})$ and $\mathrm{Da}_3(\mathrm{II})$ were calculated during each time step. When $\mathrm{Da} < 1$ the reaction is kinetically controlled and when $\mathrm{Da} > 1$ the reaction is controlled by diffusion. To compute the Damköhler number the two extreme boundary conditions as described in the original model were assumed.

- $C_{\mathrm{H^+,core}} = C_{\mathrm{H^+,bulk}}$ for the kinetic rate
- $C_{\mathrm{H^+,core}} = 0$ for the diffusion rate

which gives the following formulas for the Damköhler numbers.

$$\mathrm{Da}_1(\mathrm{II}) = \frac{r_{1,\mathrm{kinetic}}}{r_{1,\mathrm{diffusion}}} = \frac{k_1 \left(\frac{N_\mathrm{p} 4\pi r_\mathrm{c}^2}{V_\mathrm{r}}\right) C_{\mathrm{H^+,bulk}}}{D_\mathrm{eff} \frac{C_{\mathrm{H^+,bulk}} - \mathbf{0}}{(r_\mathrm{s} - r_\mathrm{c})} \frac{N_\mathrm{p}(4\pi r_\mathrm{s} r_\mathrm{c})}{V_\mathrm{r}}} \tag{D.38}$$

$$\mathrm{Da}_3(\mathrm{II}) = \frac{r_{3,\mathrm{kinetic}}}{r_{3,\mathrm{diffusion}}} = \frac{k_3 \left(\frac{N_\mathrm{p} 4\pi r_\mathrm{c}^2}{V_\mathrm{r}}\right) C_{\mathrm{H^+,core}}^{1/3} C_{\mathrm{H_2O_2}}^2}{D_\mathrm{eff} \frac{C_{\mathrm{H^+,bulk}} - \mathbf{0}}{(r_\mathrm{s} - r_\mathrm{c})} \frac{N_\mathrm{p}(4\pi r_\mathrm{s} r_\mathrm{c})}{V_\mathrm{r}}} \tag{D.39}$$

However, unlike the model, the reaction rates are not adapted when $\mathrm{Da} < 1$ becomes $\mathrm{Da} > 1$ as is described in Step 8 of the model. The $\mathrm{Da}_1(\mathrm{II})$ and $\mathrm{Da}_3(\mathrm{II})$ numbers are calculated over time to evaluate when the system shifts from a kinetically controlled regime to a diffusion controlled regime. Once all variables have been updated, the simulation returns to step 1. This iterative method is repeated over time.

D.5. Conversion of volume percentage concentration to molar concentration

To convert a $\mathrm{H_2O_2}$ concentration in volume percentage (vol %) to molar concentration ($\mathrm{mol/m^3}$), a commercial $\mathrm{H_2O_2}$ concentration is assumed. This solution contains 30 g of $\mathrm{H_2O_2}$ per 100 g of solution (30% w/w), with a density of 1.11 g/cm^3 and a molar mass of H_2O_2 = 34.0147 g/mol [56]. For example, converting a 5 vol % $\mathrm{H_2O_2}$: The volume of $\mathrm{H_2O_2}$ in 1 L of solution is:

$$V_{\mathrm{H_2O_2,sol}} = \frac{5}{100} \times 1000\,\mathrm{mL} = 50\,\mathrm{mL} \tag{D.40}$$

The total mass of this 50 mL of solution is:

$$m_\mathrm{sol} = 50\,\mathrm{mL} \times 1.11\,\mathrm{g/cm^3} = 55.5\,\mathrm{g} \tag{D.41}$$

Assuming a 30% w/w concentration, the mass of pure $\mathrm{H_2O_2}$ is:

$$m_{\mathrm{H_2O_2,pure}} = 0.30 \times 55.5\,\mathrm{g} = 16.65\,\mathrm{g} \tag{D.42}$$

The number of moles $n_{\mathrm{H_2O_2}}$ becomes:

$$n_{\mathrm{H_2O_2}} = \frac{16.65\,\mathrm{g}}{34.0147\,\mathrm{g/mol}} \approx 0.49\,\mathrm{mol} \tag{D.43}$$

Which gives a molar concentration of:

$$C_{\mathrm{H_2O_2}} = 0.49\,\mathrm{mol/L} = 490\,\mathrm{mol/m^3} \tag{D.44}$$

Table D.1 shows various mass and molar concentrations of $\mathrm{H_2O_2}$ for different volume percentages.

Table D.1: Mass (g) and concentration ($\mathrm{mol/m^3}$) for different vol% of $\mathrm{H_2O_2}$

Vol% H_2O_2	Mass of H_2O_2 (g)	Concentration (mol/m^3)
0	0.0	0
5	16.65	490
10	33.30	980
15	49.95	1470
20	66.60	1960
25	83.25	2450

D.6. Results modified model using sulfuric acid

Figure D.2a-c and Figure D.3a-c show the time evolution of the Da number, Co and Li extraction percentages, Co_3O_4 accumulation and the core radius for $LiCoO_2$ leaching in sulfuric acid at $C_{H_2SO_4} = 2000$ mol/m^3 for two hydrogen peroxide concentrations: $C_{H_2O_2} = 0 \text{mol/m}^3$ and $C_{H_2O_2} = 500 \text{mol/m}^3$ for the first 120 minutes.

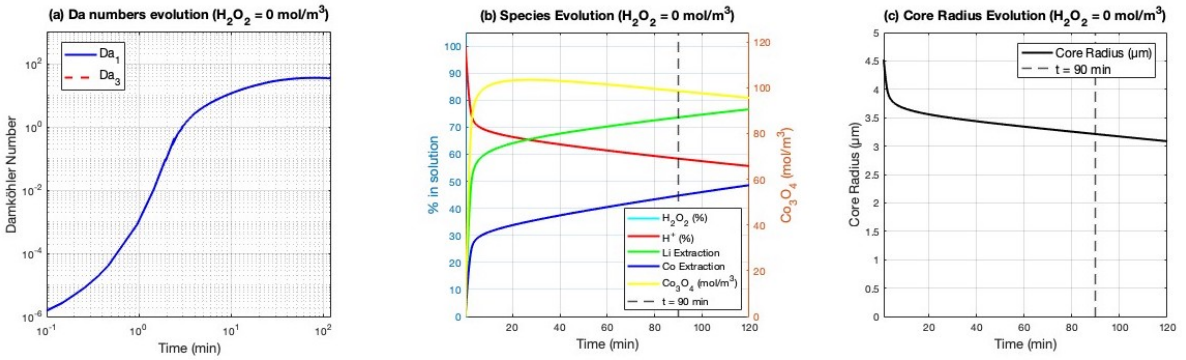

Figure D.2: Evolution of the Da numbers, species concentrations and core radius for $H_2O_2 = 0 \text{ mol/m}^3$

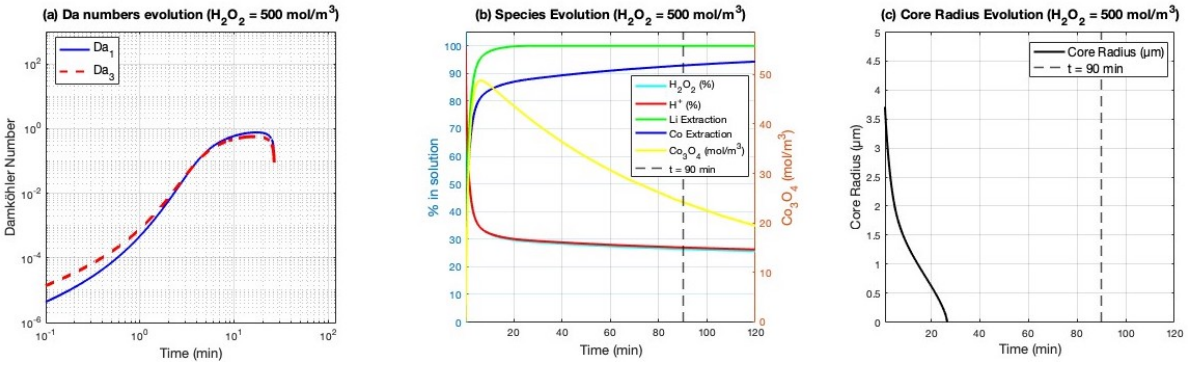

Figure D.3: Evolution of the Da numbers, species concentrations and core radius for $H_2O_2 = 500 \text{ mol/m}^3$

In the absence of H_2O_2, Li and Co extraction reach values of 70% and 35% respectively within 10 minutes. Co_3O_4 accumulation peaks at 120 mol/m^3 and the core radius shrinks to about 2.75 μm. After this point, leaching of both Li and Co slows down and diffusion becomes rate-limiting, as indicated by $Da_1 > 1$ after 3 minutes. For a concentration of $C_{H_2O_2} = 500$ $[mol/m^3]$ leaching rates increase significantly. Li and Co extraction reaches 100% and 85%, respectively within the first 10 minutes and no transition to a diffusion-controlled regime is observed, as Da_1 and Da_3 numbers remain below 1. This significant improvement in leaching efficiency can be attributed to the presence of H_2O_2, enhancing cobalt leaching by reducing Co^{3+} to Co^{2+}. Complete core shrinkage occurs after 15 minutes, coinciding with complete Li extraction. Co extraction continues as the formed Co_3O_4 gradually dissolves and eventually reaches a value of 94%. Even in the presence of H_2O_2 some Co_3O_4 is formed, however the peak concentration is much lower, only 50 mol/m^3. This indicates that the adddition of H_2O_2 also significantly reduces the accumulation of Co_3O_4 in the system, which was also seen when HCl was used.